Thermal Re-Radiation Modelling for the Precise Prediction and Determination of Spacecraft Orbits

Sima Adhya

Thesis submitted for the degree of Doctor of Philosophy of the University of London

2005

Department of Geomatic Engineering

University College London

ProQuest LLC
789 East Eisenhower Parkway
P.O. Box 1346
Ann Arbor, MI 48106-1346

Abstract

Thermal re-radiation (TRR) affects spacecraft orbits when a net recoil force results from the uneven emission of radiation from the spacecraft surface; these forces can perturb spacecraft trajectories by several metres over a few hours. The mis-modelling of TRR limits the accuracy with which some spacecraft orbits can be computed, and in turn limits capabilities of applications where satellite positioning is key. These range from real-time navigation to geodetic measurements using low earth orbiting spacecraft.

Approaches for the precise analytical modelling of TRR forces are presented. These include methods for the treatment of spacecraft multilayer insulation (MLI), solar panels and other spacecraft components. Techniques for determining eclipse boundary crossing times for an oblate earth and modelling penumbral fluxes are also described. These affect both the thermal force and the considerably larger solar radiation pressure (SRP) force. These methods are implemented for the Global Positioning System (GPS) Block IIR spacecraft and the altimetry satellite Jason-1.

For GPS Block IIR, model accuracy is assessed by orbit prediction through numerical integration of the spacecraft force model. Orbits were predicted over 12 hours and compared to precise orbits before and after thermal and eclipse-related models were included. When the solar panel model was included, mean orbit prediction errors dropped from 3.3m to 3.0m over one orbit; inclusion of the MLI model reduced errors further to 0.6m. For eclipsing satellites, the penumbral flux model reduced errors from 0.7 m to 0.56m.

The Jason-1 models were tested by incorporation into GIPSY-OASIS II, the Jet Propulsion Laboratory's (JPL) orbit determination software. A combined SRP and TRR model yielded significant improvements in orbit determination over all other existing models and is now used routinely by JPL in the operational orbit determination of Jason-1.

Acknowledgements

I am indebted to my supervisors Professor Paul Cross and Dr Marek Ziebart for providing constant supervision and support throughout all stages of the project and giving me the opportunity to work in such a fantastic subject area. I am particularly grateful to Marek for his contagious enthusiasm and ever-optimistic outlook regarding all our research.

I am grateful to many people from the UK and international community who have shown an interest and offered helpful advice and data. I would specifically like to thank Yoaz Bar-Sever from JPL and Henry Fliegel from the Aerospace Corporation for spacecraft data and ongoing assistance, Graham Appleby from the SLR facility at Herstmonceux for photometry data and Nick Cavan and Brian Shaunessy at the Rutherford Appleton Laboratory for thermal property data and technical advice. I acknowledge the National Space Science Data Center at the World Data Center for Satellite Information. I gratefully acknowledge EPSRC for the funding which enabled me to carry out this work.

Most of the results in this thesis could not have been achieved without the help of my colleagues in the department. Special thanks to Ant Sibthorpe, for collaboration, debates, white board drawings, programming advice, proof reading and all round helpfulness. Thanks also to Peter Arrowsmith and Simon Edwards for technical assistance and support. I am grateful to all three for many discussions (varied in nature) and for providing a stimulating and productive environment.

I am enormously grateful to Robert for his love, laughter, support and unwavering patience. I thank my brother Shaumik and friends Alison and Marc, who have listened patiently over the last three years through all the highs and lows.

I dedicate this thesis to my Mum and Dad, who have constantly inspired and motivated me. Their love gives me the strength to face challenges, and the freedom to make mistakes.

Table of Contents

List of Figures

List of Tables

Part I

Chapter 1 Introduction

Space based systems have wide ranging applications; these include navigation systems such as the Global Positioning System (GPS) and geodetic missions such as satellite altimetry, gravity field recovery and synthetic aperture radar. These missions fundamentally rely upon knowledge of the position of the spacecraft; hence the capabilities of these applications are limited by how accurately the spacecraft orbits can be computed. Orbit accuracy can be improved by correctly accounting for all forces which act on a spacecraft. The gravitational components of the force field, such as those due to the Earth, Sun and Moon are now well understood, but the non-gravitational forces are more problematic to characterise. The work presented here focuses on the non-gravitational non-conservative force due to thermal re-radiation from a spacecraft surface.

Thermal re-radiation perturbs spacecraft orbits when a net recoil force results from the uneven emission of radiation from the spacecraft surface. Though this force has a relatively small magnitude (~100 million times smaller than Earth's gravity), it can cause metre level perturbations to the trajectory of a spacecraft after only a few hours. The analytical modelling of this force and its effect on orbit computations are the focus of this study.

1.1 Goals of study

The aims of this study are to:

- develop methods for modelling the forces that result from spacecraft surface thermal re-radiation (TRR), based on a purely physical analysis of the problem
- apply these models to real spacecraft
- assess the strength of these methods based on their ability to improve the accuracy with which their orbits can be predicted and determined

This study is pertinent in the areas of satellite geodesy and astrodynamics. These fields are discussed in Section 1.2.

1.2 Satellite geodesy and astrodynamics

The word Geodesy literally means dividing the earth (Bomford, G., 1971), but has come to describe the science concerned with the measurement and mapping of points on the Earth's surface. Geodesy encompasses a set of techniques which, once developed, can be applied to other areas of science or engineering in order to meet the following objectives:

1. Determination of precise, global and regional coordinate reference frames
2. Precise determination of the earth's gravity field and temporal variations
3. The measurement and modelling of geodynamical phenomena (eg, crustal deformation, glacial rebound and global ocean circulation)

Satellite geodesy makes use of artificial satellites as high orbiting reference points which are visible over large areas. Compared with classical land based surveying techniques, the main advantages of using satellites are that they are able to bridge large distances, and thus establish geodetic ties between continents and islands. The issue of data gaps is less problematic, since satellites can provide data with global coverage.

Astrodynamics encompasses the study of the motion of both natural and artificial objects in space, though it is principally concerned with spacecraft trajectories, from launch to re-entry. Within astrodynamics, understanding of the motion of spacecraft and determination of orbits is effectively the end of the analytical process. Within satellite geodesy, the precisely determined orbit of a spacecraft provides a data set upon which further analyses are based. Whilst the models produced in this thesis have direct relevance in astrodynamics, their applications lie within the scope of satellite geodesy.

1.3 A brief history of satellite orbit determination

Many ancient civilisations including the Chinese, Indians and Greeks made astronomical and planetary observations from which they developed primitive understandings of the motion of celestial bodies. The first laws of planetary motion

were proposed by Kepler at the start of the seventeenth century, who determined them empirically based on observation data. These laws were formalised by Newton in his theory of gravity in 1666 and provided the first fundamental understanding of the physics of orbit dynamics. During the next three centuries, the field matured. Detailed refinements of satellite orbit models came about during the Cold War, when the race to develop intercontinental ballistic missiles and to land a man on the moon required the accomplishment of sophisticated mission objectives with elaborate constraints. This gave rise to immense efforts to improve knowledge in this field. Important benefits that flowed from this competition included space-based communication, navigation and surveillance systems.

The first object whose orbit was determined by the analysis of an emitted signal was Sputnik. Launched by the Soviet Union in October 1957, Sputnik was the first artificial satellite to orbit the Earth. Researchers at the Johns Hopkins Applied Physics Laboratory (APL) in Baltimore calculated that they could determine Sputnik's orbit simply by measuring the Doppler-induced changes in the frequency of the simple radio signal that it transmitted. Several years later, another APL scientist was seeking a system that would allow Polaris nuclear submarines to precisely track their positions. He realised that this could be achieved by inverting the approach used by the scientists working on Sputnik: by measuring a radio signal from a satellite whose position is known, a submarine could determine its own position (Tikhonravov, M., 1994).

The next few decades saw the emergence of many more sophisticated technologies, including microelectronics, radar and digital computers. These, combined with detailed theoretical and empirical models of Earth's gravity, the atmosphere, and planetary ephemerides enabled the development of systems which could be used to accurately determine the position of satellites.

The level of accuracy required in the knowledge of a satellite's orbit depends on the particular goals of a space project. In accord with these requirements, a variety of tracking systems are employed in present space projects. These include satellite laser ranging, Doppler Orbitography and Radiopositioning Integrated by Satellite (DORIS), the US Global Positioning System (GPS), and the recently commissioned European Galileo, due to be operational in 2008. Existing systems can currently provide spatial

information on the surface of the earth with precisions at the sub centimetre level. These systems can also be used to determine positions of low earth orbiting satellites.

1.4 The computation of precise orbits

To predict the trajectory of a spacecraft, its position and velocity must be correctly specified at one instant, and all forces which influence its motion must be known. The forces that drive the shape of a satellite trajectory include the Earth's gravity field, third body gravitational forces due to the Sun, Moon and planets, tidal Earth gravity field effects, and relativistic force effects. These forces are now well understood and highly accurate models for them are available, particularly when using data from the current Gravity Recovery and Climate Experiment (GRACE) mission, which has contributed significant improvements to the knowledge of the Earth's gravity field (Heugentobler, U. & Beutler, G., 2003). There is another set of forces which act on a spacecraft known as non-conservative forces (NCFs), so called because they result in an energy change to the spacecraft. Among the largest NCF is solar radiation pressure (SRP), caused by the impact of solar photons on the satellite surface. In the last decade, SRP has received some attention and now high precision analytical techniques exist to model this force (Ziebart, 2004a). Less progress has been made on the other NCF forces which are one to two orders of magnitude smaller than SRP. These include the force due to radiation reflected and emitted by the Earth, and of course TRR. Depending on altitude, a satellite may also be subject to considerable atmospheric drag effects, which for low earth orbiters (LEOs) constitute a force comparable with SRP. These forces are described in detail in Chapter 2.

NCFs are problematic to characterize analytically as they depend on the satellite's instantaneous attitude, surface geometry, optical and material properties, as well as the incident radiation flux and particulate environment. The structural and material property data is often hard to acquire. This is partly because spacecraft data are not generally released into the public domain. Additionally some of the data required are difficult to quantify accurately. Examples of the latter include surface material properties, since the nature and rate of material degradation in space is not well known, and spacecraft attitudes which may be subject to unpredictable variations.

In practice, neither the state of the spacecraft nor the forces can ever be defined completely accurately; any attempt to predict a trajectory will result in some divergence from the true position of the spacecraft over time.

However, if the distance of the spacecraft from a well-determined position on the surface of the Earth is known, again as a function of time, this information could be incorporated in the computation to correct the integrated trajectory and produce a better orbit. In principle, if many accurate range observations were available from reference stations with known co-ordinates, the orbit computation could be reduced to a series of spatial resections. In practice, none of these ranges or station co-ordinates are known exactly either; they too can only be estimated. The most accurate orbit solution is obtained when both force models and tracking data are combined, weighted by their respective accuracies. The detailed exploration of the physical model allows a better evaluation of the accuracies of the force models. Accurate range data is sometimes only available after the orbit has occurred, when data from ground tracking stations has been processed and made available, hence it is not useful for real time applications.

The level of sophistication of the orbit computation is dictated by the desired accuracy in the final solution; this depends on the requirements of the application. Two types of precise orbit computation are relevant in this thesis: orbit prediction and orbit determination.

- Orbit prediction

Predicted orbits refer to those that have been propagated from an initial position and velocity using a set of models describing the forces acting on the spacecraft. No tracking data during the period of prediction is used[1]. These techniques are described in more detail in Chapter 5. Predicted orbits play an important role in a variety of processes. These include real time GPS navigation, spacecraft design and operation and the efficiency with which satellites can be tracked by systems such as SLR.

[1] In GNSS applications tracking data collected at *previous* epochs is used to constrain future positions

- Orbit Determination

Orbit determination is a complex process which combines observations made by tracking stations with spacecraft force models of varying degrees of sophistication. Extra parameters may be computed or scale factors applied to certain force model parameters to enable the estimated trajectory to better fit the observations. There are three main types of orbits produced by this method: dynamic, reduced dynamic and kinematic. They differ in the balance chosen between force models and tracking data used, and are described in greater detail in Chapter 7. They are particularly suitable when position data is required hours or several days after the event when large amounts of range data from ground stations to satellites can be made available. There are many analysis centres worldwide which independently carry out this type of orbit processing for GPS spacecraft. These include:

- Centre for Orbit Determination in Europe (CODE), Switzerland
- Natural Resources Canada (EMR), Canada
- European Space Agency (ESA), Germany
- GeoForschungs Zentrum Institute (GFZ), Germany
- Jet Propulsion Laboratory (JPL), USA
- National Geodetic Survey (NGS), USA
- Scripps Institution of Oceanography (SIO), USA

These centres are members of the International GPS Service (IGS), which combines data from all these centres to provide an official GPS orbit, along with other high-quality GPS data and data products. The fact that so many agencies dedicate time to the production of high precisions orbits is an indication of their importance and of their non-trivial nature.

Both orbit prediction and determination techniques require an a priori dynamic model of the spacecraft. The closer the dynamic models are to the true forces, the closer the computed trajectory will be to the actual orbit. The more accurate the dynamic model, the better the final computed orbit. Section 1.5 outlines a few areas where precise orbits are essential to the successful mission performance.

1.5 The applications of precise orbits

Precise orbits play a key role in a number of areas, including Global Navigation Satellite Systems (GNSS), satellite altimetry, satellite gravity recovery and synthetic aperture radar (SAR) missions.

Real-time GPS applications such as navigation fundamentally rely upon the prediction of spacecraft positions. In the GPS process, although observation data from tracking stations are continually incorporated to update predictions, it is the force models which play the main role in determining the predicted trajectory of the spacecraft.

Aside from navigation, GPS systems can be used in real-time and in near real-time to monitor displacements of engineering structures such as bridges and dams that may occur due to small ground deformations caused by high loading or seismic activity (Behr, J. et al., 1998). Generally short baseline differencing techniques (using multiple receivers) have been used for these measurements; in these cases orbit errors are less important. However there is a current trend towards using single receiver precise point positioning techniques (Heroux, P. et al., 2004), whereby satellite orbit errors have a higher impact on the results. The real-time monitoring of deformations in large engineering structures such as oil rigs, where double differencing is not possible also depends on the quality of satellite orbits. Other developing technologies using GPS include real-time weather forecasting, by estimating the amount of water vapour in the atmosphere by the delay in the GPS signal (Reigber, C. et al., 2002). These applications are currently limited by the accuracy of predicted orbits, and improving the orbits would directly benefit these applications.

GNSS spacecraft orbits are used as references from which the position and velocity of points on the surface of the Earth can be calculated. The study of tectonic activity is one area where high precision positioning is key. Continuous networks of GPS receivers can provide measurements that help to model the deformation of the Earth's crust over time, and over areas ranging from tens to thousands of square kilometres (Liu, M. et al., 2000). Models are used to study the earthquake cycle, the effect of faulting and uplift on the Earth's surface, and the physics of continental deformation. These studies play an important role when quantifying seismic hazard and interpreting how past environments

control the distribution of natural resources. GPS networks are also used to monitor the thickness of ice sheets and the rate of glacial rebound. Biases in orbits would alias into GPS receiver positions and affect the accuracy of the target geophysical parameters.

Low Earth orbiting satellites (LEOs) are now one of the primary platforms (along with other aerial observations) used to make large-scale measurements of environmental phenomena, and the accuracy with which their trajectories can be determined is a factor which can limit what they can achieve. LEO satellite orbits often rely on GPS positioning for the calculation of their orbits. Errors in GPS orbits will therefore also lead to errors in the LEO orbits. These applications have stimulated advances in precise orbit determination. Satellite altimetry uses the measured travel time of a radar pulse to and from the sea surface to determine the distance of the sea surface from the spacecraft. For the translation of this measurement into a sea surface height, the satellite's absolute position must be determined with high precision in a suitable reference frame. Inaccuracies in the orbit are particularly problematic in that they tend to be expressed systematically over many thousands of kilometres and alias into the determination of large sea surface topography and ocean currents. Topex/Posiedon, a French American altimetry satellite mission measures ocean surface topography to within an accuracy of 4.2cm and enabled scientists to forecast the 1997-98 El Niño effect (Haines, B. et al., 2002). The follow-on mission Jason-1 aims to monitor global ocean circulation, study interactions of the oceans and atmosphere, improve climate predictions and observe events such as El Niño. Jason-1's overarching mission goal is to measure sea-surface heights to an accuracy of 1cm and (with the inclusion of the work in this thesis along with other studies) has recently been achieved. A new goal of 5mm has now been set (Bertiger, W., 2004).

The new millennium has heralded an era of missions aimed at producing a highly precise Earth gravity field. These include: CHAMP (Challenging Mini-satellite Payload), launched 15th July 2000; GRACE, launched 17th March 2002 and the soon-to-be-launched GOCE (Gravity Field and Steady-State Ocean Circulation Explorer). These missions use three axes accelerometers, which measure the combined accelerations caused by surface forces (as opposed to forces which act directly on the centre of mass of the spacecraft). A high precision orbit is required and the surface force effects (deduced from measurements made by the accelerometers) are removed from

this; further orbit perturbations are assumed to be due to the gravity field, and third body effects. Though non-conservative forces are measured, models are still required for calibration of the accelerometers, and for the deduction of specific non-conservative forces such as atmospheric drag.

1.6 Motivation

The applications described in Section 1.5 would benefit in terms of the accuracy of the data they produce from improved models of the non-conservative forces acting on the spacecrafts. To summarise, the main reasons for conducting this research are to:

- improve our understanding of the factors which influence the motion of a spacecraft
- improve the ability with which spacecraft orbits can be predicted and determined
- reduce the aliasing of orbit errors into geophysical parameters by constraining the errors in the mathematical model of the orbit.

1.7 Research methodology

In order to calculate the force due to thermal re-radiation, it is necessary to:

- characterise the radiation flux in the spacecraft vicinity
- model the interaction of this flux with the spacecraft surface
- determine spacecraft surface temperatures
- develop algorithms to calculate the surface thermal forces as a function of space and time
- obtain real spacecraft data for chosen test satellites

Two distinct regimes are considered for the spacecraft: the steady state regime where the spacecraft is in full sunlight and temperatures are assumed to change very slowly, and the transient regime that occurs during eclipses, when surface temperatures fall rapidly.

For accurate modelling of forces that depend on incident solar flux, it is necessary to know precisely when the spacecraft crosses shadow boundaries, so that the incident solar flux can be reduced accordingly. The shadow regions consist of the penumbra and umbra: the penumbra is the region where sunlight is partially occluded by the Earth and

the umbra is the region that is totally devoid of solar radiation. A method is developed to calculate crossing times into and out of shadow regions, and to estimate the reduction in flux in the penumbral regions. These methods should improve all forces that depend upon solar radiation flux.

Two test cases are chosen to which the models are applied; these are the GPS Block IIR spacecraft (in medium earth orbit (MEO)) and Jason-1 (in LEO). The test cases require different testing methods due to their different orbit environments. GPS Block IIR models are evaluated by analysing improvements to orbit prediction models whereas Jason-1 models are tested by their effect on orbit determination capabilities.

1.8 Thesis outline

The overall layout of the project is separated into Parts I-IV. The following chart is intended to clarify the thinking behind the overall approach and to outline what each part of the thesis tackles.

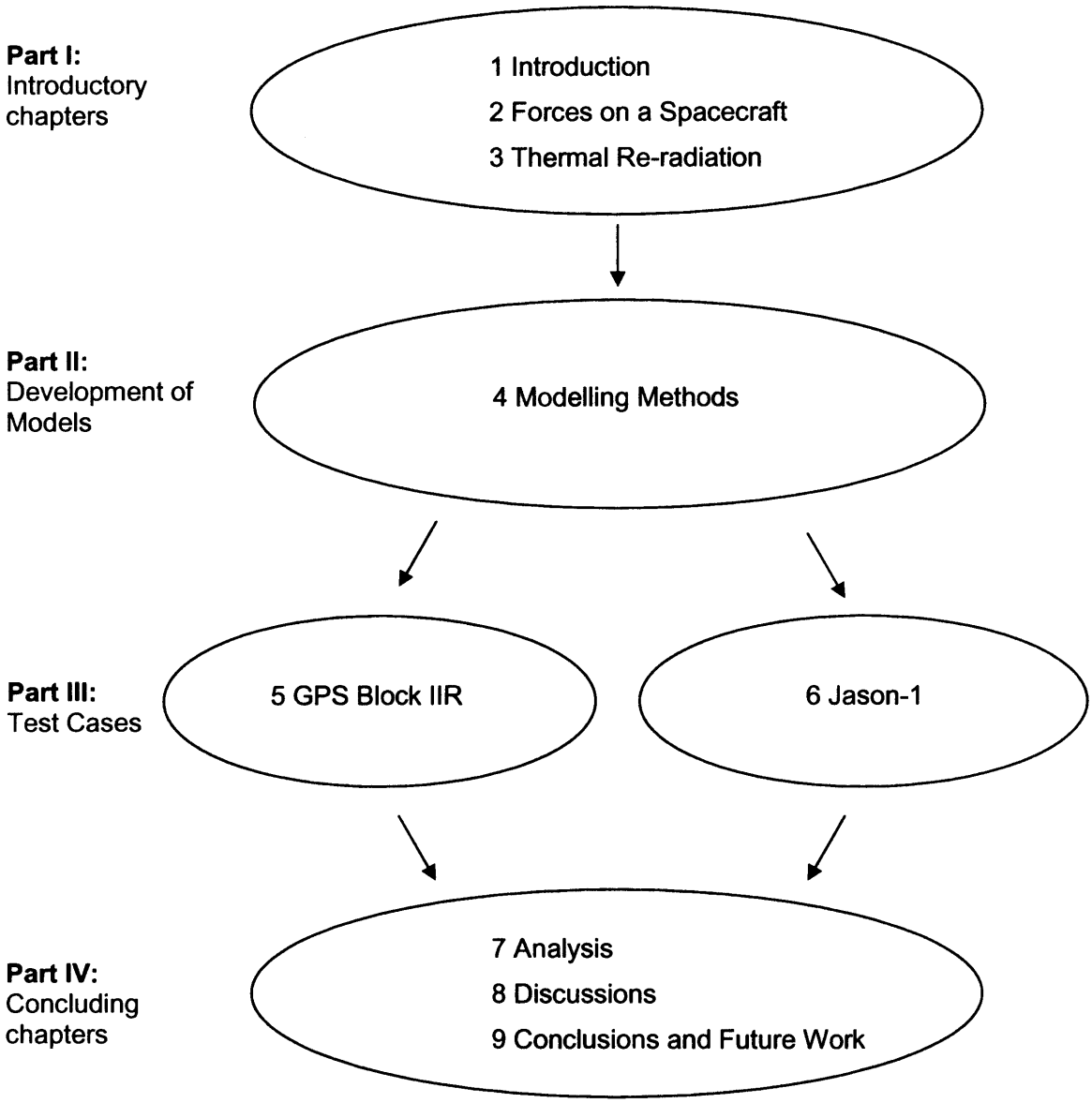

Figure 1.1: Thesis structure

1.8.1 Chapter outline

Chapter 1 introduces the problem of thermal re-radiation in orbit determination and prediction and defines the goals of the study. The importance of precise orbit computation is established and the areas to which this work bears relevance are highlighted. The layout of the thesis is given and the contents of each chapter are briefly summarised.

Chapter 2 gives a description of all the significant forces acting on a spacecraft in Earth orbit. Where possible, the method for their treatment in orbit computation is given, and the magnitude of spacecraft accelerations due to these forces is demonstrated for a low

earth orbiter (Jason-1) and medium earth orbiter (GPS Block IIR). This chapter includes a section on coordinate systems which will be useful for expressing different effects throughout this thesis.

Chapter 3 provides a more detailed explanation of the basis of the force due to thermal re-radiation and how it is characterised. Analytical and empirical methods for treatment of this force are described and with these in mind, the motivation for producing good a priori models is re-established. The published literature relevant to this work is reviewed.

In Chapter 4 the models developed in this thesis are derived. These consist of thermal force models for solar panels and surfaces covered in multilayer insulation in the steady state and transient regimes. The treatment of other surfaces, such as antennas is considered. Models for better determining the flux during eclipse regions are also described, including a method for determining boundary crossing times for an oblate earth and the reduction of flux in the penumbral regions.

Chapters 5 and 6 are concerned with the application of the modelling methods to the GPS Block IIR and Jason-1 spacecraft respectively. Each chapter reviews the spacecraft system, the data used in the modelling process and describes how the methods have been adapted specifically for each spacecraft. Orbit prediction (for GPS Block IIR) and orbit determination (for Jason-1) methods used for model testing are described. Each chapter concludes with the results of these tests and a brief analysis of the results.

Chapter 7 analyses in more detail the models, testing methods and results. Uncertainties in the parameter set and their effect on the modelled orbits are scrutinised. The thermal force is analysed in different reference frames. Remaining sources of error are identified and explored.

Chapter 8 includes a discussion of the strengths and deficiencies in each part of the model, and the general applicability of the methods produced in the thesis. Specific applications of this work are described, and an evaluation is made of the extent to which the goals set in this thesis have been achieved.

Chapter 9 summarises the work carried out in this thesis and states the main conclusions that can be made from this study. It also contains suggestions for future work in this problem domain.

Summary

In this chapter, the goals of this project have been defined and reasons for carrying out the work in this thesis are established. The accuracy of computed orbits is limited in part by the lack of detailed models of spacecraft surface thermal re-radiation forces. Greater orbit accuracies will improve the capabilities of applications which rely upon them. Modelling the motion of a spacecraft relies on knowledge of all significant forces acting on it. These forces are discussed in the next chapter.

Chapter 2 Forces acting on a spacecraft

Chapter outline

To dynamically model the orbit of a spacecraft, it is necessary to consider all forces which have significant effects on its trajectory. This section describes those forces and outlines the approaches to their modelling in orbit computations. Examples of their effects are given for two spacecraft, GPS Block IIR, which orbits at an altitude of ~20200km, and Jason-1 which orbits at an altitude of ~1340km. For most force effects, graphs of acceleration over one orbit on 2nd March 2004 are given for each spacecraft. Finally this chapter gives a description of the main coordinate systems used in the context of spacecraft orbits.

2.1 Orbital motion

From Newton's law of gravitation, the force F on mass m orbiting about a spherically symmetrical body of mass M at distance r from the centre of mass, where G is the Gravitational constant is defined as:

$$F = -\frac{GMm}{r^2} \tag{2.1}$$

The corresponding vector acceleration $\ddot{\underline{r}}$ is given by:

$$\ddot{\underline{r}} = -\frac{GM}{r^3}\underline{r} \tag{2.2}$$

Given an initial position and velocity, this second order differential equation (Equation 2.2) can be solved analytically to yield the position and velocity of mass m at future epochs. This $1/r^2$ force field provides a basic model from which we can derive a reasonable first approximation to the motion of a satellite around Earth.

In reality, the Earth is not a uniformly dense sphere; this factor along with other effects causes perturbations to this idealised orbit, and more refined models for these forces are required for the development of the actual equations of motion. The addition of the perturbing accelerations a_p gives:

$$\ddot{\boldsymbol{r}} = -\frac{GM\boldsymbol{r}}{\boldsymbol{r}^3} + \sum \boldsymbol{a}_p \tag{2.3}$$

Once these perturbations are added, it is extremely difficult to calculate a closed form analytical solution for Equation 2.3 and instead numerical procedures must be invoked. In numerical integration techniques, all modelled forces acting at a particular satellite position are explicitly calculated, and they are used as starting conditions for the next integration step.

Under the action of conservative forces, which are primarily gravitational, the mechanical energy of the system (that is, the sum of its kinetic and potential energies) is conserved. Technically, the system here refers to all the objects considered in the problem; the spacecraft, the Sun, Moon and the planets. If the energy state of the spacecraft is known at some epoch, then its energy state at any later epoch can be predicted as a function of position alone, that is, the energy state is independent of the path taken. The motion of satellite can never be completely described by a consideration of a purely conservative force field, but is useful nevertheless in the estimation of trajectories. In a non-conservative force field the spacecraft energy state is path-dependent, and any attempt to predict the future energy state has to model all the significant non-conservative forces as a function of space and time. The principal non-conservative forces acting on spacecraft are due to solar radiation pressure, thermal re-radiation, atmospheric drag and albedo effects. An additional force which falls in this category is thrust caused by signal emission from any antenna aboard the satellite.

In this chapter, the following perturbing forces are considered:

- Non-spherical earth gravity terms
- Third body effects (Sun, Moon, Planets)
- Solid Earth, ocean and pole tides
- Relativistic effects

- Solar radiation pressure
- Earth Radiation pressure
- Thermal re-radiation
- Atmospheric drag
- Force resulting from signals transmitted by satellite (antenna thrust)

These forces and their magnitudes are discussed in Section 2.2.

2.2 Perturbing forces

2.2.1 Conservative forces

2.2.1.1 Earth's gravitational field

As predicted by Newton, the Earth's rotation about its polar axis causes its shape to deviate from a perfect sphere (Montenbruck, O. & Gill, E., 2000). The earth is more accurately described by an oblate spheroid with an equatorial diameter that exceeds the polar diameter by about 20km. For any satellite with a non-zero inclination, the equatorial bulge exerts a force on the satellite such that it results in a secular drift of the right ascension of the ascending node (the point where the satellite crosses the equator from the Southern hemisphere to the Northern hemisphere). This perturbation is three orders of magnitude smaller than the central gravitational attraction and is commonly referred to as J2. The asphericity and inhomogeneous mass distribution of the earth cause a variety of further gravitational perturbations that affect the trajectory of a satellite.

The gravitational field of the Earth as a whole can be represented in terms of a potential field which satisfies Laplace's equation at all external points (Bomford, G., 1971). Laplace's equation is a partial second order differential equation and in cartesian coordinates is given by:

$$\left(\frac{\partial^2}{\partial x^2}+\frac{\partial^2}{\partial y^2}+\frac{\partial^2}{\partial z^2}\right)V=0 \tag{2.4}$$

where V is the gravitational potential field of the earth. Any function which satisfies it is called a harmonic. Laplace's equation for the potential in spherical polar co-ordinates is:

$$\frac{1}{r^2}\frac{\partial}{\partial r}\left(r^2\frac{\partial V}{\partial r}\right)+\frac{1}{r^2\sin\theta}\frac{\partial}{\partial\theta}\left(\sin\theta\frac{\partial V}{\partial\theta}\right)+\frac{1}{r^2\sin^2\theta}\frac{\partial^2 V}{\partial\theta^2}=0 \qquad (2.5)$$

The solutions to Equation 2.5 are spherical harmonics which have the form:

$$V_p=\frac{GM}{r}\left(\frac{a_e}{r}\right)^n P_{n,m}(sin\varphi)(C_{nm}cos(m\lambda)+S_{nm}sin(m\lambda)) \qquad (2.6)$$

where:

V_p = The gravitational potential at point p (ϕ,λ,r)

a_e = mean equatorial radius of the earth

n = degree of gravity field expansion

m = order of gravity field expansion

$P_{n,m}$ (sinϕ) = associated Legendre polynomial

λ= geocentric longitude of p

ϕ = geocentric latitude of p

C_{nm}, S_{nm} = spherical harmonic coefficients

The superposition of spherical harmonics can be used to represent physical phenomena distributed over the surface of a sphere in the same way that a Fourier series represents a one dimensional function with a combination of periodic functions. Some examples of spherical harmonic functions are shown pictorially in Figure 2.1 (the name of the type of harmonic is given in brackets). When m=0, the geopotential surface is divided into latitudinal bands and *zonal* harmonics result (the geopotential is independent of longitude); when m=n and the surface is divided into longitudinal sectors and are known as *sectoral* harmonics. For m <n and m ≠0, the surface is divided into rectangular domains and are known as *tesseral* harmonics.

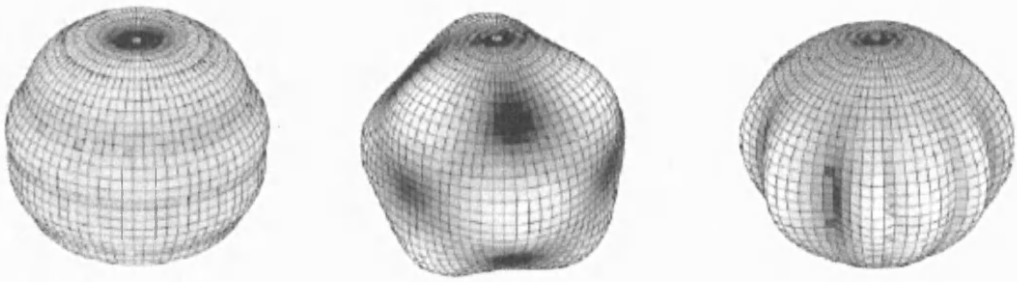

a) n=5, m=0 (zonal) b) n=5, m=3 (tesseral) c) n=5, m=5 (sectoral)

Figure 2.1: Examples of spherical harmonics of degree n and order m (Laxon, S., 2003)

The gravitational potential *Vp* at all points above the surface of the earth can be expressed as a summation of spherical harmonics as in Equation 2.7.

$$V_p = \frac{GM}{r}\left(1+\sum_{n=2}^{\infty}\sum_{m=0}^{n}\left(\frac{a_e}{r}\right)^n P_{nm}\sin\phi(C_{nm}\cos m\lambda + S_{nm}\sin m\lambda)\right) \qquad (2.7)$$

The associated Legendre polynomials $P_{nm}\sin\phi$ can be evaluated separately for each term in the expansion using a recursive formulation where each polynomial is a function of previous polynomials.

The first term in the expansion of Equation 2.7, *GM/r*, is the spherically symmetric gravitational potential at distance *r* from the centre of mass of the Earth, where the Earth is modelled as a point mass. This would be the Earth gravity model applied in a simple, two-body analysis of the orbit. As higher degrees and orders of the expansion are used, the added terms model progressively higher frequency characteristics of the gravitational field waveform. Spacecraft in lower Earth orbits are more sensitive to these higher terms.

Figure 2.2 shows the Earth Centred Inertial (ECI) components of the total acceleration due to Earth's gravitational field on GPS Block IIR and Jason-1 over one orbit. The origin of this frame is fixed at the instantaneous centre of mass of the Earth/atmosphere. More detailed descriptions of this reference frame and other relevant frames are given in Section 2.3 at the end of this chapter.

As the internal mass distribution of the earth is not well known, the geopotential coefficients, C_{nm} and S_{nm} in Equation 2.7 cannot be evaluated directly. They can however be deduced by observing the motion of the satellite and by analysing perturbations to the trajectory. Inversion of this perturbation data generates a solution for the Earth's gravity field.

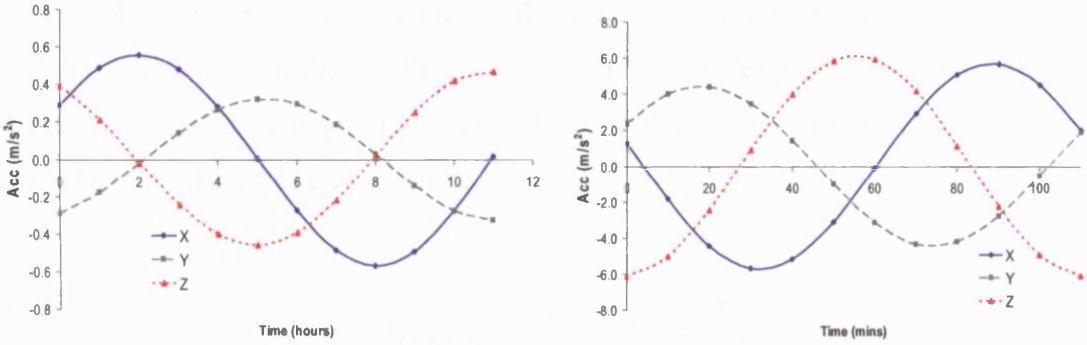

Figure 2.2: Earth's gravitational accelerations: GPS Block IIR (left) and Jason-1 (right)

Many gravity models have been developed in the last decade. Examples include EGM96 (Lemoine, F. et al., 1997) which, at the time, represented a significant milestone in global gravity field modelling. Its development incorporated a plethora of satellite tracking data, satellite altimetry, and the most up to date surface gravity information. Other recent models include JGM3, (Tapley, B. et al., 1996) and GRIM5 (Schwintzer, P. et al., 1999).

The most recent mission dedicated to recovering the gravity field is GRACE, (Gravity Recovery and Climate Experiment), launched in March, 2002 (http://www.csr.utexas.edu/grace/). The GRACE mission involves two identical satellites orbiting one after the other separated by an approximate distance of 200 km. Variations in the gravity field cause variations in the distance between the two satellites; areas of stronger gravity will affect the lead satellite first and accelerate it away from the second satellite. The resulting range variations between the two satellites are measured by a high-accuracy microwave link with a precision better than 10 microns. A highly accurate three-axis accelerometer, located at the satellite mass centre, is used to

measure non-gravitational accelerations. GPS receivers onboard satellites are used to determine the positions of the satellites over the Earth with sub-centimetre level precision and the precise orbit is treated as an a priori observable in the determination of gravity field parameters. The science data from the GRACE mission is used to estimate global mean and time variable gravity maps which are quoted to be superior to previous models by a factor of 200 in terms of precision, (Seeber, G., 2003).

2.2.1.2 Third body effects

Other solar system bodies, such as the Sun, Moon and planets exert their own gravitational forces on the satellite. The perturbing acceleration of a spacecraft in orbit about Earth due to the gravitational field of a third body are developed in Vallado (1997) and are given as (see Figure 2.3):

$$\ddot{\boldsymbol{r}}_{perturbing} = GM_t \left[\frac{\boldsymbol{r}_{sc-t}}{|\boldsymbol{r}_{sc-t}|^3} - \frac{\boldsymbol{r}_t}{|\boldsymbol{r}_t|^3} \right] \tag{2.8}$$

where:

M_t = mass of the third body

r_t = geocentric position vector of the third body

r_{sc}= geocentric position vector of the spacecraft

$r_{sc\text{-}t}$ = vector from spacecraft to third body

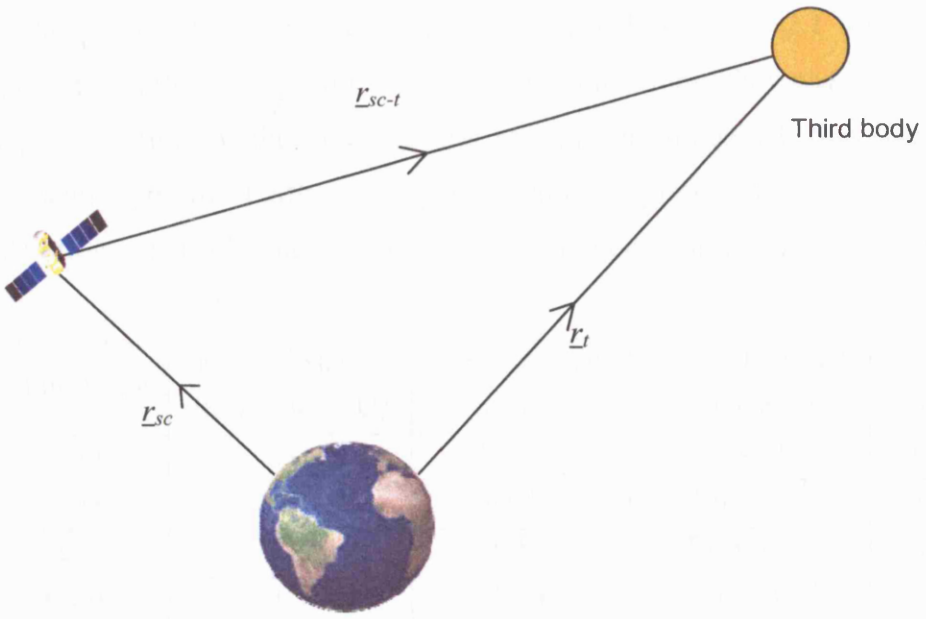

Figure 2.3: Position vectors for the third body perturbing acceleration formulation

As orbit altitude increases, for particular alignments of Earth, probe and third body, these accelerations increase in significance relative to Earth's gravity. At the altitude of a geostationary satellite (~36000km), when the probe lies between the Sun or Moon and the Earth, these forces are comparable to the force caused by the equatorial bulge.

Positions of the Sun, Moon and other planets can be approximated by a set of Chebyshev polynomials (Press, W., 2002). The Jet Propulsion Laboratory (JPL) provide a series of ephemerides for bodies in the solar system in the form of these polynomials known as Developmental Ephemerides (DE). DEs are publicly available and have emerged as a standard for high precision planetary and lunar coordinates (Seidelmann, P., 1992). The most recent versions are DE405 and DE406[2] (Standish, E., 2004) and covers a total of 600 years from 1600 to 2201. The ephemeredes are based on a rigorous numerical integration of the respective equations of motion. Once the positions of these bodies have been generated, their perturbing accelerations can be calculated.

Table 2.1 summarises the mass, distance from the Sun (in astronomical units, AU) and perturbing accelerations of the third bodies for a particular epoch. Perturbations caused by the Sun and Moon are similar in magnitude and require consideration for any precise

[2] DE405 and DE406 are similar, but the accuracy of the interpolating polynomials for DE406 have been lessened.

prediction. The effects of the planets represented in Table 2.1 are ~5-7 orders of magnitude smaller, though for very precise applications, they can become important. Though the effect of the other planets can also be modelled, they are too small to significantly perturb Earth orbiting spacecraft. Figures 2.4 and 2.5 show the ECI accelerations caused by the Sun and the Moon over one orbit (March 2nd, 2004).

Third body	Mean distance from Sun (AU)	Mass in Earth masses	GPS Block IIR acc (ms^{-2})	Jason-1 acc (ms^{-2})
Sun	-	333000	2.5×10^{-6}	6.0×10^{-7}
Moon	1	0.012	3.0×10^{-6}	1.0×10^{-6}
Venus	0.72	0.82	5.0×10^{-12}	1.0×10^{-12}
Mars	1.5	0.11	1.0×10^{-13}	2.0×10^{-14}
Jupiter	5.2	318	2.0×10^{-11}	6.0×10^{-12}

Table 2.1: Planetary data

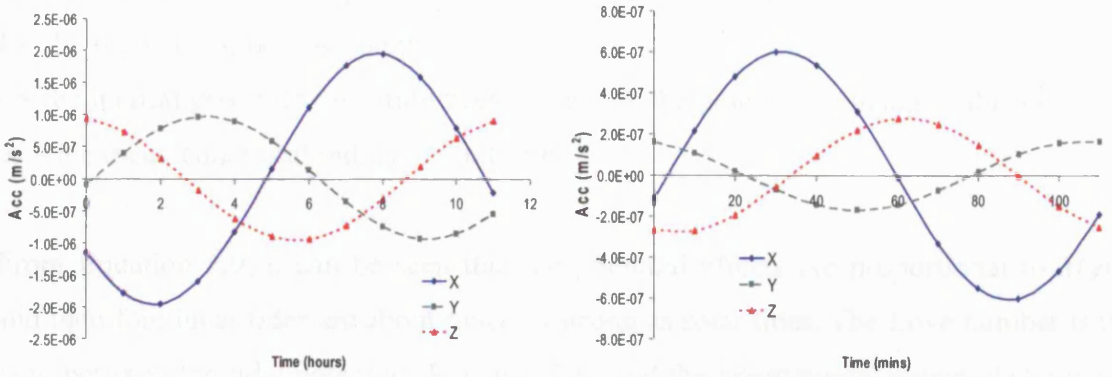

Figure 2.4: Solar gravity accelerations for GPS Block IIR (left) and Jason-1 (right)

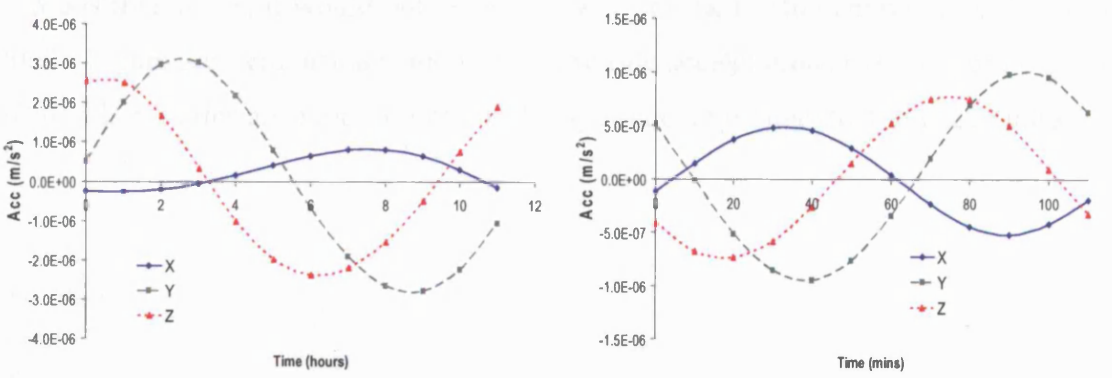

Figure 2.5: Lunar gravity accelerations for GPS Block IIR (left) and Jason-1 (right)

2.2.1.3 Earth tides

The gravity of the Sun and Moon exert direct forces on the Earth's crust leading to small periodic deformations called solid Earth tides. Similar effects on the ocean are known as ocean tides. This movement of mass around the Earth induces a change in the Earth's gravitational potential. The perturbations of satellite orbits from the luni-solar tides are derived by an expansion of the tidal-induced gravity potential using spherical harmonics in a similar way to the static gravity field of the Earth. The second degree expansion of the potential U_B at position vector r (Montenbruck, O. & Gill, E., 2000) due to the gravitational fields of n disturbing bodies is given by:

$$U_B = \sum_{d=1}^{n} \frac{k}{2} \frac{GM_d a_e^2}{r_d^3} \left[\frac{a_e}{r}\right]^3 \left[3\left\{\frac{\boldsymbol{r_d}.\boldsymbol{r}}{r_d r}\right\} - 1\right] \tag{2.9}$$

M_d = the mass of the third body

r_d = the inertial geocentric position vector of the disturbing body

k = the second degree Love number

r = the inertial geocentric position vector at which the potential is being evaluated

a_e = the mean equatorial radius of the Earth

From Equation 2.9, it can be seen that the potential effects are proportional to M_d/r_d^3 and therefore lunar tides are about twice as strong as solar tides. The Love number is the ratio between the tidal potential (Equation 2.9) and the gravitational potential (Equation 2.7) and can be interpreted as a measure of Earth's elasticity and the extent to which it will deform. A value of k = 0.30 is commonly used for the Earth, though for very rigorous treatments, it would not be treated as a constant (Montenbruck, O. & Gill, E., 2000). Figure 2.6 demonstrates the solid Earth tide accelerations over one orbit. Effects of solid Earth tides are about one order of magnitude larger than that of ocean tides.

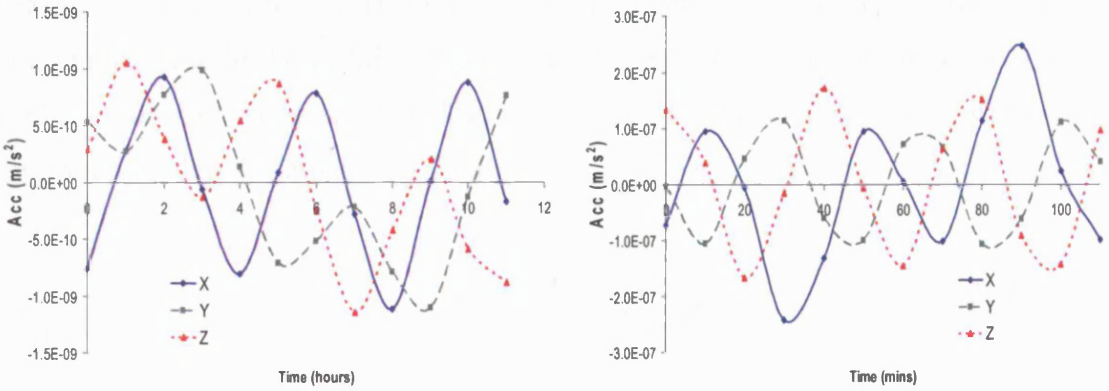

Figure 2.6: Earth tide accelerations for GPS Block IIR (left) and Jason-1 (right)

2.2.1.4 Pole tides

The changing position of the Earth's rotation axis causes the poles to roughly describe a circle of about 20m in diameter. The variation in the direction of the resulting centrifugal forces causes a varying elastic response in the Earth's crust. These are described by corrections to the geopotential coefficients C_{21} and S_{21}. The time varying magnitude of these corrections are calculated by the International Earth Rotation Service (McCarthy, D., 1996). The changes in the Earth's gravity acceleration as a result of the polar tides over one orbit are shown in Figure 2.7.

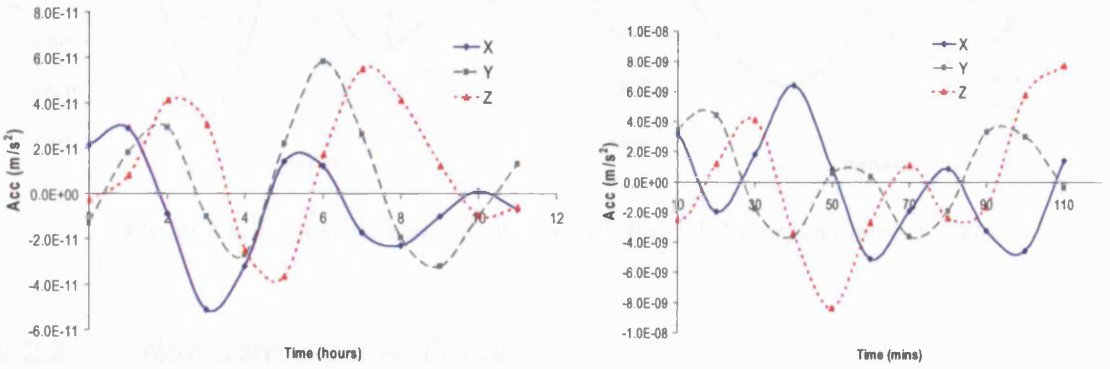

Figure 2.7: Pole tide accelerations for GPS Block IIR (left) and Jason-1 (right).

2.2.1.5 Relativistic effects

For a rigorous treatment of a satellite's trajectory, general relativistic effects require consideration. Though this force is extemely small (see Figure 2.8), it has been included in the analyses later in this thesis and hence is mentioned here.

While the special theory of relativity considers a flat four dimensional space-time, this is no longer true in the vicinity of the Earth. Instead, the Earth's mass M_E and rotation lead to a curvature of space-time. The relativistic correction of the acceleration is given by (Montenbruck, O., & Gill, E., 2000):

$$\ddot{\boldsymbol{r}} = -\frac{GM_E}{r^2}\left(3\frac{v^2}{c^2}\right)\boldsymbol{r} \qquad (2.10)$$

where v is the speed of the satellite and c is the speed of light. This is equal to the product of the Newtonian acceleration and a factor ($3v^2/c^2$) which for a typical satellite equates to about 3 x 10^{-10}ms^{-2}. A fuller treatment can be found in Weinberg (1972) and Hatch, (1995). Figure 2.8 shows the effect of relativistic accelerations on GPS Block IIR and Jason-1.

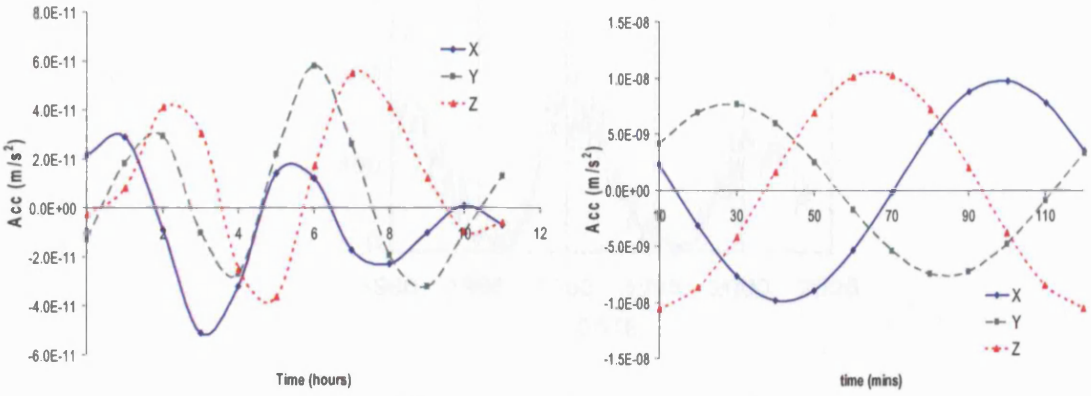

Figure 2.8: Relativistic accelerations for GPS Block IIR (left) and Jason-1 (right).

2.2.2 Non-conservative Forces

2.2.2.1 Solar radiation pressure

Solar radiation pressure (SRP) is the force due to the interaction of solar photons that impact upon the spacecraft surface. When photons strike the spacecraft, they are either absorbed or reflected. The absorbed photons transfer their momentum to the spacecraft, and comprise one component of the SRP force. An additional force arises as the reflected photons, in accordance with the principle of conservation of momentum, cause

a recoil force on the spacecraft. Unlike gravitational accelerations (described in Section 2.2.1), the SRP acceleration depends on the structure, material properties and attitude of the spacecraft. Its magnitude is directly proportional to the area of the spacecraft facing the sun, inversely proportional to the spacecraft mass, and dependent on the surface material properties of the spacecraft. It is also directly proportional to the solar irradiance, the energy flux per unit area at the spacecraft. Solar radiation is emitted over a wide frequency spectrum with a peak energy flux in the visible light. Its energy distribution can be well approximated by a black body radiator of mean temperature 5,785 K. Accounting for all wavelengths of solar radiation, the sun provides a mean energy flux of 1,367 Wm^{-2} (Frolich, C. & Lean, J., 1998) at one astronomical unit, with annual variations of ± 3.3% due to the small eccentricity of the Earth orbit. The solar flux also varies with the 9-14 year solar cycle (as can be seen from the sunspot number variation in Figure 2.9) over a range of ~1.7 Wm^{-2}. These values are known from measurements made by probes in space such as the Solar and Heliospheric Observatory (SOHO).

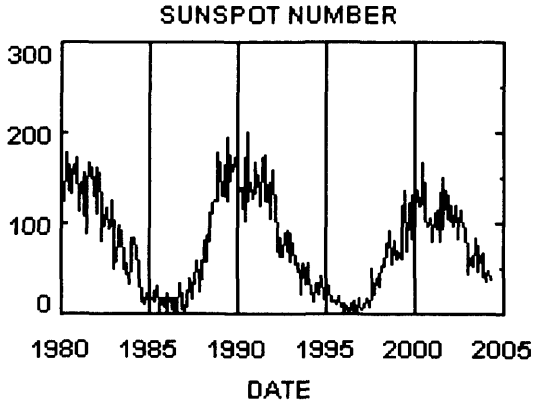

Figure 2.9: Number of sun-spots over 25 years

The main challenge in the evaluation of this force is the calculation of radiation flux incident on each surface. For complicated spacecraft geometries, this becomes difficult, especially when dealing with irregular 3D surfaces and the shadowing of some components by others. Various bodies of work have been carried out to evaluate this force, but there is no "standard approach" as yet. The most detailed method published involves projections of a pixel array onto all possible sun-probe orientations of the spacecraft to simulate the incident solar flux on orbit (Ziebart, M. & Dare, P., 2001; Ziebart, M., 2004a). Figure 2.10 shows the force in ECI coordinates for Jason-1 and

GPS Block IIR using Ziebart's method. The periods when the SRP accelerations fall to zero signify periods spent in eclipse.

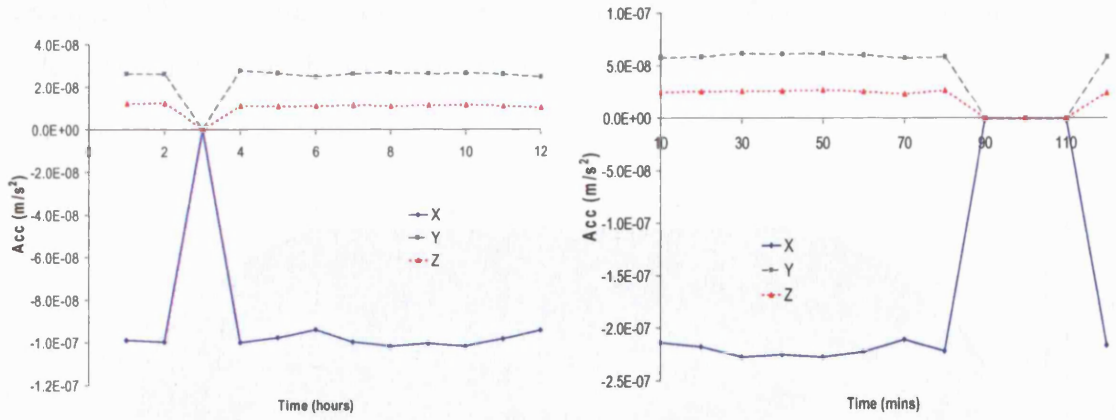

Figure 2.10: SRP accelerations: GPS Block IIR (left) and Jason-1 (right)

This method will be described in more detail in the Chapter 4.

2.2.2.2 Earth radiation pressure

Earth radiation pressure (ERP) refers to the force that results from short wave energy reflected from Earth and the longer wave energy emitted by Earth impacting on the spacecraft surface. The only significant energy source for the Earth is the Sun. When the incoming energy into the illuminated hemisphere is averaged over the whole Earth's surface, the mean incident energy flux is ~350 Wm^{-2}, of which approximately one third is reflected in the visible part of the spectrum (~25% reflected by cloud, and ~7% reflected by continents and oceans) and the rest of the incident energy is absorbed by the atmosphere, soil and water. The absorbed energy is then re-emitted mainly as infra-red radiation, and this thermal component causes the Earth to appear as a black body radiator of mean temperature 253 K. The physical modelling is similar to SRP in that the force is produced by the interaction of electromagnetic radiation and the spacecraft surface. The fundamental difference between the two effects is in the modelling of the radiation source. For SRP the solar irradiance is fairly stable and can be considered constant over a few orbits (provided scaling for the probe-sun distance is considered). On the other hand the ERP flux will vary significantly over an orbit, and is complicated to model a priori because of its dependence on many highly changeable environmental

variables, such as cloud and land cover (vegetation, land, water, ice) below the satellite as it orbits Earth. Figure 2.11 shows the monthly averaged short wavelength (visible) radiation from Earth (Ziebart, M. et al., 2004b), which was derived from Climate Experiment Radiation Environment System (CERES) data (Wielicki, B. et al., 1996) for January, 2001. The fluxes are shown at an altitude of 30km above the Earth's surface, which is referred to as the top of the atmosphere (TOA).

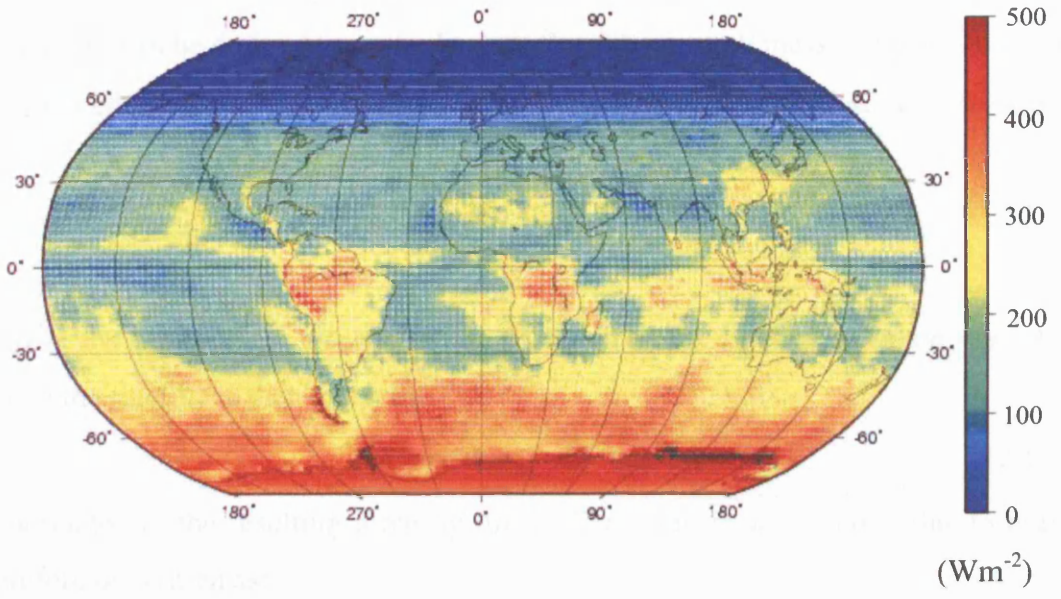

Figure 2.11: Shortwave radiation emitted from TOA, January, 2001.

Research into modelling this force has recently sparked much interest amongst the orbit modelling community, and, as for SRP, different approaches are in use, most of which are fairly crude.

The greater the altitude of the satellite, the smaller the albedo effect, due to the "inverse square law" fall off in flux density. The size of ERP acceleration is ~ 10^{-8} ms^{-2} for Jason-1, and ~$10^{-9}ms^{-2}$ for GPS spacecraft. A graph for Jason-1 is not shown as processing the data for this was beyond the scope of this thesis.

2.2.2.3 Atmospheric drag

Atmospheric forces generally represent the largest non-gravitational perturbations acting on satellites at low altitude. For low Earth orbiting satellites (up to ~2000km)

drag is a significant problem which must be considered for precise orbit determination. For the lowest orbiters (at altitudes of ~250km) drag can cause decelerations of the order of 10^{-5} ms^{-2}, and at 800 km, decelerations have values ~ $10^{-7}ms^{-2}$. For medium Earth orbiters, for example GPS satellites at an altitude of ~20000km, the atmosphere is conventionally considered as sufficiently rarefied for drag to be ignored (Jacchia, L., 1977).

The dependence of the drag force on the velocity of the object relative to the atmosphere, v_r, can be derived in a simple way. Consider a small mass element Δm of an atmosphere column that hits the satellite cross-sectional area A in some time interval Δt. Then:

$$\Delta m = \rho A v_r \Delta t \tag{2.11}$$

where ρ is the atmospheric density at the location of the satellite. The impulse Δp exerted on the satellite is then given by

$$\Delta p = \Delta m v_r = \rho A v_r^2 \Delta t \tag{2.12}$$

which is related to the resulting force by $\Delta p/\Delta t$. The satellite acceleration due to drag can therefore be written as:

$$\ddot{\underline{r}} = -\frac{1}{2} C_d \frac{A}{m} \rho v_r^2 \underline{u}_v \tag{2.13}$$

where m is the spacecraft mass and $\underline{u}_v$ is the unit relative velocity vector. The drag coefficient C_D is a dimensionless coefficient which describes the interaction of the atmosphere with the satellite's surface material, and typical values range from 1.5-3.0 (Montenbruck, O. & Gill, E., 2000)[3]. This coefficient depends on the interaction of the atmospheric constituents with the satellite surface. Accurate modelling of this is a challenging task. Firstly, the complex properties and dynamics of the Earth's atmosphere are required; for the upper atmosphere (> ~100km), these are not well known. Secondly, modelling these forces requires detailed knowledge of the interaction of neutral gas as well as charged particles with the different spacecraft surfaces. Thirdly, the cross-sectional area of the satellite presented to the particle flux must always be

[3] The factor ½ is conventionally included in Equation 2.13, so that the equation resembles the functional form of other equations in aerodynamics.

known. Over the last three decades extensive effort has been devoted to developing models of the atmosphere at high altitudes, though recent progress has been fairly modest and it is still an area of ongoing research. As the atmospheric densities and the drag coefficient are so difficult to quantify in the upper atmosphere, it is commonly estimated as a free parameter in orbit determination programs.

2.2.2.4 Thermal re-radiation

A satellite absorbs energy, then re-emits it anisotropically as heat. When a surface emits energy, the law of conservation of momentum requires an equal but opposite force to act on that surface. As the main topic of this thesis, thermal re-radiation will be described in more detail in Chapter 3.

2.2.2.5 Antenna thrust

Aside from the natural forces described so far, the motion of a spacecraft can also be affected by self-generated forces. Man-made satellites communicate with Earth by the transmission of electromagnetic signals via antennas mounted on the outside of the spacecraft. The emission of these signals causes a recoil force on the spacecraft, which can be determined from the power with which the signal is emitted as shown in Equation 2.14.

$$F = \frac{P}{c} \tag{2.14}$$

where P is the signal power and c is the speed of light in a vacuum. If the signal is emitted continuously, as is the case for many satellites, a constant force acting in the orbit radial direction will result and may have considerable effects on the orbit of the spacecraft. For a GPS satellite, the signal strength is about 77W which translates into a constant acceleration of about 2.5×10^{-10} ms^{-2}. This can cause a maximum displacement to a spacecraft at the 0.5m level for one 12 hour orbit.

2.3 Co-ordinate Systems

The definition of an appropriate co-ordinate system in order to study a particular physical phenomenon requires careful consideration in satellite geodesy. In order to model and analyse the orbits of spacecraft we require a number of different co-ordinate systems, and those used in this thesis are described below. They fall into two types:

those whose origin is at the centre of mass of the Earth and atmosphere and those whose origin is fixed relative to the spacecraft. Earth-centred frames are of two principal types: inertial and rotating. The former is termed Earth-Centred Inertial (ECI) and the latter is termed Earth-Centred Earth-Fixed (ECEF).

2.3.1 Earth-Centred Inertial (ECI)

An ECI frame approximates the inertial frame postulated by Sir Isaac Newton, within which Newton's equations of motion are valid, and is defined by a right-handed, cartesian basis. The X and Y axes typically lie in the Earth's equator, and the Z axis is aligned with the angular momentum axis of the earth, but since they move in inertial space due to nutation and precession, there are effectively an infinite number of ECI frames. Conventionally, ECI frames are defined in space by fixing them to an epoch. Currently the most widely used frame is J2000, which is the ECI frame as defined at 12.0 hours UT[4], 1st January 2000. ECI axes are conventionally labelled IJK. The I-axis points along the intersection of the equator and the ecliptic, a direction defined as the Vernal equinox. The J-axis is 90° east of I in the equatorial plane. The K-axis completes the right-handed set.

2.3.2 Earth-Centred Earth-Fixed (ECEF)

This frame is non-inertial due to the Earth's diurnal rotation. Conventionally, the ECEF system is a right handed cartesian basis, and its axes are labelled XYZ. The definition of an ECEF frame is complicated by the fact that reference stations fixed to the surface of the Earth are moving continuously with respect to each other due to phenomena such as tectonic activity and post glacial rebound. Nominally an ECEF frame has the X-axis in the equatorial plane passing through some point close to the Greenwich meridian; the Y-axis is also in the equatorial plane and is 90° East of the X-axis and the Z-axis completes the right-handed set. The frame realisation is through the co-ordinates of a number of reference stations. There are many ECEF frames. This study uses the International Terrestrial Reference Frame (ITRF) as defined by the positions and velocities of several hundred core stations. Conversion from the ECI (eg J2000 to the ECEF frame, eg ITRF) requires a transformation that accounts for polar motion, (to

[4] UT = Universal Time

align the Z-axes of the frames), Greenwich Apparent Sidereal Time (to align the X axes) and nutation and precession of the ECEF frame.

2.3.3 Spacecraft Body-Fixed Co-ordinate system (BFS)

There is no formal definition for this system, though general conventions do exist. The BFS axes defined for GPS Block IIR and Jason-1 are presented here.

For GPS Block IIR, the BFS axes are a right-handed cartesian basis with the origin at the spacecraft centre of mass. The antenna boresight is defined as a direction along the central bus longitudinal axis, pointing in the same direction as the navigation signal antennae. The body-fixed Z-axis is co-incident with the antenna boresight. The spacecraft Y-axis is parallel to the solar panel support boom arm, and the X-axis completes the right-handed set. This is demonstrated in Figures 2.12.

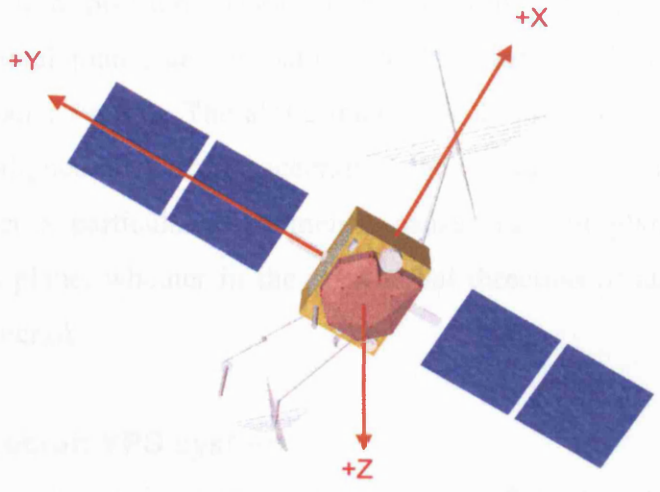

Figure 2.12: GPS Block IIR showing BFS XYZ axes

For Jason-1, the BFS origin is not at the centre of mass, but translated to the base of the spacecraft as shown in Figure 2.13.

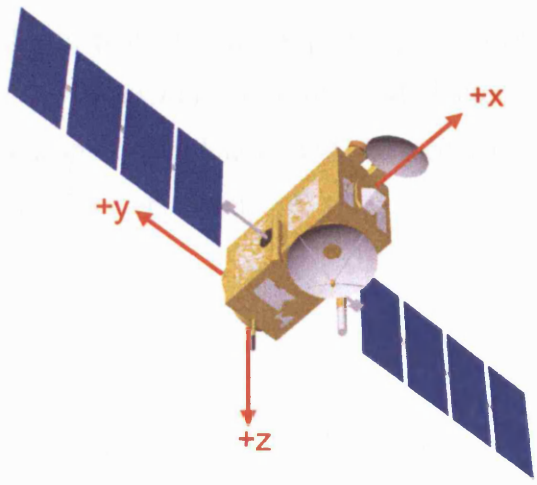

Figure 2.13: Jason-1 showing BFS XYZ axes

2.3.4 Spacecraft Height/Cross-track/Along-track system (HCL)

The HCL basis is centred on the spacecraft centre of mass. The H-axis is parallel to the spacecraft geocentric position vector. The C-axis is orthogonal to the satellite's instantaneous orbital plane, and is parallel to the cross product of the spacecraft's position and velocity vectors. The along track axis, L, completes the right-handed set and is roughly aligned with the spacecraft velocity vector. This basis is useful for analysing whether a particular phenomenon causes in-orbit plane/out-of-orbit plane effects and, if in plane, whether in the orbit radial direction or along the direction of travel of the spacecraft.

2.3.5 Spacecraft YPS system

This basis also has its origin at the nominal spacecraft centre of mass. This basis is satellite specific; taking GPS Block IIR as an example: the PS-axis is parallel to the probe-Sun vector and the Y-axis is parallel to the solar panel boom arm and is calculated as the unit vector parallel to the cross product of the spacecraft BFS Z-axis and the PS-axis. The YPS basis right-handed set is completed with a Z-axis. This axes system is useful when analysing effects which are expected to be related to sun direction.

Summary

Both gravitational and non-gravitational forces have significant effects on the spacecraft orbits. In this chapter the origin of these forces, approaches to their modelling and estimates of their effects have been given. In the next chapter, the force due to thermal re-radiation is presented in more detail, and the different approaches that have previously been used to model it are discussed.

Chapter 3 Thermal re-radiation modelling

Chapter outline

In this chapter the nature of the thermal re-radiation force and its mathematical formulation are described. The different approaches to modelling in the context of orbit computations are explained and a review of relevant bodies of work carried out so far on this topic is presented.

3.1 Basis of TRR force

Modelling of the thermal forces arising from the interaction of the spacecraft with its environment requires understanding the physical laws which govern heat transfer. Two types of heat transfer processes are pertinent for this study of the spacecraft surface: radiation and heat conduction. A third heat transfer mechanism, convection, involves fluid particle motion; though this is a relevant heat transfer mechanism within some parts of the spacecraft, it does not apply to satellite surfaces.

When radiation interacts with matter it is subject to three possible outcomes; reflection, transmission or absorption. If energy is reflected or transmitted, the thermal energy of the matter is unaffected. If energy is absorbed, it can be incorporated as thermal energy, causing a change in the electron configuration of the constituent atoms or molecules and resulting in an increase in temperature. Usually a combination of the above processes occur and the relative amounts of each depend on the material properties of the body upon which the radiation is incident, namely the reflectivity, absorptivity and the transmission coefficients. These parameters range between 0 and 1 and give the fraction of radiation that is reflected, absorbed or transmitted at a particular wavelength.

Matter also emits radiation. The emission may again be attributed to the changes in the electron configuration of the material. The energy radiated is in the form of electromagnetic waves in the infra-red (~5-1000 μm) part of the spectrum. The rate at

which energy is released per unit area (Wm^{-2}) is termed the surface emissive power E. This has an upper limit which is prescribed by the Stefan-Boltzmann law:

$$E = \sigma T^4$$

where T is the absolute temperature of the surface and σ is the Stefan-Boltzmann constant (5.6699×10^{-9} $Wm^{-2}K^{-4}$). Such a surface is called an ideal radiator or a blackbody. The energy radiated by a real body is less than this, and is given by

$$E = \varepsilon \sigma T^4 \tag{3.1}$$

where ε is the emissivity of the body (Incropera, F. & DeWitt, D., 2001). The emissivity ranges between 0 and 1, and is a measure of how efficiently energy is radiated by a body.

According to Einstein's theory of special relativity, there is an equivalence between mass and energy. One implication of this is that emitted photons have momentum. The law of conservation of momentum dictates that a net momentum flux out of the body causes a reaction force against the satellite's heated surface. This is the force due to TRR and forms the basis of this study.

The sun is the primary source of radiation for a satellite; smaller sources include the Earth and moon. Differential heating occurs between parts of a spacecraft which are irradiated and those which are not. Some deep space probes spin specifically to distribute the heat load evenly, but most Earth orbiting spacecraft cannot do this because of attitude constraints. Taking GPS spacecraft as an example, the +Z face upon which the antennas are mounted must always point to Earth, while the body and panels rotate in such a way so that the panels always face the sun. As a result, different components receive different amounts of radiation depending on whether they are sun-facing or not and the extent to which they are shadowed by other components. The amount of energy absorbed and emitted by each component is determined by its material and optical properties, so surface temperatures may differ considerably. Since the surface components of a satellite will radiate at a rate proportional to temperature and emissivity, the resulting emission will most likely be anisotropic (Figure 3.1), and lead to a resultant force.

Another source of environmental heating is due to friction with particles in the rarefied upper atmosphere under a free molecular regime, though this heating is usually only significant during the launch phase (Gilmore, D., 1994). Internal subsystems are a source of heat within the spacecraft bus. This heat is vented to space via radiators or louvers on the surface of the bus. This emission will also produce a recoil force, and should be included in any rigorous calculation. To account correctly for this depends on the accessibility of thermal budget data, which may be available in engineering data sets for specific satellites.

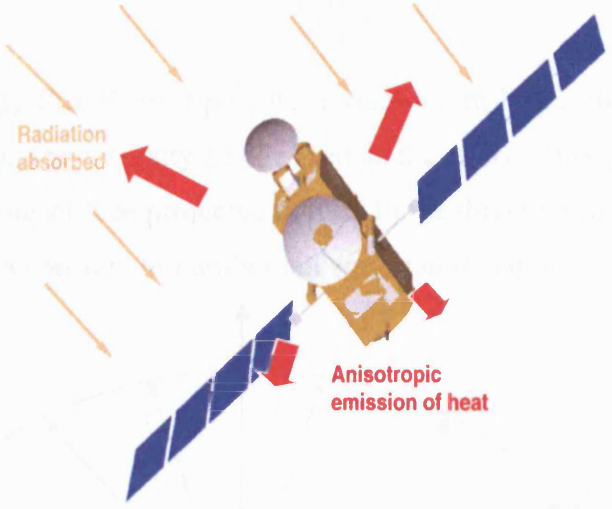

Figure 3.1: Anisotropic emission of radiation by the satellite

3.2 Characterisation of Force

Einstein's theory of relativity describes the energy of a particle as

$$E = \left[(cp)^2 + \left(m_0 c^2 \right)^2 \right]^{\frac{1}{2}}$$

where E is the energy of the particle, p is the momentum and m_0 is the rest mass. For a photon, $m_0 = 0$, and hence $E=cp$. Dividing the total energy that is radiated by a surface each second by the speed of light gives the total momentum transferred away from the surface each second:

$$\frac{dp}{dt} = \frac{E}{c} = \frac{\varepsilon \sigma T^4}{c}$$

The law of conservation of momentum causes a recoil force on the spacecraft which is equal and opposite in direction to the momentum leaving the surface per second, which

is the thermal re-radiation force. To calculate the magnitude of this force, the directional distribution of the emitted radiation must be known.

If the body is treated as a diffuse radiator (which is a reasonable approximation for many surfaces (Incropera, F. & DeWitt, D., 2001), Lambert's Law can be applied (Chapman, A., 1984). Lambert's law states that for a diffuse radiator the energy flux (Wm^{-2}) going through a point P varies as the cosine of the angle between that direction and the normal vector of the surface element Q, and inversely with the square of the distance between the source and the point:

$$E_P = \frac{I \cos\theta}{r^2} \tag{3.2}$$

where E_P is the energy flux (Wm^{-2}) passing through point P at a distance r away from the emitting source Q. The intensity I is defined as the energy flux per unit solid angle, per unit area of emitting surface projected normal to the direction in which the energy is travelling, and this is a constant in Lambertian emission (Chapman, A., 1984).

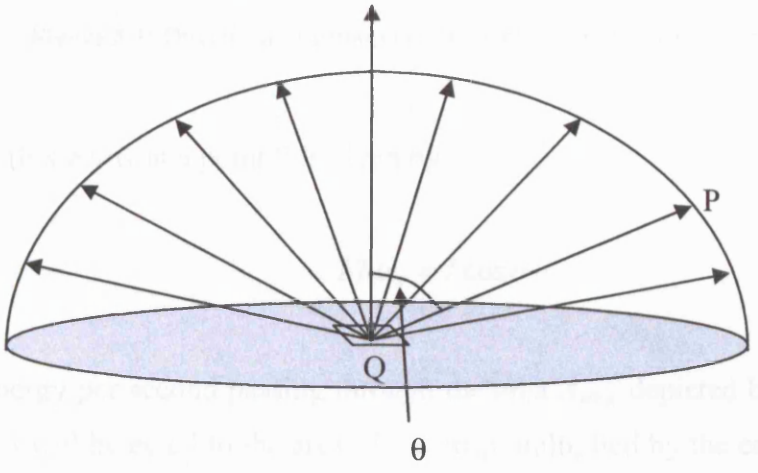

Figure 3.2: Diffuse emission from a surface

The forces which arise from emission can be resolved into components parallel and perpendicular to the surface. A Lambert emitter is azimuthally symmetric in its emission (constant amount of radiation emitted at particular value of θ), hence the components parallel to the surface will cancel out, and it is only necessary to calculate the resultant force perpendicular to the emitting surface. This flux is calculated by summing the components of the flux in the normal direction.

Figure 3.2 shows a hemisphere with unit radius above an emitting point source. The energy flux through a point P on the surface of the hemisphere is given by

$$E_P = I\cos\theta \tag{3.3}$$

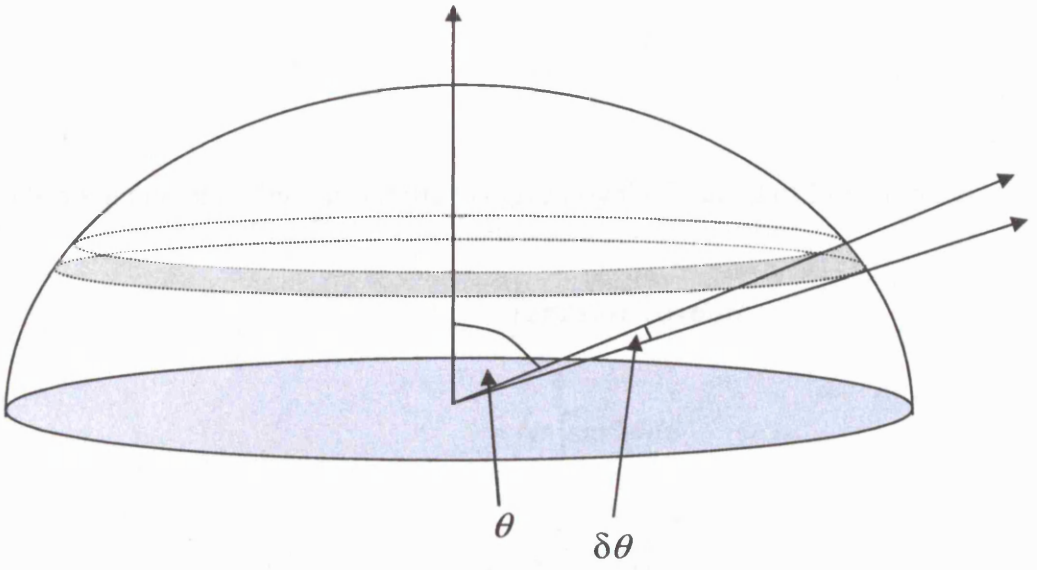

Figure 3.3: Directional distribution of radiant energy from a point source

The energy flux $Flux_P$ at a point P is given by:

$$Flux_P = I\cos\theta \tag{3.4}$$

The total energy per second passing through the area A_{strip} depicted by the shaded strip in Figure 3.3 will be equal to the area of the strip multiplied by the energy flux at point P. The area of the strip shown in Figure 3.3 is:

$$A_{strip} = 2\pi\sin\theta\delta\theta \tag{3.5}$$

and the energy per second passing through this strip is therefore:

$$E_{strip} = 2\pi I\sin\theta\cos\theta\delta\theta \tag{3.6}$$

The component of this energy flux normal to the emitting surface is:

$$E_{perp} = 2\pi I\sin\theta\cos^2\theta\delta\theta \tag{3.7}$$

E_{perp} describes the normal component of energy passing through the strip per second. The total perpendicular component arising from the whole hemisphere is found by integration over the range of θ.

$$E_{perp} = \int_0^{\frac{\pi}{2}} 2\pi I \sin\theta \cos^2\theta d\theta \tag{3.8}$$

$$E_{perp} = -\frac{2\pi I}{3}\left[\cos^3\theta\right]_0^{\frac{\pi}{2}} \tag{3.9}$$

$$E_{perp} = \frac{2\pi I}{3} \tag{3.10}$$

The total amount of energy emitted is given by the integral of Equation 3.6

$$E_{tot} = \int 2\pi I \sin\theta \cos\theta d\theta \tag{3.11}$$

$$= I\pi \int_0^{\frac{\pi}{2}} \sin 2\theta d\theta \tag{3.12}$$

$$= -\pi\left[\frac{\cos 2\theta}{2}\right]_0^{\frac{\pi}{2}} \tag{3.13}$$

$$= I\pi \tag{3.14}$$

Therefore the energy emitted perpendicular to the surface as a fraction of the total energy emitted can be written as

$$\frac{\left(\frac{2I\pi}{3}\right)}{I\pi} \tag{3.15}$$

$$= \frac{2}{3} \tag{3.16}$$

Combining this with Equation 3.1 gives the amount of energy emitted perpendicular to the surface as

$$\frac{2\varepsilon\sigma T^4}{3} \tag{3.17}$$

The corresponding momentum transferred to the body per unit area of surface is then given by

$$\frac{2\varepsilon\sigma T^4}{3c} \tag{3.18}$$

and the recoil force on the surface of area A is

$$-\frac{2A\varepsilon\sigma T^4}{3c} \tag{3.19}$$

In order to find the complete thermal force on a body, this differential force must be integrated over the entire surface.

$$\underline{F}_{thermal} = -\frac{2}{3c}\int_{\Omega}\varepsilon\sigma T_A^{\,4}\,d\underline{A}$$

The problem reduces to acquiring knowledge of the emissivities and the determination of temperatures for each part of the satellite surface. The temperatures must be accurately determined since the force is proportional to the fourth power of the temperatures.

3.3 Existing approaches to thermal modelling

Before reviewing existing work on the topic of thermal re-radiation, the two general approaches - analytical modelling and empirical modelling- used to account for this force in orbit computations are discussed. The most appropriate method to use is dependent upon the data available, the orbit precision required, and what knowledge is desired at the end of the process.

3.3.1 Analytical modelling

An a priori mathematical model of the forces is constructed based solely on a physical analysis of the problem. The precision of this analytical force model is highly dependent on the accuracy of the data describing the environment, the spacecraft attitude, and the structural and material properties of the spacecraft. In orbit processing, model complexity is an issue, and a trade off must be made between accuracy of model and computational burden. This poses another limit to the usability of accurate a priori models.

3.3.2 Empirical modelling

Limitations of analytical models have led orbit determination agencies to employ empirical techniques to account for un-modelled forces. In empirical modelling, an a priori force model is used to create an initial estimate of the orbit. This estimate will be improved by using observation data, for example tracking data from ground stations, to constrain the trajectory. A linearised least-squares process is employed to adjust the

initial conditions and selected model parameters (eg. solar irradiance or atmospheric drag coefficients) to decrease the discrepancy between the observations and the computed orbit. The final trajectory of the satellite should be consistent with the physics of the mathematical model and the series of observations used. In the estimation process, two methods are used to carry out empirical adjustments: scaling and augmentation. These strategies are described in the following sections.

3.3.2.1 Scale factor determination

Where scaling is applied it is assumed that some parameter inherent in the a priori model has the correct form for the satellite orbit, but an incorrect magnitude. This might be, for example, due to errors in parameters such as the solar irradiance, or ill defined optical properties of a surface material. A scale factor is used to inflate or deflate a particular parameter in the a priori model, which is suspected to be a cause of some mis-modelling, in order to minimise the discrepancy between the system dynamics and the observed data and to reduce errors in other parameters which are solved for.

3.3.2.2 Augmentation

In empirical augmentation, extra parameters are added to the a priori model which do not necessarily represent a known physical effect. As an example the so-called Y-bias effect (Fliegel, H. et al., 1992) is considered. When precise orbits were first being estimated for GPS it was assumed that the attitude control algorithm and broadly symmetrical structure of the spacecraft in the X-Z plane implied that no component of the SRP force would act along the spacecraft Y-axis. In practice, it was found that empirically estimating a small force acting along the Y-axis improved the results. The physical mechanism causing this effect was not understood, but could have been due to panel misalignment, small departures from the nominal attitude of the spacecraft, or asymmetric venting of heat through the radiators on the ± Y faces (Figure 3.4).

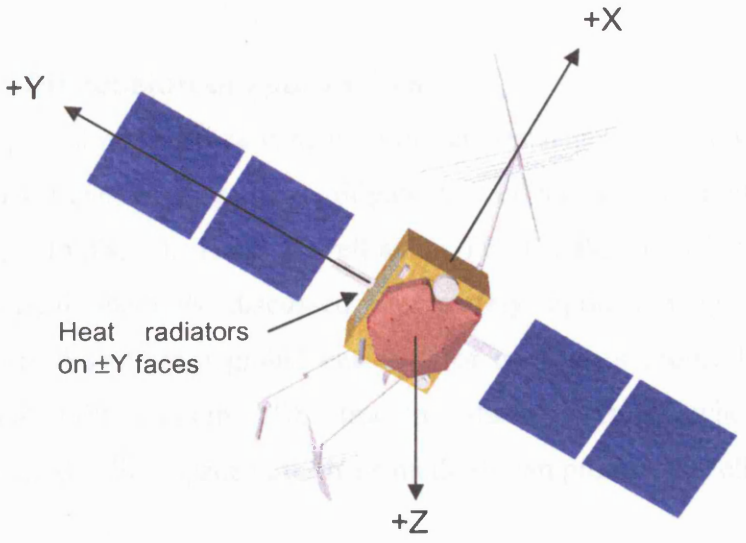

Figure 3.4: GPS Block IIR spacecraft showing body fixed system axes

Un-modelled effects are often expected to have a frequency of once per orbit revolution, so parameters with this periodicity, along with constant terms are estimated. The direction of empirical accelerations are commonly specified in a body fixed frame, either HCL, YPS, or along the spacecraft X, Y and Z axes.

An example of a developed augmentation approach is that used by Centre for Orbit Determination in Europe (CODE) for GPS spacecraft. Here the solar radiation pressure and thermal effects are combined and described by a set of parameters (Beutler, G. et al., 1994). Their model uses various combinations of parameters estimated with respect to a spacecraft-fixed YPS basis. For each axis, CODE estimate a constant acceleration for each 12-hour orbit, with once-per-revolution sine and cosine terms superimposed. Hence, in the CODE approach nine SRP and thermal parameters are estimated per orbit of the Earth. This approach has been applied to GPS spacecraft.

The Jet Propulsion Laboratory (JPL), on the other hand, estimate 5 SRP and TRR parameters in the body-fixed frame for GPS Block IIR. (Gregorius, T.,1996). In an analysis carried out by Vigue (1994b), GPS orbits were estimated using 5 SRP parameters, all in the body-fixed frame. Two of these are constant scale factors, one parameter for along the y-axis and one that is combined constant factor for the X and Z

direction. The additional 3 parameters are varying scale factors for each body fixed X, Y and Z axes that are estimated sequentially.

3.3.3 Discussion of approaches

These empirical approaches can, in some circumstances, work very well. They have successfully been employed to mitigate the effects of force model errors of GPS satellites (Colombo, O., 1989) as well as for TOPEX/Poseidon (Tapley, B., et al. 1994). The empirical methods discussed above rely upon having a large number of observations drawn from global networks of tracking stations. In the context of the International GPS System (IGS) tracking station network where over 200 ground stations track the GPS spacecraft, these methods can produce excellent results.

They are still however limited in the accuracy with which they can replicate the true orbit and, as precision requirements increase, better a priori dynamic models are required as a start point. A more accurate a priori physical model benefits orbit determination because it provides the correct form of the function, which will then be augmented or scaled. A poorer a priori model will require more empirical parameters, and reduce the redundancy of the observation data.

A drawback of solving for such empirical terms is that there is a tendency for estimated parameters to absorb any unmodelled effects. If these effects have a time or spatial dependency that is uncorrelated with the signature of the force in question, then this can not be used to deduce the effect of this force at future epochs. In these cases, no physical significance can be associated with the effect. As many effects are assumed to have a once per orbit revolution period and as such are modelled with once per revolution empirical parameters, they may be inadequate to correctly account for un-modelled effects with different periodicities (Ziebart, M. et al., 2003a).

Problems can arise when empirical terms are used to soak up un-modelled parameters which correlate with other effects. In orbit determination of GPS satellites, parameters which impact on the measurement data are estimated; an example is tropospheric zenith delay (TZD), which is the attenuation of a signal caused by atmospheric water vapour. This parameter is required by other scientists in fields such as climatology and weather prediction. If a bias is suspected in the range to a GPS spacecraft due to an un-modelled

effect in the a priori model, eg earth radiation pressure, a scale factor could be introduced along the spacecraft body-fixed Z-axis to account for it. This scale factor will soak up all radial errors including some of the effect caused by the TZD. The estimation of the TZD then will be less accurate as part of its effect has been absorbed by the scale parameter. This example shows what is to be gained by having an accurate a priori force model. The more accurate the model, the more highly constrained are the errors in other parameters.

Whilst empirical parameterisation of orbits is an approach that is well suited to a posteriori orbit determination when much tracking data is available, applying empirical acceleration parameters for orbit prediction purposes may lead to a substantial degradation of the position accuracy.

3.4 Review of relevant literature

The structural complexity and lack of reliable data of a real spacecraft makes any accurate calculation of the thermal force a difficult task. This fact, coupled with the relatively low ranking of surface thermal effects in the hierarchy of forces that affect the motion of a spacecraft, has resulted in this force receiving little detailed attention. Increasingly however, GNSS applications require greater precisions, and modelling of smaller forces are becoming more important. This section summarises the material that has been published in this area so far in the context of spacecraft orbits. A review of the available literature on eclipse boundary determination is also given, and the main bodies of work carried out on the other non-conservative forces are outlined.

3.4.1 Thermal re-radiation

In the late 1980s, several studies were undertaken to investigate the size of the thermal force and its impact on various spacecraft. Slabinski (1988) provides an introduction to the theoretical background of thermal imbalance forces, and demonstrates that thermal re-radiation could be significant in explaining the observed drag effects for deactivated telecommunication satellites. Rubincam (1987) shows that the thermal behaviour of retro-reflectors embedded in the surface of LAGEOS, a small, spherical, spinning satellite, would explain the observed drag like behaviour of the satellite, thus establishing that thermal forces were indeed big enough to perturb the motion of a

satellite. The simple structure of LAGEOS, and its continuous rotation enables a relatively straightforward calculation of the thermal force, but as the spacecraft structural complexity increases, so does the effort required in producing accurate thermal models.

In a thesis by Cook (1989) the surface thermal forces on simple spacecraft models such as box and wing (see Figure 3.5) and spherical bus models are estimated, thus avoiding the issue of spacecraft complexity. The purpose of Cooke's study was to estimate maximum possible displacements that could occur due to this force. His discussion concentrates on a number of idealised situations, for example, the spacecraft is modelled as a perfectly conducting slab with a constant sun facing profile on orbit. His study predicts that this force could result in metre level radial errors in 14 days, and up to tens of metres along track. He suggests that, though estimation of other force model parameters (such as SRP) would probably absorb much of the error, significant discrepancies might still occur.

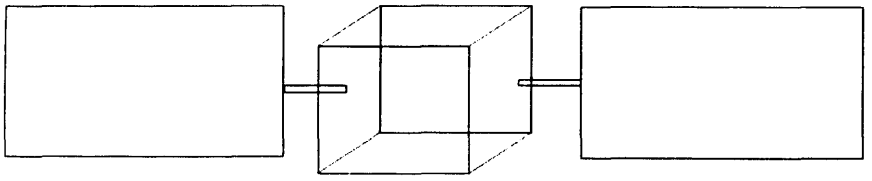

Figure 3.5: Simplified spacecraft structure: Box and Wing model

Vigue (1994a) presents the most detailed methods published for analysing the perturbations due to the thermal force, specifically to determine the long term effects on the behaviour of GPS Block IIA satellites. Vigue argues that a thermal model of the entire spacecraft would be very complicated due to the complex geometry and poorly defined material properties which strongly affect the magnitude of the forces. She asserts that as the solar panel areas are large compared to the bus areas and constantly face the sun, their effect would dominate the thermal force, and hence she does not consider the spacecraft body. Using the material properties for each layer of the panel, she employs finite element method software to study the one dimensional heat transfer through the panel. This yields the temperatures for the front and back face which are then used to calculate a force. A ball park figure for the thermal acceleration of 1×10^{-9} ms^{-2} was estimated. She analyses the effect of the thermal force by comparing

numerically integrated orbits: one with two body effects only and the other with two body effects and the thermal force. The residuals grow to the metre level after a day, in both the radial and along track directions.

In this paper, she also examines how well solar pressure scale factors can absorb thermal effects and finds that though a large proportion can indeed be absorbed, the remaining signals are significant. She ultimately concludes that as the thermal force is dependent on many properties which cannot be well known, it may be more appropriate to estimate empirical parameters to represent it. Though this work was progressive at the time, in that it was the first detailed study to try and predict the effects of this force for a real spacecraft, it had two main drawbacks: 1) the spacecraft bus was totally ignored, with no supporting analysis and 2) no testing was carried out to see whether these models were correct or whether they improved orbit prediction/determination capabilities.

Rockwell International, the spacecraft contractors for the GPS Block I and II/IIA spacecraft developed SRP models for their satellites. The computer code to deal with them was written by IBM and amended by the Aerospace Corporation, and became known as the Rock models. To begin with, these models totally ignored the effects of thermal re-radiation. In a paper by Fliegel & Gallini (1996) of the Aerospace Corporation, it was stated that the thermal force was indeed significant and accounted for ~5% of the solar force. The Rock models for the Block II spacecraft were then amended to include these effects and renamed as the T20 models. Similar models for GPS Block IIR (which had extra antennas) are known as T30. The thermal forces were absorbed into the SRP models directly. Fliegel's papers (Fliegel, H. et al., 1992, Fliegel, H. & Gallini, T., 1996) describe the processes used in the calculation of the models and outline their main assumptions and weaknesses. The spacecraft surface is treated as a set of surfaces, which are assumed to be either flat or cylindrical. The SRP force is calculated on a component by component basis, where the interaction of the component with incoming photons is computed as a function of angle of incidence, and the results are summed over the whole spacecraft. Specular and diffuse SRP effects are modelled, and the effect of shadowing of one component by another is accounted for. The method does not allow for the effect of light reflected from one surface striking another. The method also becomes progressively more impractical as the complexity of the

spacecraft structure increases. The models consist of Fourier series of accelerations as a function of the angle between the spacecraft z-axis and the probe-sun line (Earth-Probe-Sun, (EPS) angle) for the x and z axes. The EPS angle is shown in Figure 3.6.

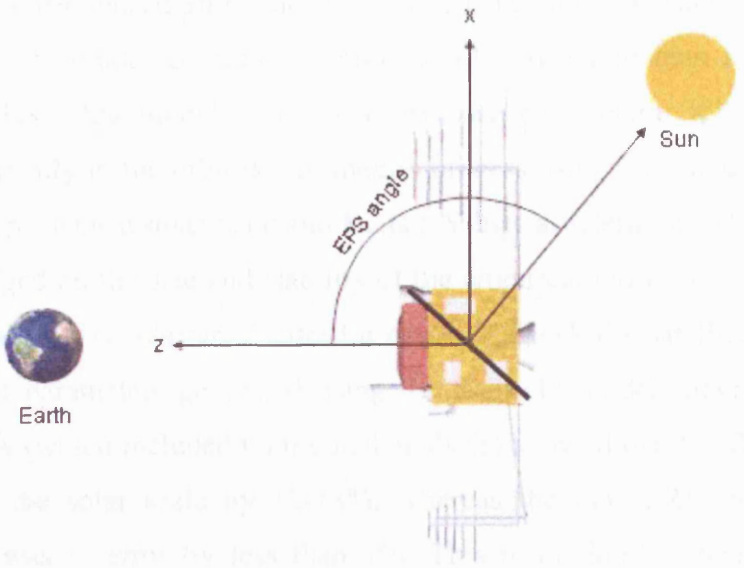

Figure 3.6: Earth-Probe-Sun angle

The thermal analysis considers both the panels and the spacecraft bus surfaces and the GPS Block IIR material and optical properties used in the analysis are given. These models give errors in orbit prediction of 3-4m after 12 hours along track, and a 0.5m error in height. Fliegel recognised that these levels of precision were unacceptable for geophysical work, and recommended that the models be constrained using tracking data to produce more precise orbits. Though the models developed incorporated a reasonable level of detail, they can only be applied to GPS spacecraft; no generalised method is described so no adaptation of these models can be made for more complex spacecraft, for example, Jason-1 or ENVISAT.

A paper by Marquis (2000) provides an overview of how the forces acting specifically on GPS Block IIR satellites are dealt with by Lockheed Martin, the spacecraft contractors. Their aims were to develop improved a priori models, in order to determine whether an increase in their accuracy resulted in increased accuracy for GPS users. Their a priori models include the forces due to SRP, TRR of solar panels and parts covered in thermal blankets, emissions from the radiators, antenna thrust, spacecraft surfaces covered in multilayer insulation, shunt energy dissipation (this is the difference

between the amount of energy produced by the solar panels and the amount of energy drawn away by the bus), earth albedo and earth infrared. The details of their actual modelling techniques are scant and no generalised methods are described. The geometry of the GPS Block IIR spacecraft surface was modelled using tessellated triangles, which although still fairly crude, generates a more detailed structure than a box and wing model. To analyse this model, two solar pressure parameters, K1 and K2, were estimated empirically in the orbit determination process using a Kalman filter (Kaplan, E., 1996). K1 represents a solar scale and K2 is a Y-bias acceleration. The quality of the models was judged on the size and stability of the empirical terms. Testing was carried out by the Naval Surface Warfare Centre for one GPS Block IIR satellite; a comparison of the empirical parameters generated using the Rock 42 models developed for GPS Block II and IIA (which included no thermal analysis) showed that the Rock 42 models underestimated the solar scale by 12-13%, whereas the new SRP (including TRR) model for IIR was in error by less than 1%. This result implies that the new SRP method appears to work fairly well for GPS Block IIR, though it is certain that the relative simplicity of the shape of GPS Block IIR enables this, in spite of their simplifications in modelling. The main conclusion of the paper was that the new, more detailed SRP model added improved accuracy to an already accurate system.

The Centre Nationale des Etudes Spatiale (CNES) developed an SRP and TRR surface force model for Jason-1. Details of their method are unavailable in the public literature, but the essence of their technique is as follows (Ferrier, C. et al., 2002): a box and wing spacecraft model is created where the dimensions of the box and the surface optical properties are calculated to yield the same response as the real spacecraft. This means that the complex geometry of the real spacecraft does not need to be dealt with at each epoch in orbit determination, and therefore significantly reduces the computational burden. The assumption inherent in this approach is that the empirically estimated parameters will soak up all the mis-modelled effects, which are inevitable due to the simplification. If the spacecraft deviates substantially from a box and wing model (which it does in the case of Jason-1), then this assumption may not hold, and residual systematic biases can remain as exemplified by Ziebart et al. (2003a). This work will be used as a comparison against the work done in this study and will be discussed in Chapter 7.

Ziebart (2001) developed a detailed SRP model for the Russian positioning system satellites, GLONASS. He states that the pattern of the orbit residuals that resulted from orbit prediction tests were in line with Vigue's prediction of the behaviour of the thermal force. This implied that a substantial part of the residual mis-modelling could be corrected by developing a TRR model for GLONASS.

3.4.2 Spacecraft thermal control

Surface thermal effects include the forces that arise due to heat vented out to space through radiators and heat louvers. The amount of energy expelled depends on internal temperature distributions and heat transfer processes. A large body of work has been carried out on methods for the calculation of temperatures within a spacecraft and how to control them. This has been driven by the necessity to ensure that ideal thermal conditions are maintained so delicate electronics and subsystems operate optimally. Spacecraft are commonly equipped with combinations of heaters, heat louvers, radiators, refrigerators and thermo-electric coolers and make use of different absorbance/emittance coatings and thermal blankets to control internal heat distributions and regulate outgoing heat. Thermal control methods are well documented in many texts and papers (Gilmore, D., 1994; Fortescue, P. et al., 2003). Fortunately engineering data usually includes values for emission from radiators and louvers, and therefore knowledge of the internal heat transfer processes (which would undoubtedly be too complicated to incorporate in orbit models) is not required, and will not be considered further.

3.4.3 Eclipse boundary crossing time determination

Earth-orbiting satellites experience partial or total eclipses when they pass through the regions known as the umbra and penumbra. In the penumbra, the total solar irradiance is partially occluded by the earth, whereas the umbra can be defined as the region on the anti-sun side of the earth which is completely devoid of solar radiation. In reality the earth is flattened, with the polar radius being about 0.3% smaller than the equatorial radius. If the earth's oblateness is taken into account, the boundaries of the shadow regions are altered.

Literature detailing previous approaches to eclipse region modelling is sparse, and the existing material ranges between two extremes. Several techniques have been developed

using a spherical earth model, which allows simple geometric arguments to be developed. These are described in Montenbruck (2000) and Vallado (2001). Some methods (Neta, B. & Vallado, D., 1994) describe a cylindrical shadow model, but this totally ignores the penumbral region where the flux gradually diminishes. These methods are simple to implement from a computation viewpoint, though they result in errors in precise orbit computation.

Vokrouhlicky, D. et al. (IV), (1996) states that it is certainly worthwhile treating the earth as an oblate spheroid as it has been shown that with respect to a spherical earth the main changes occur in the timing of the umbra and penumbra transitions, and in the overall duration of the eclipse periods. Woodburn (2000) showed that such mistiming has important consequences for the precise numerical integration of orbit trajectories.

The main drawback of implementing techniques using existing approaches for eclipse boundary determination with a spheroidal earth is that they are significantly more complex than for a spherical earth. In Vokrouhlicky's paper (1996), he describes a method which involves a complex series of rotations, and in Neta and Vallado (1994) a method involving the solution of quartics is described. The shortcoming of both these methods is that they are costly to implement in operational software due to the intensive nature of the computation required. Until now, there has been no published method which describes a simple and efficient way to accurately calculate eclipse boundary crossing times and, without such a method, the accurate calculation of SRP and TRR during the course of an orbit for an eclipsing satellite is extremely difficult.

3.4.4 Other non-conservative forces

The largest of the non-conservative forces is solar radiation pressure and many techniques have now been developed for the solution of this force, ranging from the fairly crude to the much more precise. Methods for SRP modelling can be found in Milani and Nobili (1987) and those already referred to in Fliegel (1992, 1996). The state of the art in SRP modelling uses a pixel array algorithm (described in Section 5.6) which automatically takes into account the complexity of real spacecraft. A detailed description of this method can be found in Ziebart (2001).

Albedo and infrared emissions from the Earth provide radiation which acts on a spacecraft's exposed surfaces in a fashion similar to that of SRP as described in Chapter 2. This radiative flux coming from the earth is commonly evaluated by dividing the Earth into a grid and taking the vector sum of the grid-to-satellite accelerations. The standard models that have been adopted in most orbit determination codes (Knocke, P., 1988; Borderies, N., & Langaretti, P., 1990) are fairly simplistic and do not account for the large temporal variation due to the changing albedo of the Earth's land masses arising from snow and vegetative covering, and the distribution of clouds. Martin and Rubincam (1993) attempted a detailed calculation of the specular and diffuse albedo re-radiation based on measured global albedo time histories to assess whether this would result in improvement over the Knocke models. Their study indicated that while the time history of the albedo is complex, when integrated over the Lageos orbit, it produces effects which are similar to that obtained with the simpler models. Now probes exist in space from which very high resolution temporal and spatial radiation data sets can be extracted and used to produce more accurate albedo models (Ziebart, M. et al., 2004b). Data from these models are utilised in the validation of the thermal models developed in this thesis and will therefore be described in Chapter 5.

Summary

In this chapter the basis of the thermal surface force and its characterisation was explained. The analytical and empirical approaches that have been used to account for it were described and a review of the published work to date related to this topic was given. Scant work has been done on the process of calculating a detailed analytical thermal force model, and that which has been done is primarily for simply shaped spacecraft, such as spheres or box-and-wing representations of more complicated structures, and often the specific method details have not been described. In earlier work, model simplicity was necessary due to the computational load that accurate models of complex spacecraft introduce. As computer power becomes less of a restriction, there is now no reason why a current state of the art model should not attempt to model accurately a realistic complex spacecraft structure. Chapter 4 describes the methods developed in this thesis which aim to do this.

Part II

Chapter 4 Modelling methods

Chapter outline

This chapter describes the methods developed during the course of this research to deal with the treatment of the thermal forces produced by various parts of the spacecraft, both in steady state and during shadow crossings where temperature changes occur on a very short timescale. Methods for determining accurate eclipse boundary crossing times based on the earth modelled as an oblate spheroid and a model of flux in penumbral regions are described. Methods are also given for the modelling of solar radiation pressure and earth radiation pressure as they impact upon some aspects of the thermal forces models and their testing.

4.1 Introduction

The aim in this chapter is to develop generalised analytical thermal re-radiation force models. The problem consists of:

- defining the flux in the vicinity of the spacecraft
- computing the radiation incident on each surface component as a function of space and time
- calculating the temperature variations over the surface of a spacecraft by analysis of energy transport mechanisms
- calculating the resultant force
- fitting models to these forces for use in orbit computations

Spacecraft with internal subsystems commonly have a central bus and solar panel arrays attached via boom arms to the bus; thus the bus and the panels are assumed to be strongly thermally decoupled. For many spacecraft, the bus is largely wrapped in thermal blankets called multilayer insulation (MLI) (Gilmore, D., 1994) whose function is to thermally stabilise the spacecraft to prevent significant deviations of bus internal

temperatures from the design regime. Methods are developed for the solar panels and parts of the bus covered in MLI. Remaining surfaces are considered individually and a discussion for these parts is given.

The techniques developed in this chapter are applicable to Galileo, Glonass, ENVISAT, TOPEX/Poseidon and Mars Global Surveyor to name only a few. Spacecraft which do not conform to this generic box and wing structure include GRACE, CHAMP (Challenging Minisatellite Payload) and some micro-satellites, and the techniques developed here will require some adaptation for those cases.

During most mission phases, when in full sunlight, Earth pointing satellites change attitude and distance from the sun slowly and smoothly over an orbit[5]. The component surface areas exposed to sunlight hence change slowly, and the flux in the vicinity of the spacecraft varies smoothly as a function of sun-probe distance. The corresponding temperatures change on timescales such that at each instant, can be assumed to be constant (Fortescue, P. et al., 2003). In these regions a steady state temperature regime is assumed. When the spacecraft goes into eclipse, the reduction in incoming flux causes the surface temperatures to change on a much quicker timescale and a transient analysis is required to calculate surface temperatures and resultant forces.

In Section 4.2, a solar panel thermal force model is developed and in Section 4.3, the approach for the treatment of MLI is described. Section 4.4 outlines an approach to dealing with the response of the MLI to earth radiation fluxes. Section 4.5 describes a method which can be used for the calculation of eclipse boundary crossing times, and Section 4.6 details the method for calculating the reduction in solar flux in the penumbral regions.

4.2 Solar panels

For clarity the following nomenclature is defined for symbols appearing in this section:

A area (m^2)

F force (N)

[5] The exceptions to this are during gyro calibration manoeuvres or when corrective thrusts are applied. During these times data from the spacecraft are generally not used.

m mass (kg)

$\bar{n}$ unit vector normal to surface

q heat transfer rate (Wm^{-2})

T temperature (K)

W incident solar radiation (Wm^{-2})

c_{sp} specific heat capacity ($Jkg^{-1}K^{-1}$)

α absorptivity

ε emissivity

k conductivity ($Wm^{-1}K^{-1}$)

θ angle between negative surface normal and incoming photon flux

L thickness of panel (m)

ρ resistivity of panel (Ωm)

Rtotal effective resistance of total panel (Ω)

Subscripts:

b back face of solar panel

f front face of solar panel

Constants:

c speed of light in a vacuum (299792458 ms^{-1})

σ Stephan-Boltzmann constant (5.6699 x 10^{-8} $Wm^{-2}K^{-4}$)

4.2.1 Description of solar panels

Satellite solar panels consist of many thin layers of materials sandwiched together to form a composite structure. They generally have two dominant layers: the solar cells which lie below a quartz coverglass, and a highly conductive aluminium core (Figure 4.1) (Gilmore, D., 1994). As a consequence of the diffuse nature of the thermal emission (Section 3.1), the resulting force acts normal to the panels. The thermal re-radiation force depends on the temperatures of the front and back surfaces of the panel; these temperatures depend upon the amount of radiation incident on and emitted by the panels and the way that heat is transported through the panel layers. An analysis of these energy transport mechanisms requires knowledge of the material properties, panel

dimensions, panel orientation relative to the incoming solar flux and the amount of power drawn from the panels.

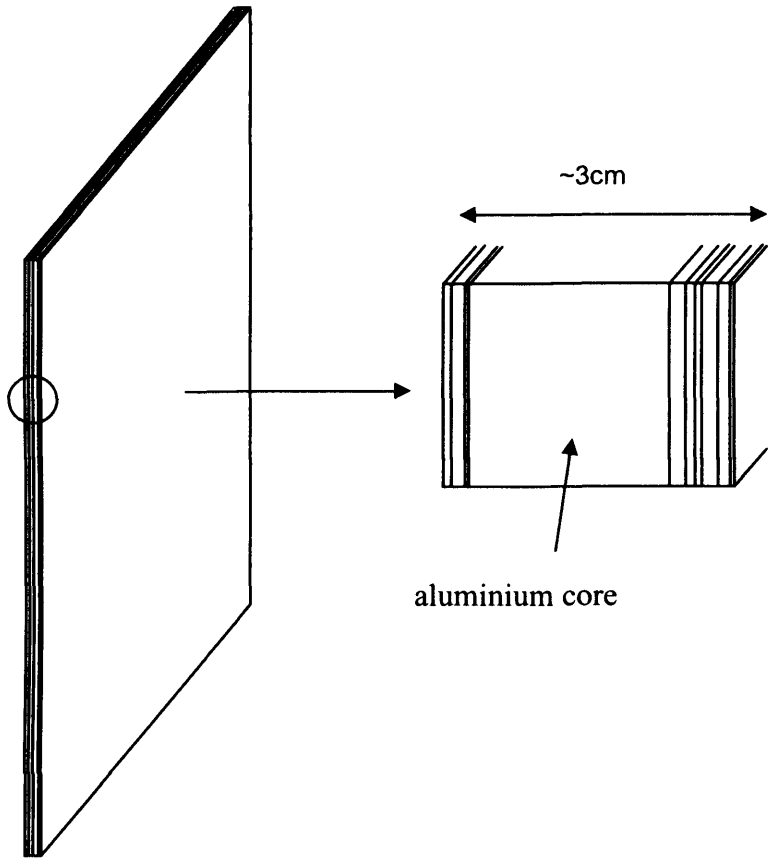

Figure 4.1: Composite structure of solar panel

4.2.2 Steady state solar panel thermal force calculation

In this analysis, a one dimensional, steady state condition is applied. A one dimensional scheme is appropriate since as the area of the panels is much greater than their thickness and the incident radiation and properties are constant over the panel area, heat should be transferred perpendicular to the layers. The principal source of incoming energy is solar radiation and only this is considered here (Earth radiation is discussed in Section 4.72). In this analysis, ERP is ignored. This is reasonable for medium earth orbiting spacecraft (such as GPS spacecraft) where ERP fluxes are ~15Wm^{-2}, though for low earth orbiter's, like Jason-1, this may cause inaccuracies; this is discussed further in Chapter 6. Energy leaves the panels via radiation from the front and back surfaces and power is drawn from the panels to supply energy to other satellite components. Under the steady

state assumption, no overall energy change of the panel occurs and hence an energy balance is considered in order to calculate the surface temperatures. Figure 4.2 depicts the energy inputs and outputs of the panel and Figure 4.3 depicts an energy balance for the back surface of the panel.

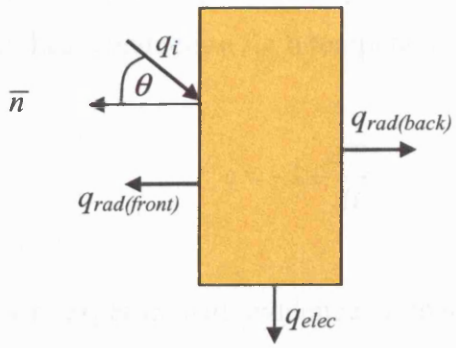

Figure 4.2: Energy inputs and outputs of the solar panel

An energy balance yields:

$$q_{in} = q_{rad(front)} + q_{rad(back)} + q_{(elec)} \tag{4.1}$$

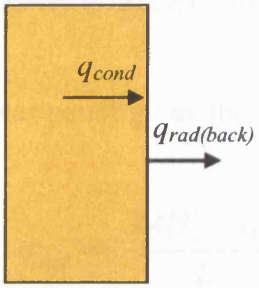

Figure 4.3: Energy inputs and outputs of the back face of solar panel

$$q_{cond} = q_{rad(back)} \tag{4.2}$$

The term q_{in} (W) is the amount of incoming radiation that is absorbed each second. In this model only solar radiation, which is the largest source is considered. This is the product of the solar flux, the absorptivity α, the panel area A and the cosine of the angle of incidence θ, shown in Figure 4.2.

$$q_{in} = \alpha W A \cos\theta \tag{4.3}$$

The terms $q_{rad(front)}$ (W) and $q_{rad(back)}$ (W) refer to the rate of energy radiated out of the front and back surfaces and are given as:

$$q_{rad(front)} = \varepsilon_f \sigma A T_f^{\,4} \tag{4.4}$$

$$q_{rad(back)} = \varepsilon_b \sigma A T_b^4 \tag{4.5}$$

To evaluate the rate of heat conduction through the back face of a panel, consideration of how heat is conducted through a composite wall is required. Fourier's Law (Incropera, F. & Dewitt, D., 2001), given in Equation 4.6, describes the rate at which energy is transferred by heat conduction for a temperature gradient in the x-direction.

$$q = -kA\frac{dT}{dx} \tag{4.6}$$

This law is founded on experimental evidence, rather than a derivation from first principles. It states that the energy transferred per unit time is proportional to the cross-sectional area A and the temperature gradient of the material in question. The minus sign indicates that energy will flow from high to low temperatures. The constant of proportionality is k, the conductivity ($Wm^{-1}K^{-1}$), and it is an inherent property of the material. In this study, the conductivity is assumed to be independent of temperature.

Applying Fourier's law to the solar panel gives the rate of perpendicular heat transfer q_{cond} through the material:

$$q_{cond} = -\frac{kA(T_f - T_b)}{L} \tag{4.7}$$

An analogy can be made between the transfer of heat and the transfer of electrical charge: electrical resistance is associated with the conduction of electricity and similarly thermal resistance relates to the conduction of heat (Incropera, F. & Dewitt, D., 2001). Directly analogous to electrical resistance, thermal resistance is defined as:

$$R = \frac{\rho l}{A} = \frac{l}{kA} \tag{4.8}$$

where the thermal resisitivity ρ is equal to $1/k$. In a composite structure such as a solar panel, each layer of the panel can be treated as a resistor and the total resistance can be calculated by adding the resistances of each layer as if it were a series circuit. If unit area is assumed and each layer has a thickness l_i and conductivity k_i then:

$$R_i = \frac{l_i}{k_i A} \tag{4.9}$$

$$R_{total} = \sum R_i \tag{4.10}$$

where R_i is the resistance of each layer and R_{total} is the total resistance per unit area of the panel. The effective conductivity K_{eff} describes the conductivity of the panel overall, taking into account the conductivities of the individual layers, and is defined as:

$$K_{eff} = \frac{L}{(R_{total})A} \tag{4.11}$$

From Equation 4.7, the rate of heat transfer, q_{cond} (W) through the solar panel can be written as:

$$q_{cond} = -\frac{K_{eff} A(T_f - T_b)}{L} \tag{4.12}$$

Therefore the amount of heat conducted through the back face of the panel is given by:

$$q_{cond} = -\frac{(T_b - T_f)}{R_{total}} \tag{4.13}$$

Expressions have been derived for all the terms in Equations 4.1 and 4.2 and these can be used to determine the temperatures of the front and back faces. Substituting these terms into Equations 4.1 and 4.2 respectively yields:

$$\alpha WA\cos\theta = \varepsilon\sigma A T_f^{\,4} + \varepsilon\sigma A T_b^{\,4} + q_{elec} A \tag{4.14}$$

$$-\frac{(T_b - T_f)}{R_{total}} = \varepsilon\sigma A T_b^{\,4} \tag{4.15}$$

Rearranging Equation 4.15:

$$T_f = T_b + R_{total}\varepsilon\sigma A T_b^{\,4} \tag{4.16}$$

Substituting for T_f in Equation 4.14 and dividing through by A gives:

$$\alpha W \cos\theta = \varepsilon\sigma(T_b + R_{total}\varepsilon\sigma A T_b^4)^4 + \varepsilon\sigma T_b^4 + q_{elec} \tag{4.17}$$

Equation 4.17 is a non-linear equation for the back face temperature of the panel. With knowledge of the solar flux, the attitude of the panels, the material properties of the layers and the amount of power drawn from the panels, this equation can be solved numerically. The Newton-Raphson method is used to obtain a value of T_b which is then substituted into Equation 4.16 to find the value of T_f. The solution of these temperatures enables the evaluation of the force F which was derived in Section 3.2.

$$F = -\frac{2A\sigma(\varepsilon_f T_f^4 - \varepsilon_b T_b^4)}{3c} \tag{4.18}$$

The corresponding acceleration is obtained by division of Equation 4.18 by the mass of the spacecraft.

$$Acceleration = -\frac{2A\sigma(\varepsilon_f T_f^4 - \varepsilon_b T_b^4)}{3mc} \tag{4.19}$$

4.2.2.1 Construction of the force model

For precise orbit computations, it is necessary to calculate this force at frequent intervals along the trajectory. It is not computationally efficient to attempt an iterative solution as described in Section 4.2.2 at each epoch. For this reason, a relationship is required which will provide the thermal forces as a function of some known quantity whilst in orbit. This quantity is the flux incident on the panel, and can be calculated at each epoch using knowledge of the pointing direction of the panels and distance from the sun. The force is evaluated over a range of possible fluxes, and a polynomial function (a quadratic is generally sufficient and yields RMS residuals of <1%) is fitted to this data by least squares yielding a model of the force as a function of flux. This function can then be evaluated at the required epoch in the orbit modelling software. Figure 4.4 shows an example of force as a function of flux.

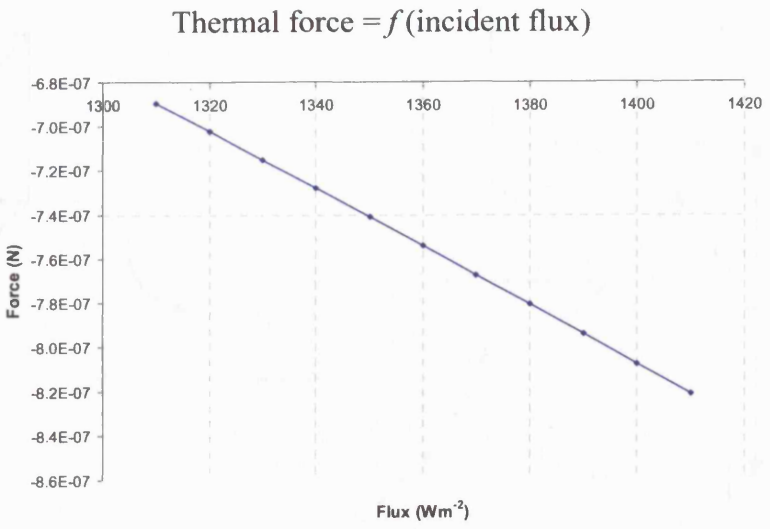

Figure 4.4: Graph of force as a function of flux

In Figure 4.4, the flux limits are driven by the maximum and minimum flux in the vicinity of the spacecraft from perihelion to aphelion.

4.2.3 Transient modelling

When a satellite enters shadow regions, changes in temperature occur on a timescale too quick to allow the steady state assumption to hold true. Changes in surface temperature can only be evaluated once the energy transport mechanisms that supply or remove energy from the surface are calculated. This requires knowledge of the initial temperature distribution within the panel, the material properties of all the layers, specifically their conductivities, densities, specific heat capacities and dimensions.

Time-varying temperatures can be acquired through the solution of the heat equation. The heat equation is a partial differential equation which describes the temperature field in a given region over time. In this section, the heat equation is derived by the application of the conservation of energy principle to a differential control volume ($\delta x \delta y \delta z$) and the energy processes relevant to it, as represented in Figure 4.5.

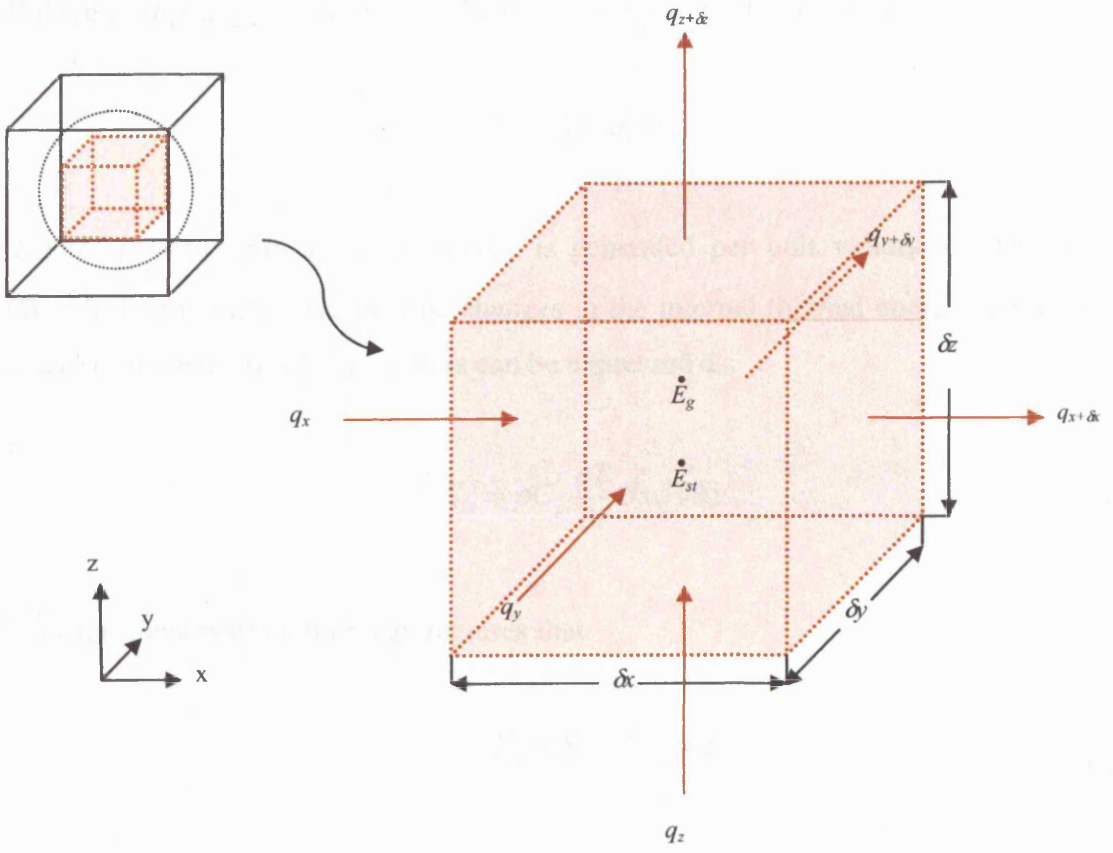

Figure 4.5: Energy transfer processes in a finite control volume.

If the temperature distribution is known at some point in time, Fourier's law can be used to calculate the rate of heat transfer between two points to obtain the temperatures at subsequent epochs. Where temperature gradients exist, heat conduction will occur across each of the control surfaces. The conduction heat rates perpendicular to each of the control surfaces at the x, y and z coordinate locations are indicated by the terms q_x, q_y and q_z. The conduction heat rates at the opposite surfaces can then be expressed as a Taylor series expansion where, neglecting higher order terms,

$$q_{x+\delta x} = q_x + \frac{\partial q_x}{\partial x}\delta x$$

$$q_{y+\delta y} = q_y + \frac{\partial q_y}{\partial y}\delta y \qquad (4.20)$$

$$q_{z+\delta z} = q_z + \frac{\partial q_z}{\partial z}\delta z$$

If there is an energy source within the medium, it can be described as:

$$\dot{E}_g = \dot{q}\delta x\delta y\delta z \tag{4.21}$$

Where $\dot{q}$ is the rate at which energy is generated per unit volume of the medium (Wm^{-3}). In addition, there may be changes in the internal thermal energy stored by the material in the control volume. This can be expressed as:

$$\dot{E}_{st} = \rho C_p \frac{\partial T}{\partial t}\delta x\delta y\delta z \tag{4.22}$$

Now the conservation of energy requires that

$$\dot{E}_{in} + \dot{E}_g - \dot{E}_{out} = \dot{E}_{st} \tag{4.23}$$

$\dot{E}_{in}$ and $\dot{E}_{out}$ represent conduction inflow and outflow, and Equation 4.23 can be rewritten as:

$$q_x + q_y + q_z + \dot{q}\delta x\delta y\delta z - q_{x+\partial x} - q_{y+\partial y} - q_{z+\partial z} = \rho C_p \frac{\partial T}{\partial t}\delta x\delta y\delta z \tag{4.24}$$

Substituting in for Equations 4.20, it follows that:

$$-\frac{\partial q_x}{\partial x}\delta x - \frac{\partial q_y}{\partial y}\delta y - \frac{\partial q_z}{\partial z}\delta z + \dot{q}\delta x\delta y\delta z = \rho C_p \frac{\partial T}{\partial t}\delta x\delta y\delta z \tag{4.25}$$

The heat conduction rates can be evaluated from Fourier's law:

$$\begin{aligned} q_x &= -k\delta y\delta z\frac{\partial T}{\partial x} \\ q_y &= -k\delta x\delta z\frac{\partial T}{\partial y} \\ q_z &= -k\delta x\delta y\frac{\partial T}{\partial z} \end{aligned} \tag{4.26}$$

Substituting Equations 4.26 into Equation 4.24 and dividing out by the dimensions of the control volume, we obtain:

$$\frac{\partial}{\partial x}\left(k\frac{\partial T}{\partial x}\right)+\frac{\partial}{\partial y}\left(k\frac{\partial T}{\partial y}\right)+\frac{\partial}{\partial z}\left(k\frac{\partial T}{\partial z}\right)+\dot{q}=\rho C_p\frac{\partial T}{\partial t} \tag{4.27}$$

This is the heat equation, and can be solved for the temperature as a function of position within the material and time.

When in total darkness, it is assumed that no power is drawn from the panels, so the $\dot{q}$ term can be set to zero and assuming one-dimensional heat flow, the heat equation in Equation 4.27 reduces to:

$$\frac{\partial}{\partial x}\left(K\frac{\partial T}{\partial x}\right)=\rho C_p\frac{\partial T}{\partial t} \tag{4.28}$$

where T is the temperature distribution in the panel at location x and at time t.

For the temperature to be evaluated, the differential equation needs to be solved with appropriate boundary and initial conditions. A technique based on the finite volume method to calculate how temperatures change in a composite wall (Price, B. & Smith, T. , 1994) was applied to the solar panels. This method splits the panels into small control volumes and performs energy balance calculations on each of them based on heat transfer to neighbouring control volumes and heat exchange processes occurring at the panel surfaces. Figure 4.6 shows a panel which is separated into discrete elements of thickness δx_i and δi is the inter-node distance, each element containing a node. For each node, an equation is written at the initial time-step for which the temperatures of each node are known. This equation relates heat flow in and out of the node based on neighbouring nodes and boundary conditions to the temperature change that will result due to this heat flow. These sets of equations are solved simultaneously at each time-step to yield temperatures at the next time-step. For a thorough description of this method, the reader is referred to Price, B. & Smith, T., 1994.

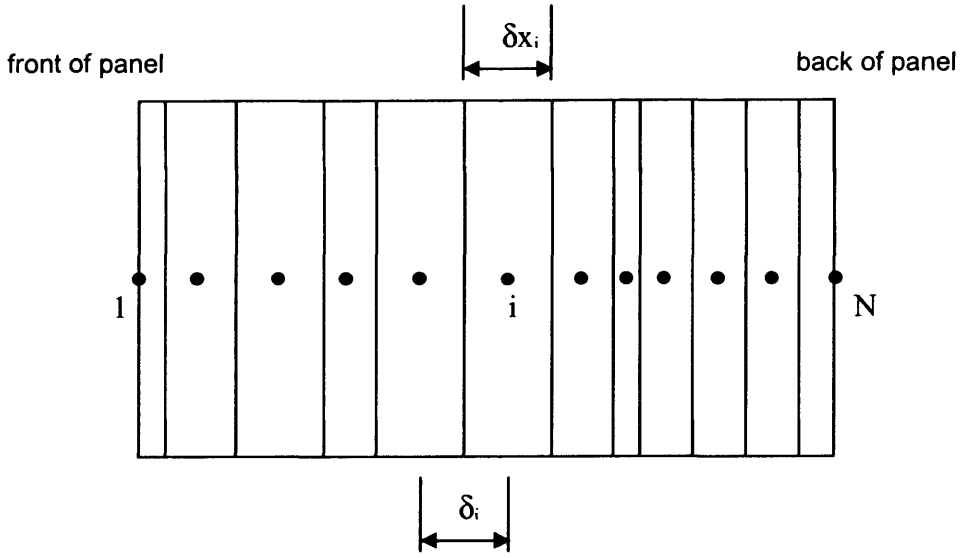

Figure 4.6: Composite panel divided into nodal elements

This method was applied to GPS and Jason-1 solar panels in a hypothetical eclipse situation. The spacecraft was assumed to go from full phase directly into the umbra. The gradual reduction of flux in the penumbra was not included at this stage. Figure 4.7 show the temperature change with time for the front and back panels when the GPS Block IIR spacecraft enters and exits the eclipse; Figure 4.8 shows the corresponding accelerations for a GPS solar panel.

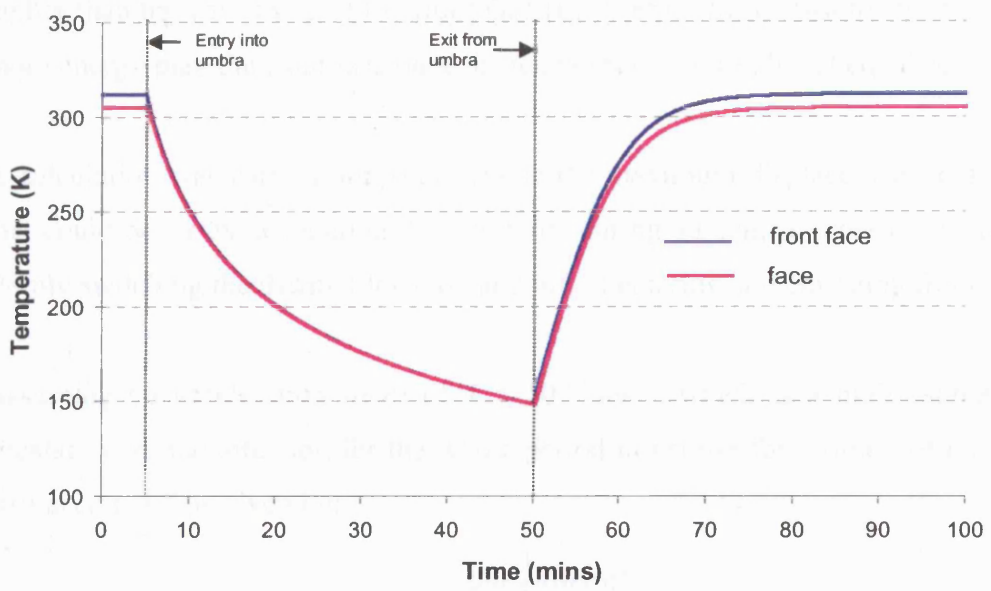

Figure 4.7: Front and back panel face temperatures for a GPS Block IIR spacecraft

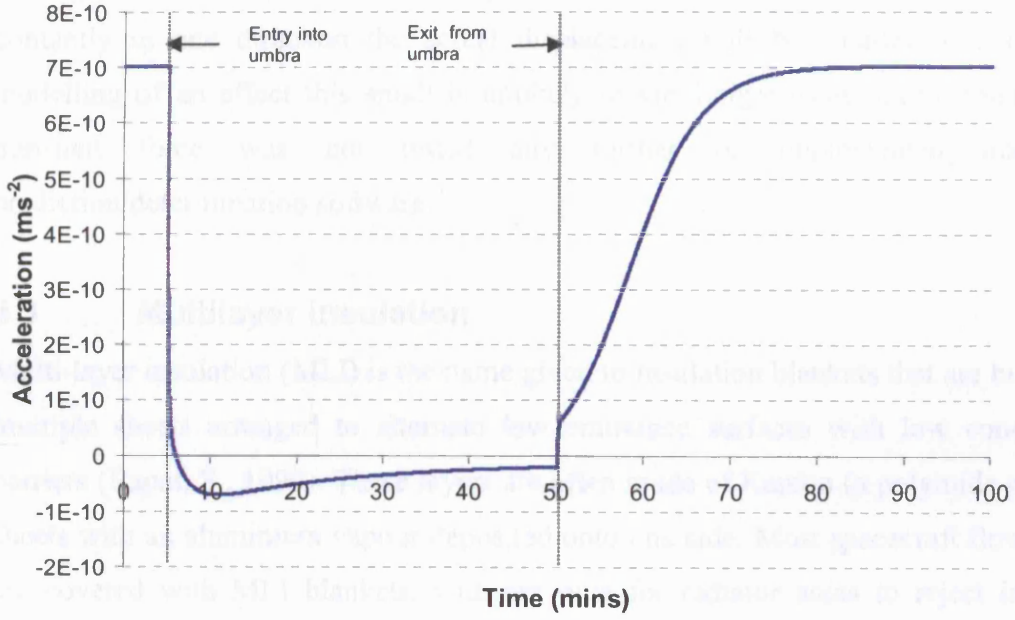

Figure 4.8: Acceleration due to thermal panels for a GPS Block IIR spacecraft

Figure 4.7 demonstrates the fact that the temperatures drop very quickly as soon as the incoming radiation is "switched off". More importantly, the conduction of heat from hot regions to cold regions causes the difference between the front and the back surfaces temperatures to diminish. Therefore, the resultant force, which is the difference between the forces due to the front and the back surfaces, declines extremely rapidly. The resultant force changes direction because the emissivity of the back face (ε_b=0.89) is

higher than the emissivity of the front face (ε_b =0.86). This causes the back face to emit more energy than the front face once the temperatures have almost equalised.

A calculation was carried out to determine the maximum displacement to a spacecraft that could occur by accounting for this force during an eclipse crossing, as opposed to simply switching the thermal force on and off on entering and emerging from eclipse.

Assuming an acceleration (*acc*) of 4 x 10^{-10} ms^{-2} (which is a high estimate) acting constantly in one direction for the whole period in eclipse for a time *t* of one hour, the displacement *S*, is given by:

$$S = \frac{1}{2}(acc)t^2$$

This gives a maximum possible displacement of 3mm. As this force will not act contantly in one direction the actual displacement will be smaller than this. The modelling of an effect this small is unlikely to yield significant improvements. This transient force was not tested any further or implemented into orbit prediction/determination software.

4.3 Multilayer insulation

Multi-layer insulation (MLI) is the name given to insulation blankets that are built up of multiple sheets arranged to alternate low emittance surfaces with low conductance barriers (Bapat, S., 1990). These layers are often made of Kapton (a polymide polymer) sheets with an aluminium vapour deposited onto one side. Most spacecraft flown today are covered with MLI blankets, with cut outs for radiator areas to reject internally generated waste heat (Gilmore, D., 1994) and necessary instrument surfaces. Heat transfer through multilayer insulation is a combination of radiation, solid conduction, and under atmosphere conditions, gaseous conduction.

The solid conduction heat transfer through the blanket is minimised by rumpling of the inner layers, so the aluminised sheets touch at discrete points rather than across the whole surface. Radiation heat transfer is minimised by interposing as many enclosing layers with reflective surfaces (metalised sheets) as is practical. In order to evacuate the air trapped between blanket layers before launch, vent paths have to be provided. This is

often done by small perforations in each blanket layer, while ensuring that perforations between one layer and the next are not aligned in order to minimise incoming radiation entering the spacecraft.

Because the heat transfer mechanisms described above operate simultaneously and interact with each other, the thermal conductivity of MLI is not strictly definable analytically in terms of variables such as temperature, density, or physical properties of the component materials. It is therefore useful to refer to either an apparent thermal conductivity or an effective emittance. These values are usually derived experimentally. When blankets are configured for spacecraft application, experience has shown that effective emissivities are usually between 0.015 to 0.030 (Gilmore, D., 1994).

4.3.1 Properties of MLI

The behaviour of MLI blankets and the assumptions used in this study are as follows:

- Heat transfer parallel to the layers of MLI is ignored. This is valid because MLI is so thin (between 7-25 μm) that effectively no heat is conducted along the individual layers. MLI coverage often consists of discrete pieces that are joined together; this also reduces heat transfer in this direction (pers comms, Cavan, N., Rutherford Appleton Laboratories (RAL), Oct 2002).
- The temperature of the spacecraft beneath the layers of MLI is assumed to be between 273K and 323K. Payload instruments are designed to work at room temperature (Galvin, D., 1999) and therefore spacecraft thermal systems aim to maintain temperatures close to this. It is therefore reasonable to assume T_{sc} to have a value of 298K. The calculation is not highly sensitive to this parameter; an error analysis using temperatures 25 degrees higher and lower than this showed the force to be different by less than 1% (shown in Section 7.1.1.2).
- The MLI surface is assumed to emit radiation as a plane Lambert diffuser (crinkliness is ignored).
- Steady state is assumed in full phase.
- When the satellite enters eclipse, its temperatures are assumed to drop to zero instantly (pers comms, Cavan, N., (RAL), Oct 2002). This is reasonable given that the MLI is not designed to be a good heat store.

- An effective emissivity of 0.02 was used in this study. This was determined experimentally for a typical sheet of MLI (pers comms, Cavan, N., (RAL), Oct 2002).

4.3.2 Computation of flux on body

To evaluate the amount of solar energy each part of the spacecraft receives requires an accurate description of the satellite and knowledge of its attitude, so that the sun-facing profile of the satellite can be calculated. A pixel array method (Ziebart, M., 2004a) is used to calculate how much radiation is incident upon the parts of the satellite that are covered in MLI.

This method is a precise and efficient technique for calculating the flux incident on each spacecraft component for a given attitude and sun position. Software is used to simulate the photon flux with a pixel array which is projected towards a computer model of the spacecraft, and ray tracing techniques are used to determine which parts of the satellite are illuminated. The pixel array is then rotated around the spacecraft and the process is repeated at discrete steps. The pixel array is rotated in all orientations necessary to account for the range of possible profiles of the satellite that are presented to the sun.

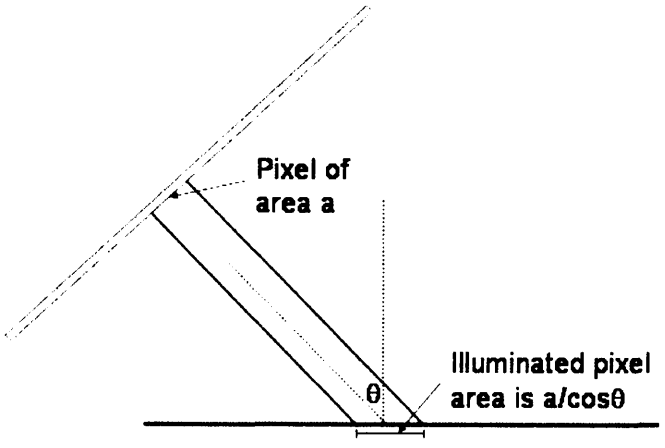

Figure 4.9: Illumination of MLI surface with pixel array

This software was originally created for solar radiation pressure (SRP) modelling, and has been adapted for use in thermal force modelling. The pixel array method and SRP modelling methods are described in Section 4.7.1 later in this chapter.

Once the pixel array software has determined whether a particular surface is irradiated, a test is performed to see whether that part is covered in MLI. If so, a calculation is carried out to determine the force due to the MLI. This calculation is described in Section 4.3.3.

4.3.3 Calculation of force due to MLI

As described in Section 3.1, if the emitting surface is planar and treated like a Lambertian diffuser, the force normal to the emitting surface is given by:

$$\underline{F} = -\frac{2\sigma}{3c} A\varepsilon T^4 \underline{n} \tag{4.29}$$

To obtain solutions for the temperature of the MLI surface, the following energy transport mechanisms are considered.

(1) Solar photons impact upon the MLI.

(2) Energy is both absorbed and reflected, depending on the absorptivity of the MLI.

(3) Of the energy absorbed, some is re-emitted and some is transferred through to the spacecraft. The latter amount is dictated by the value of the effective emissivity.

If a is the area of one pixel, and θ is the angle of incidence of the radiation flux W (see Figure 4.9), the solar radiation absorbed by the surface illuminated by one pixel is $\alpha W a$. The area of the MLI that is illuminated is given by $a/\cos\theta$. The energy radiated out to space is given by:

$$\frac{a}{\cos\theta}\varepsilon_{MLI}\sigma {T_{MLI}}^4 \tag{4.30}$$

A cut off angle of 89.5° was included to prevent Equation 4.30 tending to infinity. The energy conducted through to the spacecraft is given by:

$$\frac{a\varepsilon_{eff}\sigma\left({T_{MLI}}^4 - {T_{sc}}^4\right)}{\cos\theta} \tag{4.31}$$

These terms are substituted into an energy balance to give:

$$\alpha aW = \frac{\varepsilon_{MLI} a\sigma {T_{MLI}}^4}{\cos\theta} + \frac{\varepsilon_{eff}\sigma a({T_{MLI}}^4 - {T_{sc}}^4)}{\cos\theta} \tag{4.32}$$

By dividing through by a and multiplying by $\cos\theta$, Equation 4.32 becomes:

$$\alpha\cos\theta W = \varepsilon_{MLI}\sigma {T_{MLI}}^4 + \varepsilon_{eff}\sigma({T_{MLI}}^4 - {T_{sc}}^4) \tag{4.33}$$

where T_{MLI} is temperature of MLI, T_{sc} is temperature of spacecraft and ε_{eff} is the effective emissivity between the MLI and the spacecraft. Re-arranging Equation 4.33 gives the temperature of the surface illuminated by each pixel:

$${T_{MLI}}^4 = \frac{\alpha W\cos\theta + \varepsilon_{eff}\sigma {T_{sc}}^4}{\sigma(\varepsilon_{MLI} + \varepsilon_{eff})} \tag{4.34}$$

Substituting in the value of 298K for T_{sc}, Equation 4.34 can be calculated to yield the temperature which when substituted into Equation 4.35 below, yields the force due to the illuminated area.

$$\underline{f} = -\frac{2\sigma\varepsilon_{MLI}{T_{MLI}}^4}{3c}\underline{\hat{n}} \tag{4.35}$$

4.4 Thermal Response of MLI due to earth radiation flux

It is only recently that consideration has been given to the analytical modelling of forces of the order of magnitude of TRR and earth radiation pressure (ERP) ($\sim 10^{-7}$ N). As more and more of the error is removed by improved force models, effects such as thermal re-radiation due to radiation from the earth, which are at least an order of magnitude smaller, begin to attract attention.

In this study, a "first pass" treatment of the problem is made; these effects are considered for GNSS altitude satellites only and the assumptions made cannot necessarily be applied to LEO satellites.

The analysis of the thermal force due to Earth radiation involves a combination of the thermal model for the satellite and an Earth radiation model of the earth. All radiation from the earth that reaches the satellite is assumed to approach along the BFS +Z-axis (the earth-spacecraft vector). In reality this approximation is fairly reasonable (especially for GNSS altitude satellites), since most of the radiation comes from the sub-satellite point as a result of the Lambertian nature of the earth radiation model used. Figure 4.10 shows radiation coming from points A and B, that are some distance away on either side of the sub-satellite point. In general, components of this radiation that act perpendicular to the BFS Z-axis would cancel, and most of the displacement would be along the BFS Z-axis.

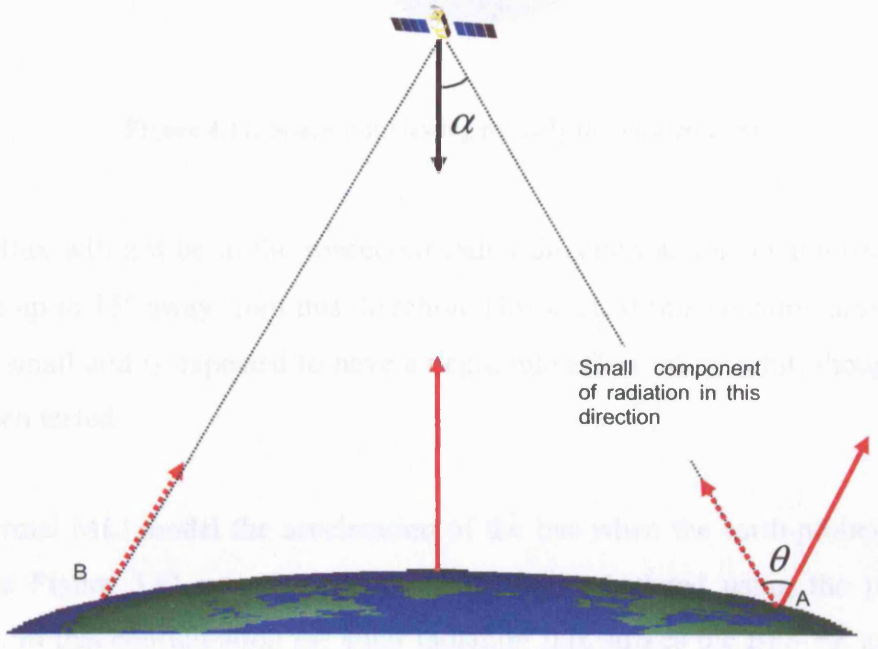

Figure 4.10: Radiation from earth impinging on the satellite

For a GPS spacecraft, the maximum value for α is ~15°. The situation where this will create the largest error is when half the earth is in shadow, and the other half is in sunlight as shown in Figure 4.11 below.

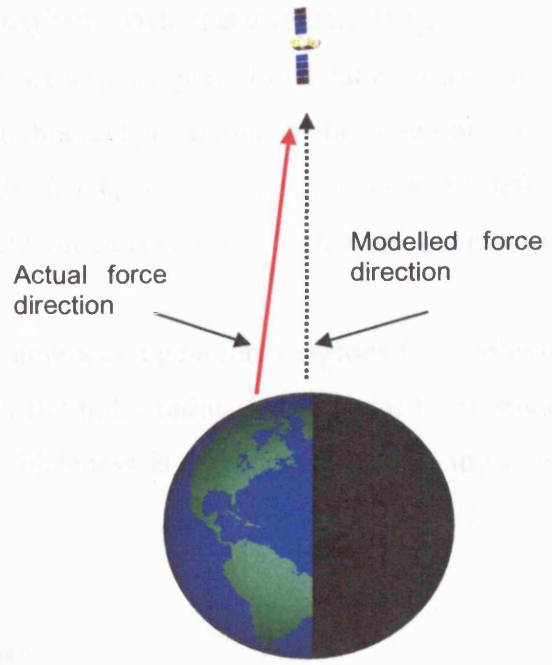

Figure 4.11: Spacecraft viewing partially illuminated Earth

Here the flux will not be in the spacecraft radial direction and as mentioned, could in theory, be up to 15° away from this direction. However, if this situation arose, the flux would be small and is expected to have a negligible effect on an orbit, though this has not yet been tested.

In the thermal MLI model the acceleration of the bus when the earth-probe-sun (EPS) angle (see Figure 3.6) was zero (EPS = 0°) was calculated using the pixel array technique. In this configuration the solar radiation flux strikes the BFS +Z axis face of the spacecraft. An estimate of the thermal response of the MLI due to ERP, $acc_{thermal\_ERP}$, was made by adapting this value by scaling for the ERP flux magnitudes at GNSS altitudes, as shown in Equation 4.3.6:

$$acc_{thermal\_ERP} = \frac{W_{ERP}}{W_S} acc_{MLI} \tag{4.36}$$

where W_{ERP} is the flux due to ERP, W_s is the solar flux, and acc_{MLI}, is the acceleration of the MLI due to solar flux at an EPS angle of zero.

4.5 Eclipse region boundary modelling

Earth-orbiting satellites experience partial or total eclipses when they pass through the regions known as the umbra and penumbra. In the penumbra, the total solar irradiance is partially occluded by the Earth, whereas the umbra can be defined as the region on the anti-sun side of the Earth which is completely devoid of solar radiation.

Figure 4.12 shows the umbra and penumbra regions for a spherical Earth. In reality the Earth is flattened, with the polar radius being about 0.3% smaller than the equatorial radius. If the Earth's oblateness is taken into account, the boundaries of the shadow regions are altered.

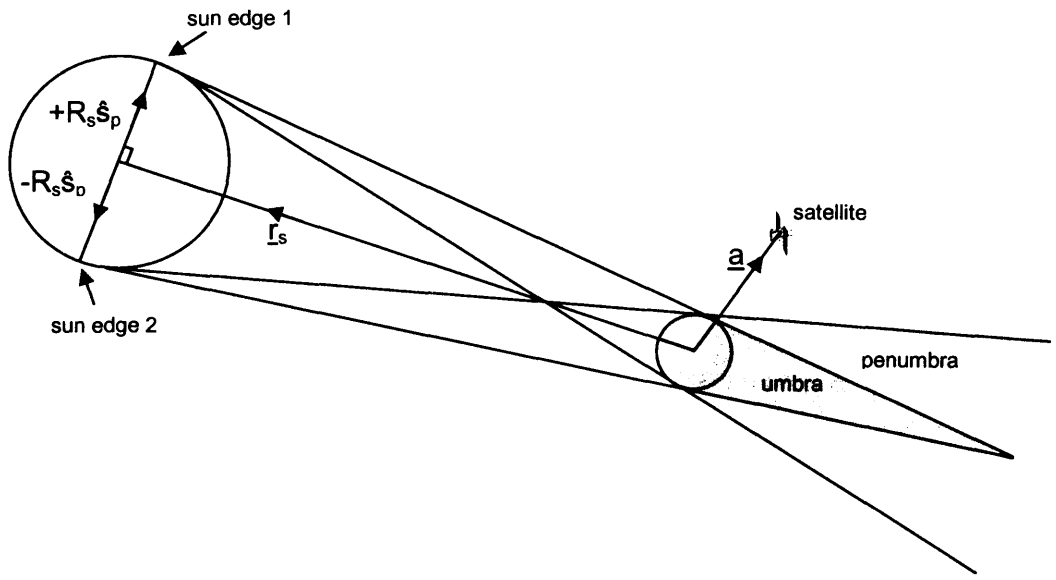

Figure 4.12: Lines forming penumbra and umbra boundaries

In order to model accurately the forces caused by solar radiation it is necessary to know when the satellite enters or exits a shadow region, as the amount of solar radiation incident on the spacecraft changes dramatically (Woodburn, J., 2000). Forces so affected include SRP and TRR.

A review of the publicly available literature on this subject indicates that current methods are either accurate or efficient, but not both (see Section 3.4.3). As part of the force modelling work undertaken in this thesis, a new treatment of the problem has been developed which yields direct solutions for the eclipse state (whether the spacecraft is in

full sunlight, penumbra or umbra) whilst still accounting for the earth's polar flattening. The aim is to develop a method which combines accuracy with efficiency, and is therefore usable for orbit determination purposes, where a solution for the eclipse state will be required very frequently. The mathematical formalism of this method is described in Section 4.5.1 and in Adhya, S. et al., (2004). In the development of this method, tests to assess its validity are included in this section.

4.5.1 Determination of satellite eclipse state

This method is based upon tests that determine whether or not lines from the sun edges to the spacecraft intersect the Earth. If an intersection occurs, and the distance from the sun to this intersection point is less than the sun-spacecraft distance, then the satellite is either in the penumbra or the umbra.

An instantaneous plane is defined by the geocentre, the Earth-sun vector $\underline{r}_s$ and the Earth-spacecraft vector $\underline{a}$ (see Figure 4.12). In this two-dimensional space the sun is modelled as a circle. In the plane, rays of light starting at the sun edges and making tangents with the Earth define the full phase/penumbra and penumbra/umbra boundaries, as shown in Figure 4.12.

The actual calculations of the intersection points are carried out using three-dimensional geometry, with the surface of the Earth being mathematically approximated by the equation of a spheroid:

$$\frac{x^2+y^2}{p^2}+\frac{z^2}{q^2}=1 \tag{4.37}$$

where x, y, z are the ECI coordinates of a point in space on the surface of the spheroid, p is the equatorial radius and q is the polar radius.

The line passing through the spacecraft and sun-edge 1 is henceforth referred to as Line 1. Any point (x, y, z) on Line 1 obeys the equation:

$$\begin{pmatrix} x \\ y \\ z \end{pmatrix} = \begin{pmatrix} a_1 \\ a_2 \\ a_3 \end{pmatrix} + \lambda \begin{pmatrix} b_1 \\ b_2 \\ b_2 \end{pmatrix} \tag{4.38}$$

where (a_1, a_2, a_3) are the x, y, z components of the position vector of the spacecraft $\underline{a}$, and (b_1, b_2, b_3) are the x, y, z components of the vector from sun-edge 1 to the spacecraft $\underline{b}$. Rearranging and equating the formulae for Equation 4.38 yields the following relationship, which is another definition for Line 1:

$$\frac{x-a_1}{b_1}=\frac{y-a_2}{b_2}=\frac{z-a_3}{b_3} \tag{4.39}$$

Vectors $\underline{a}$ and $\underline{b}$ can be obtained at a specific epoch from precise ephemeredes or numerical integration, and hence Line 1 is defined. Line 2 is defined similarly with a different value of vector $\underline{b}$.

To calculate the vector the coordinates of the sun-edges are required. The unit vector orthogonal to the Earth-sun vector is used to find these sun-edges in an ECI coordinate frame (see Figure 4.12). The vectors $\underline{r}_{s1}$ and $\underline{r}_{s2}$ can be defined as the lines from the geocentre to sun-edge 1 and sun-edge 2 respectively. Hence the vector $\underline{b}$ is calculated from:

$\underline{b} = \underline{r}_{sc}\text{-}\underline{r}_{s1}$ for Line 1 and (4.40)

$\underline{b} = \underline{r}_{sc}\text{-}\underline{r}_{s2}$ for Line 2.

To determine $\hat{S}_p$, the unit vector that lies in the plane and is perpendicular to $\underline{r}_s$ (see Figure 4.12), the cross product between $\underline{r}_s$ and $\underline{a}$ is taken to give a vector ($\underline{r}_i$) normal to the plane.

$$\underline{r}_i = \underline{r}_s \times \underline{a} \tag{4.41}$$

Taking the cross product of $\underline{r}_i$ with $\underline{r}_s$ gives the vector that lies in the plane and is perpendicular to $\underline{r}_s$, which is $\hat{S}_p$.

$$\underline{S}_p = \underline{r}_s \times \underline{r}_i \tag{4.42}$$

Normalizing this vector gives $\hat{S}_p$.

The two sun edge points are given by:

$$\underline{r}_{s1} = \underline{r}_s + (R_s.\underline{\hat{S}}_p) \tag{4.43}$$

$$\underline{r}_{s2} = \underline{r}_s - (R_s . \hat{\underline{S}}_p) \tag{4.44}$$

where R_s is the sun radius.

From Equation 4.39, it is possible to rewrite y and z as a function of x and the coefficients of vectors $\underline{a}$ and $\underline{b}$.

$$y = \frac{b_2}{b_1}(x - a_1) + a_2 \tag{4.45}$$

$$z = \frac{b_3}{b_1}(x - a_1) + a_3 \tag{4.46}$$

Now y and z can be substituted into Equation 4.37 to yield a quadratic in x:

$$\frac{x^2 + \left[\frac{b_2}{b_1}(x - a_1) + a_2\right]^2}{p^2} + \frac{\left[\frac{b_3}{b_1}(x - a_1) + a_3\right]^2}{q^2} = 1 \tag{4.47}$$

$$q^2 x^2 + q^2\left[\frac{b_2}{b_1}(x - a_1) + a_2\right]^2 + p^2\left[\frac{b_3}{b_1}(x - a_1) + a_3\right]^2 = p^2 q^2 \tag{4.48}$$

$$Ax^2 + Bx + C = 0$$

In this quadratic:

$$\begin{aligned}
A &= b_1^2 q^2 + q^2 b_2^2 + p^2 b_3^2 \\
B &= -2b_2^2 q^2 a_1 + 2b_1 b_2 q^2 a_2 - 2p^2 b_3^2 a_1 + 2p^2 b_1 b_3 a_3 \\
C &= q^2\left[b_1^2 a_2^2 + b_2^2 a_1^2 - 2b_2 b_1 a_1 a_2\right] + p^2\left[b_1^2 a_3^2 + b_3^2 a_1^2 - 2b_3 b_1 a_1 a_3\right] - b_1^2 p^2 q^2 = 0
\end{aligned} \tag{4.49}$$

The real solutions to this quadratic equation give the x-coordinates of the points of intersection of the spheroid and the sun-edge to spacecraft line.

For a real solution to exist:

$$B^2 - 4AC \geq 0 \tag{4.50}$$

If Equation 4.50 is satisfied, an intersection takes place. A negative value has no physical meaning, but shows that no intersection occurs. If there is no intersection, then the satellite is in full phase. Lines from both sun edges to an instantaneous satellite position are tested in this manner. Once the value of x is obtained, it can be substituted into Equation 4.39 to solve for the y and z coordinates of the intersection point; equivalent equations can be generated to yield quadratics in y and z. Full coordinates of the intersection point are required in order to calculate its distance from the sun. If this distance is larger than the distance between the sun and the spacecraft, then the satellite is automatically assigned a state of full phase. In all other cases, the following conditions are regarded (see Figure 4.1.3):

- If both lines have real solutions, then the spacecraft is in the umbra.
- If only one of the lines has real solutions the spacecraft is in the penumbra.
- If there are no real solutions then the spacecraft is in full phase.

The algorithm written to carry out this function takes a UTC time-tag and the position vector of the satellite as inputs. The corresponding sun positions are retrieved for each epoch from an ephemeris file (JPL DE405), and the test for intersection points is carried out. A specified integer value is returned depending upon the result of the computation; the program calling the function uses this integer value to determine if a change of state has occurred.

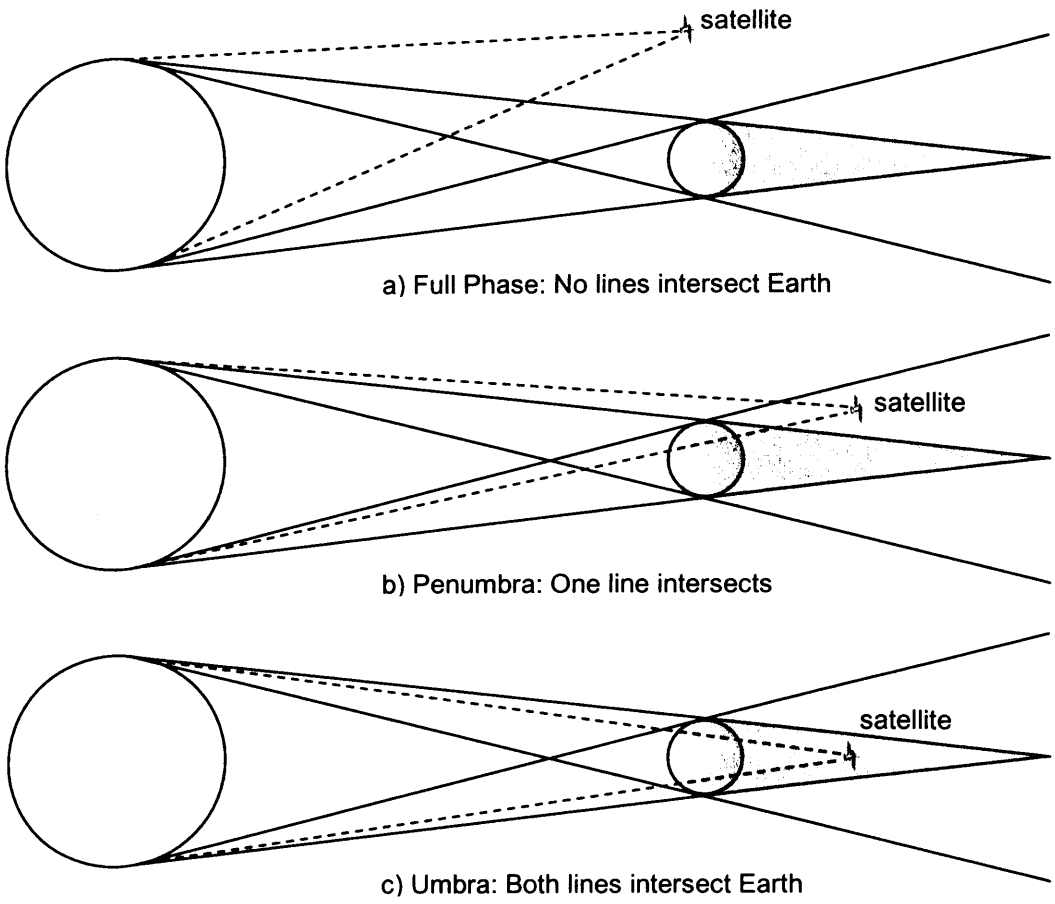

Figure 4.13: Diagram of a satellite in full phase and a satellite in eclipse

4.5.2 Results of eclipse state determination testing

The method above describes a way of determining whether the satellite is in full phase, penumbra or umbra at a particular epoch. This algorithm can be used with positions interpolated from precise ephemeredes, or from an integrated orbit position for prediction purposes. In order to precisely determine crossing times, iteration between the satellite's position and its state will be required. The iteration process is efficient as the algorithm shares much of the geometric simplicity of its spherical Earth counterparts, thus ensuring its implementation is straightforward. The algorithm could be easily incorporated into both fixed-step and adaptive-step size orbit integrators.

Testing of the method was conducted using precise ENVISAT orbit and photometric data which was made available to us by the satellite laser ranging (SLR) facility at Herstmonceux. In this instance, photometry is simply the observation and counting of

solar photons reflected from the spacecraft, which can be sorted from laser pulses during simultaneous SLR observations on the basis of amplitude and duration by a median filter (Otsubo, T. et al., 2001). Obviously, as the satellite enters eclipse, there will be less sunlight incident upon it, resulting in fewer photon counts; though this will also depend to a small degree upon the viewing geometry from the SLR station. The photometry data shown in Figure 4.14 for ENVISAT (a LEO satellite), and Figure 4.15 for Glonass (a MEO satellite) are quite typical for the satellites tested.[6] A decision was made to use only the ENVISAT photometry to test the algorithm because, as can be seen from the figures, the Glonass eclipse transition occurs over a much longer time period. It is also expected that atmospheric refraction will have a greater impact on the higher altitude satellites, and therefore the algorithm is likely to have more errors associated with it for higher altitude satellites. However, the Herstmonceux SLR team is currently tracking Russian Etalon satellites, which are covered in corner cube reflectors and orbit with an altitude of approximately 19,000 km, in an attempt to try to assess the effect of atmospheric refraction on eclipse transition times. Orbital data for ENVISAT is given in Table 4.1.

Semi-major axis	7159 km
Inclination	98.5°
Eccentricity	0.001165
Argument of perigee	90.0° ± 3°
Mean local solar time at descending node	10am

Table 4.1: Approximate orbital elements for ENVISAT

To estimate the time of onset of shadow transition, the team at the SLR facility fitted a low order polynomial to a short period of pre-event photometric data. This function is extrapolated and residuals from the photometry data are computed. When the modulus of the residuals become larger than 3 x RMS of the post-fit residuals, the event is assumed to be underway. The precision of this process is estimated to be about 1 second

[6] Photometry data was reproduced by kind permission of the NERC Space Geodesy Facility at Herstmonceux, E. Sussex.

of time, and the epochs of the photometry data are at a much higher resolution than this (pers comms, Appleby, G., March 2002).

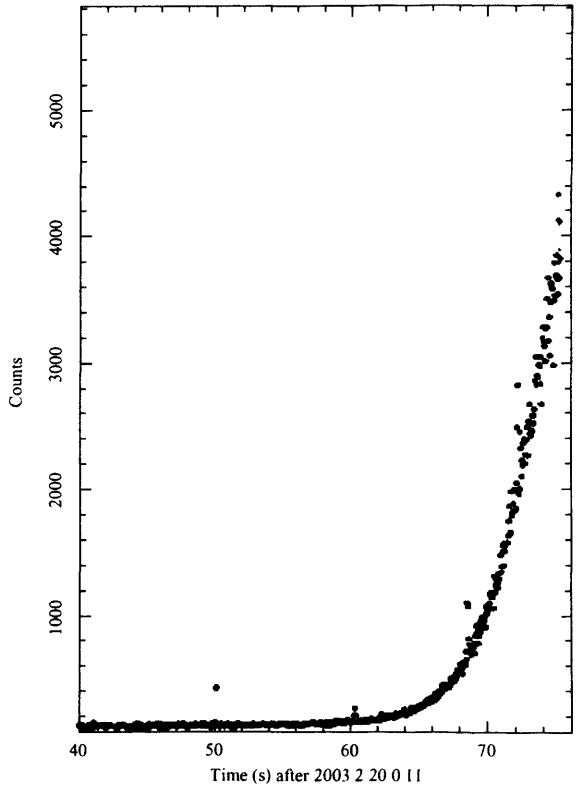

Figure 4.14: ENVISAT photometry plot - emergence from eclipse

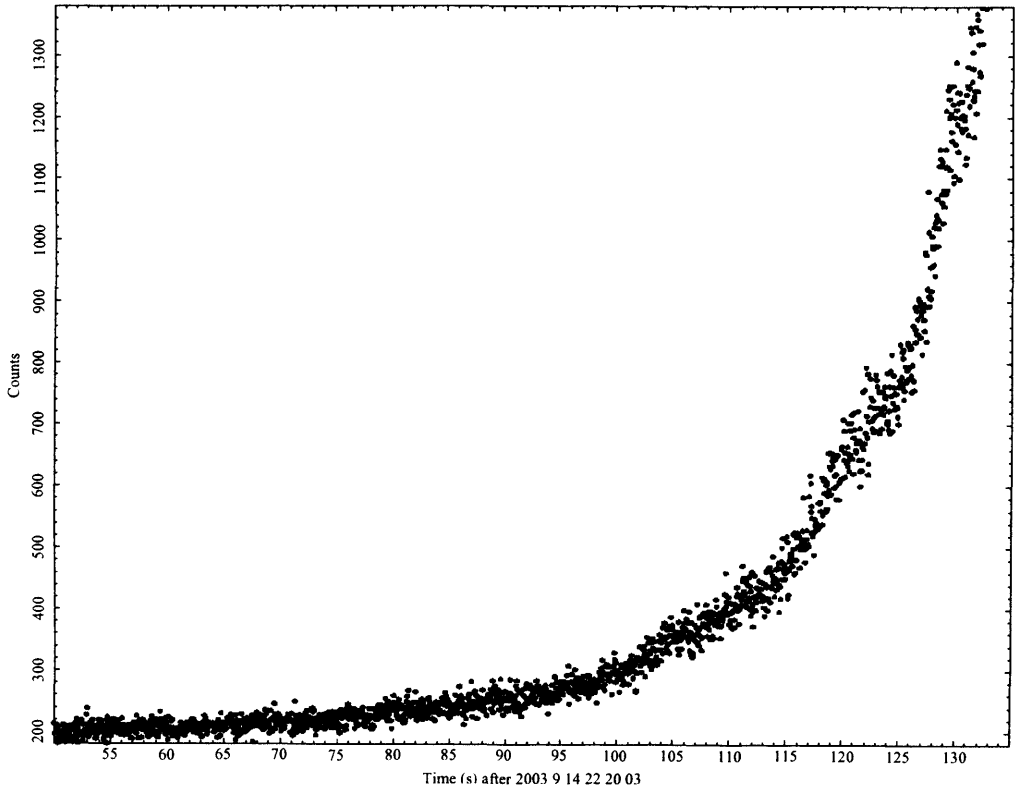

Figure 4.15: Glonass photometry plot - emergence from eclipse

Table 4.2 shows the time offsets for a series of eclipse entry/exit times between ENVISAT photometric observations and three different Earth models. A small root mean square (RMS) value for these time offsets suggests a greater degree of accuracy in the model. The spheroidal model uses the algorithm described here with p = 6378.137 km and q = 6356.752 km (Montenbruck, O. & Gill, E., 2000), the spherical model uses p = q = 6378.137 km and the International Earth Rotation Service (IERS) model uses a spherical Earth with p = q = 6402.0 km (McCarthy, D., 1996). The data indicate that with standard values for the Earth radii, the above spheroidal algorithm can determine shadow crossing times which demonstrate a significant improvement over comparable spherical models for a low Earth orbiting satellite when tested against photometric observations.

Date	Time from Photometry	Spheroid (seconds)	Sphere (seconds)	IERS (seconds)
17/02/2003	20:36:59	-4	2	12
17/02/2003	22:17:31	0	6	15
18/02/2003	21:45:52	-4	-1	8
17/03/2003	20:53:54	2	8	17
18/03/2003	20:22:15	-2	4	12
18/03/2003	22:02:53	-5	1	10
20/03/2003	20:59:19	2	8	17
21/03/2003	22:08:14	0	6	14
23/03/2003	21:04:44	3	9	18
24/03/2003	20:33:02	2	8	16
27/03/2003	20:38:28	2	8	16
27/03/2003	22:19:04	1	7	16
07/04/2003	21:31:58	2	7	16
	Mean offset (secs)	0.3	6.0	14.5
	RMS (secs)	2.6	6.4	14.5

Table 4.2: Eclipse entry / exit time offsets between models and ENVISAT photometry

The mean and RMS offsets shown in Table 4.2 show that the spheroid model has errors which are distributed about zero whereas both the spheroid and the IERS models appear to have strong biases.

For low Earth orbiting satellites, an incorrect transition point will introduce a systematic bias over many orbit revolutions. Polar orbiters, such as ENVISAT (Table 4.1), may be subject to a difference of several minutes (when added over several orbits) spent in eclipse when comparing those predicted by a spherical Earth model against those from the current algorithm. In terms of efficiency, the algorithm developed here runs 13.4 times faster than an alternative oblate Earth technique (Vokrouhlický, D., 1996) when determining 1 million eclipse states on a dual processor AMD Athlon 2200+ machine.

4.6 Modelling of penumbra flux

4.6.1 Introduction

On entering the penumbra, the flux gradually diminishes until it reaches zero in the umbra. If this reduction in flux is modelled, then the forces that are a result of solar radiation can be calculated. However, this extra computation will only be of benefit in orbit prediction if the forces are large enough and act for long enough to make a noticeable difference to the satellite's orbit. The penumbra is a relatively small region, though its size increases with orbit altitude. If a medium earth orbiting spacecraft at GPS attitude was to travel straight through it, the time taken would be ~1-2 minutes. There are however certain configurations of the sun-earth-satellite geometry which at a certain inclination of orbit cause the satellite to graze through the penumbra, spending an appreciable time in this region. A simple calculation was carried out to estimate what the maximum time spent in the penumbra would be, taking a GPS spacecraft as example.

4.6.2 Maximum time spent in penumbra

The maximum time possible for a GPS IIR satellite to spend in penumbra is calculated based upon the orbit of the satellite and the geometry of the umbra and penumbra. For this calculation, the earth was assumed to be spherical. Figure 4.16 shows the Sun, Earth and shadow region geometry. R_s is the radius of the sun, R_E is the radius of the earth, r_s is the distance from the centre of the earth to the centre of the sun, a is the radius of the

satellite orbit (assumed to be circular in this case). α, β, x and y are angles and distances that are marked on the diagram and used in the calculations below.

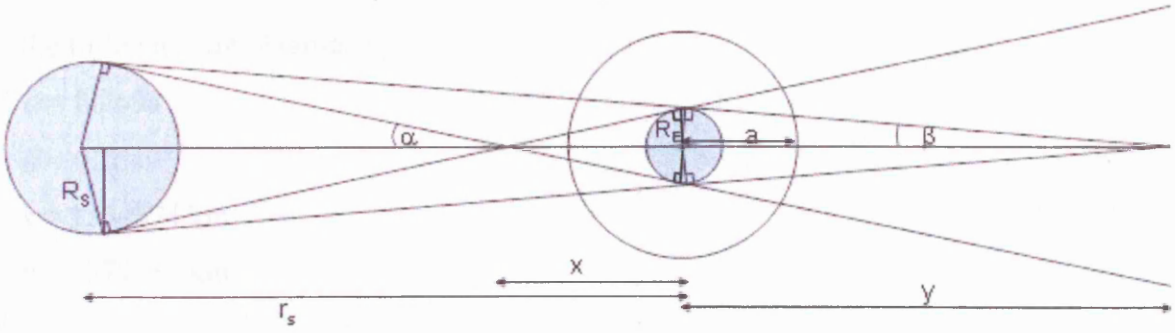

Figure 4.16: Sun, Earth and shadow region geometry

At 26000 km from the geocentre (which is approximately the size of the semi-major axis of a GPS orbit), the size of the umbra and penumbra can be calculated as follows:

$$\sin\alpha = \frac{R_E}{x} = \frac{R_s}{r_s - x}$$

$$x = \frac{R_E r_s}{R_S + R_E} \tag{4.51}$$

$$\sin\beta = \frac{R_E}{y} = \frac{R_s}{r_s + y}$$

$$y = \frac{R_E r_s}{R_S - R_E} \tag{4.52}$$

Figure 4.17 shows a cross-section of the penumbral and the umbral cones. The radius of the circular section through the penumbral cone at satellite altitude a, (h_p) is given by:

$$h_p = (x + a)\tan\alpha \tag{4.53}$$

and the radius of the circular section through the umbral cone at satellite altitude a, (h_u):

$$h_u = (y - a)\tan\beta \tag{4.54}$$

Using the following values:

R_s =70000 km

R_E =6378 km

r_s =150000000km

a = 26000 km

the following are obtained:

α = 0.2698

β = 0.2649

x = 1354374 km

y = 1379282 km

h_p = 6500.1 km

h_u = 6256.8 km

To find a ball park figure for the amount of time spent in penumbra, Figure 4.17 can be used.

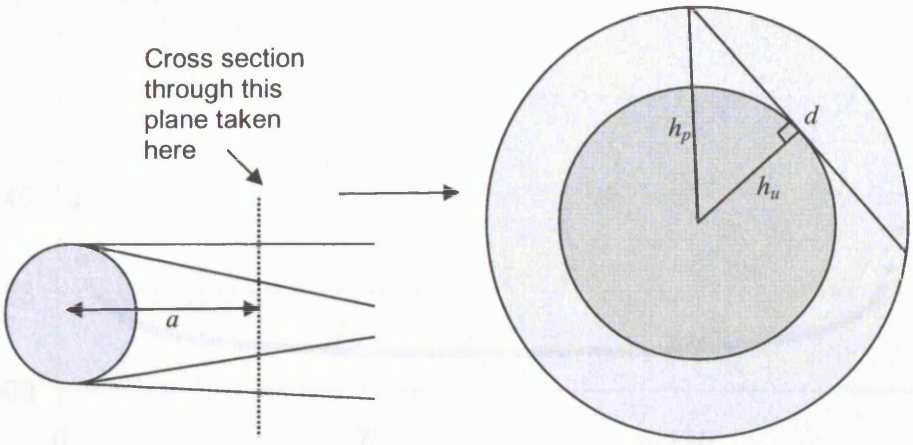

Figure 4.17: Schematic of cross-section of eclipse region

The distance d is then given by:

$$d = 2\sqrt{h_p^{\,2} - h_u^{\,2}} \tag{4.55}$$

and evaluation of Equation 4.55 gives d = 3523.5 km. If we take the speed of the satellite to be ~ 4kms^{-1}, then the satellite can spend up to 14.7 minutes in the penumbra.

This is a theoretical value to estimate an upper bound to how long the satellite could spend in penumbra. The JPL shadow event files which can be obtained from their ftp site (sideshow.jpl.nasa.gov) record the eclipse crossing times and Figure 4.18 shows the

amount of time that SVN 46 spent in penumbra for each crossing during an eclipse season in 2001. From these plots it can be seen that for most orbits during eclipse season the time spent in eclipse is 1-2 minutes, but at the end of the season the satellite does seem to graze the penumbra without actually ever entering the umbra and consequently spends ~14 minutes in penumbra. This gives good agreement with the predictions of the simple model described above. For this amount of time, larger forces such as SRP will cause significant errors to predicted orbits if forces during this time are ignored. To accurately calculate these forces, knowledge of the attitude is required in penumbra. For GPS Block IIR, the attitude in penumbra is described in Section 5.2.1.

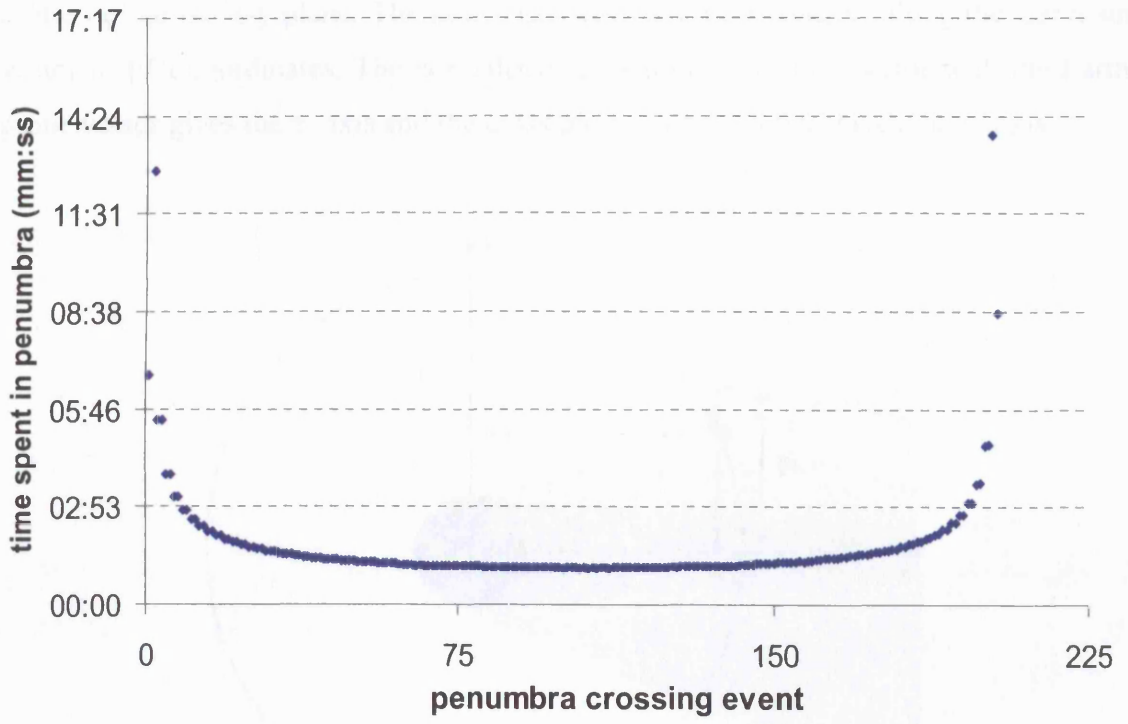

Figure 4.18: Time spent in penumbra per crossing for SVN 46 in Jan/Feb/Mar 2001

4.6.3 Penumbra flux model

To calculate the exact flux in penumbra taking into account an oblate Earth would require the solution of quartic equations, which as mentioned earlier is a computationally intensive process. Though geometrically it would give correct values, there would still be errors because of limb darkening – the fact the sun is less bright at the edges than at the centre (Vokroulicky, D., 1994). Even if this could be accounted for, there is still the problem of refraction of light from the atmosphere, which causes sunlight to be bent into the regions of penumbra and umbra. A refraction model for the

atmosphere is complicated because of its variation with time and place. It was not within the scope of this research to analyse the penumbra flux in such detail and even if this had been done, it would have been cumbersome to implement in a software package, which is a concern of all model development undertaken herein.

A first order approximation for the fall off of flux in the penumbra is to linearly reduce it from the value it has when it enters the penumbra to zero at the umbra.

To do this, it is necessary to transform the coordinates into a basis so that the origin is at the geocentre, the sun is along the positive x-axis and the satellite, geocentre and sun-centre define the x-y plane. The new basis will have its x-axis, x' along the Earth-sun vector in ECI coordinates. The normalised cross product of this vector with the Earth-probe vector gives the z' axis and the cross product of z' with x' gives the y' axis.

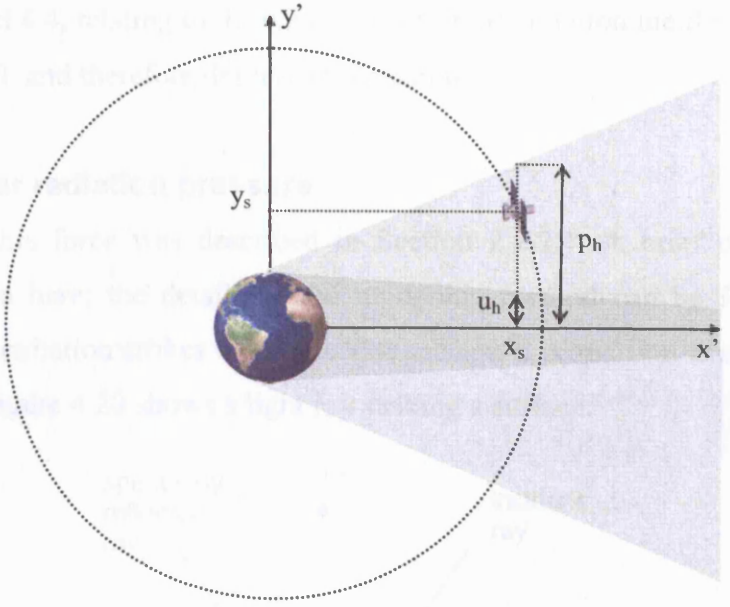

Figure 4.19: Schematic for penumbral height calculation

At the x-value of the satellite the size of the umbra (u_h) and penumbra (p_h) are calculated. This gives the penumbra width. The y-value of the satellite gives the "height of the satellite above the x axis. Then Equation 4.56 gives the proportion of the flux incident on entering eclipse that is still present.

$$\frac{y'-u_h}{p_h-u_h} \tag{4.56}$$

The effects of implementing this preliminary model into orbit prediction software is investigated in Chapter 5.

4.7 Other models required for generation of thermal forces

Descriptions of the models used for the SRP and ERP forces are given in this section. The reasons for their inclusion here are two-fold. Firstly, for thermal force models to be successfully tested in orbit prediction/determination, larger forces, such as those described in Chapter 2 need to be implemented. For many of the forces, standard models are used and will be listed when required; for SRP and ERP however custom models developed within UCL's geodesy group have been employed. Secondly, aspects of both of these models have been adapted for use in the thermal models developed in Sections 4.3 and 4.4, relating to the characterisation of radiation incident upon each part of the spacecraft, and therefore deserve explanation.

4.7.1 Solar radiation pressure

This basis of this force was described in Section 2.2.2.1. A brief overview of this method is given here; the details of the modelling method can be found in Ziebart (2004a). When radiation strikes the spacecraft surface, a proportion is absorbed and the rest reflected. Figure 4.20 shows a light ray striking a surface.

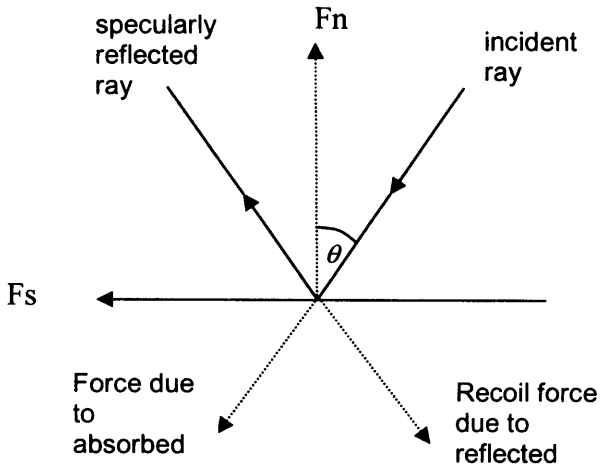

Figure 4.20: Incident ray on spacecraft surface

A physical analysis of the interactions result in the following functions for the normal and shear forces (see Figure 4.20) due to SRP on a flat surface:

$$F_n = -\frac{AW\cos\theta}{c}\left[(1+\mu\nu)\cos\theta + \frac{2}{3}\nu(1-\mu)\right]$$

$$F_s = \frac{AW\cos\theta}{c}\left[(1-\mu\nu)\sin\theta\right]$$

where:

F_n the force normal to the surface (N)

F_s the shear force or the force along the surface (N)

A surface area of component (m^2)

W solar irradiance Wm^{-2}

θ angle of incidence of incoming radiation

ν reflectivity of component

μ specularity of component

c speed of light in a vacuum (299792458 ms^{-1})

For complicated spacecraft geometries, calculation of the radiation flux incident on each surface poses a difficult problem, due to irregular 3D surfaces and shadowing of some components by others. The solar photon flux is simulated using a pixel array which is projected towards a computer simulation of the spacecraft. Ray tracing techniques from each pixel are used to determine which parts of the satellite are illuminated. The effect of radiation reflected specularly and intersecting with other parts of the spacecraft is modelled. The method deals automatically with the shadowing of one part of the spacecraft by another. Figure 4.21 shows the pixel array projected onto the spacecraft model.

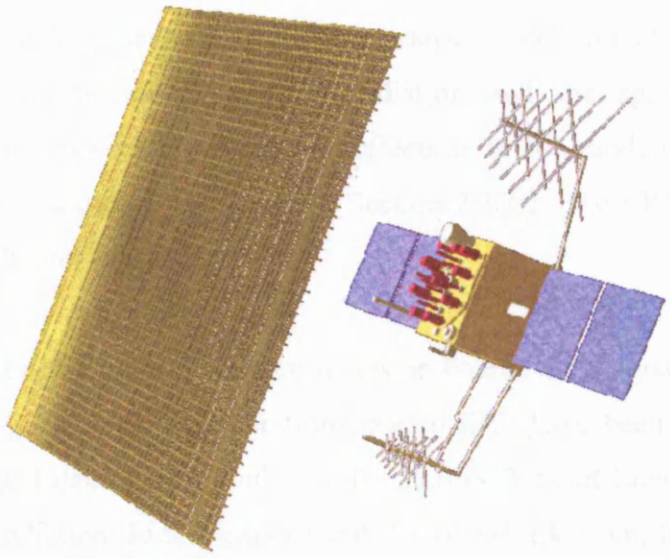

Figure 4.21: Projection of pixel array onto spacecraft structure from one direction

The pixel array is then rotated around the spacecraft and the solar panels are adjusted to track the pixel array as they would track the Sun on orbit. This process is repeated for all possible sun directions. The output from the software for any one orientation of the pixel array is the acceleration of the spacecraft due to the SRP expressed in the BFS XYZ axes. This yields a number of discrete snapshots of the response of the satellite to the radiation flux. Orbit integration requires a continuous model, and this is calculated by fitting an appropriate mathematical model to the data. This could be, for example, a Fourier series or a grid file. A particular strength of this technique is that it deals with the high geometrical complexity of real spacecraft as no simplification is made to the spacecraft structural data.

By using the pixel array method in the calculation of the thermal force due to MLI, the thermal force can be combined with the SRP force for the spacecraft bus. This results in a computationally efficient algorithm for calculation of the solar driven non-conservative forces.

4.7.2 Earth radiation pressure

The physical modelling of the ERP force is similar to SRP in that the force is produced by the interaction of electromagnetic radiation and the spacecraft surface. The fundamental difference between the two effects is in the modelling of the irradiance from the radiation source as discussed in Section 2.2.2.2. The ERP models used in this study are described in Ziebart (2004b).

Probes exist in Earth's orbit with instruments on board, whose goals are to quantify the radiation leaving the earth. Accelerations due to ERP have been derived from space-and-time averaged data from Clouds and the Earth's Radiant Energy System (CERES) and the Earth Radiation Budget Experiment (ERBE) (Barkstrom, B., 1984; Weilicki, B. et al., 1996). Combined data from these two probes provide global grided monthly estimates of longwave and shortwave earth radiation fluxes emitted from the top of the atmosphere (TOA) (30km) from 1984 until at least the end of the current decade. The spatial resolution of data is such that each grid cell represents an area of 2.5° longitude by 2.5° latitude.

The model used in this study was developed based on the assumption that the emitting surface emits energy into the hemisphere above the point source at the centre of a grid and that the surface behaves like a Lambert diffuser (Chapman, A., 1984). The TOA values are manipulated based on these assumptions to provide the contribution of each grid cell at the required altitude. The total radiation received at the satellite can be obtained by summing contributions from each grid cell to that point in space. The interaction of the flux with a box-and-wing model of GPS Block IIR is calculated and a Fourier series is fitted to a time series of the resulting accelerations. During the orbit integration, this function is computed at the required epoch.

Summary

This chapter has described the main techniques developed to compute thermal forces from a spacecraft surface for use in orbit computations. Methods for the treatment of the solar panels and for MLI covered surfaces are derived, and an initial attempt at characterising the thermal force due to earth radiation pressure effects for GNSS altitude satellites has been explained. Methods for determining eclipse boundary crossing times for an oblate earth and for estimating the flux in penumbral regions have been

developed. In Part III, these methods will be applied to the GPS Block IIR and Jason-1 spacecraft, and tested in model computations. A brief overview is given for the solar radiation pressure and earth radiation pressure models which are used in parts of the thermal modelling process.

Part III

Test Cases

The methods developed in Chapter 4 were used to compute models for two satellites: GPS Block IIR, the most recent Global Positioning System (GPS) space vehicle deployed in orbit (at the time of writing), and Jason-1, a joint CNES/NASA altimetry satellite. Chapters 5 and 6 describe the implementation of the model, testing methods and results of these tests for each satellite.

The test cases differ significantly in terms of orbit, structure, mass and attitude regimes and are subject to different characteristic particulate and electromagnetic radiation fluxes. Their main characteristics are summarized in Table III.1.

	GPS Block IIR	Jason-1
Altitude	20200 km	1336 km
Mass	1100 kg	489.1 kg
Area/mass ratio[7]	0.013 m^2kg^{-1}	0.025 m^2kg^{-1}
Orbital period	11 hrs 56 mins	1 hr 52 mins
Orbital inclination	55°	66°

Table III.1: Characteristics of GPS Block IIR and Jason-1

At GPS altitude the atmosphere is greatly rarefied and in terms of affecting the motion of a spacecraft, atmospheric drag is considered insignificant (Jacchia, L., 1977). GPS force models can be tested by comparing predicted orbits based on numerical integration of the force models with post-processed precise orbits. The rationale for this is that orbit prediction is central to the GPS operational concept.

The altitude of Jason-1 was specifically chosen to balance the trade off between achieving a short probe-surface range whist still minimising drag effects. It does however still suffer from drag perturbations which are complicated to predict (see Section 2.2.2.3) and as yet no accurate analytical modelling for this force exists. Estimates made using a typical value for the drag coefficient, yielded accelerations ranging between 3.4 x 10^{-8} to 3.9 x 10^{-10} ms^{-2} (depending on atmospheric temperatures

[7] Area refers to maximum spacecraft profile

and densities). As these are one to two orders of magnitude larger than the thermal force effects, orbit prediction based on dynamic models is not suitable for testing thermal models. The thermal models for Jason-1 are to be tested by incorporation into orbit determination software (described in Section 6.4.1), in which drag forces are estimated empirically.

These satellites have been chosen as test cases for two main reasons. Firstly, both spacecraft require precise orbits to meet their mission objectives. Secondly, GPS Block IIR and Jason-1 spacecraft differ substantially (see Table III.1) and, if application of the methods developed in this study appears to improve orbit prediction/determination for both spacecraft, the validity of the model in the general case is strengthened.

Chapter 5 GPS Block IIR

Chapter outline

This chapter contains a brief overview of the GPS system and its architecture. A detailed description of the structural, material and optical properties and attitude regime of GPS Block IIR is given. The computation and implementation of the methods discussed in Chapter 4 are described. The methods are tested and results of these tests are shown. This chapter includes a brief analysis and discussion of the results.

5.1 Overview of GPS system

The GPS IIR satellite is the most recent model of operational satellites that comprise the Global Positioning System (GPS) space segment. GPS is used to obtain three dimensional positioning anywhere on the surface of the earth or for satellites in lower orbits. GPS was primarily developed as a navigation system, but now has widespread uses in precise geodetic applications.

The fundamental navigation principle is based on the measurement of so called "pseudoranges" between the user and a minimum of four satellites. The spacecraft positions are considered to be known in a suitable reference frame. Geometrically three range measurements are required, and a fourth is necessary to correct for errors in the receiver clock. This clock error is the reason for the term "pseudorange". For real time single receiver positioning, each GPS satellite emits a signal modulated with a specific code sequence of binary values, known as a pseudorandom noise (PRN) code. To determine the signal propagation time, the user needs a copy of this code sequence in the receiver. The code sequence is phase shifted in time until maximum correlation is achieved and the necessary phase shift is a measure of the signal travel time between the satellite and the receiver antennas.

For geodetic applications which require much higher precision, observations of the phase of the transmitted carrier wave (termed a phase observable) are used. This is a lengthier process as it requires the solution to the problem of ambiguity resolution. This

is not discussed further here; for a comprehensive description of GPS systems the reader is referred to the following texts: GPS Satellite Surveying, Leick, 2004 & Satellite Geodesy, Seeber, 2003.

5.1.1 System architecture

The GPS system consists of three segments:

- Space segment
- User segment
- Control segment

The space segment currently (November, 2004) consists of a constellation of 30 satellites in near circular orbits which are inclined at 55° and have a period of almost 12 hours. These satellites are in medium earth orbits at altitudes of 20200 km. The satellites occupy 6 planes separated by 60 degrees, and the satellites are distributed over the planes. The constellation design criterion was that 4 satellites should be visible anywhere on earth 24 hours a day (Seeber, G., 2003).

The user segment consists of receivers on the ground (or in space, in the air or at sea) which pick up signals emitted by the space segment. This data is used to solve for position and velocity of the receiver. The spacecraft positions derived from the predicted orbit effectively define the user's real-time reference frame. Obviously any errors in the orbit prediction will propagate directly into errors in the position and velocity of the user's receiver. Depending on variables such as the receiver type, the amount of data recorded and the sophistication of the processing technique used, varying degrees of accuracy in the calculated position and velocity can be attained. In terms of absolute positions this can vary from 20m down to a few centimetres.

The control segment consists of a global network of ground stations, which continuously track the spacecraft throughout the course of their orbits. The tracking data is transmitted from the ground stations to a Master Control Station (MCS). At the MCS, these data are combined with models of the forces acting on the spacecraft to predict the orbital trajectory of each satellite 12-48 hours in advance. These data are uploaded to

the spacecraft. As each spacecraft orbits the Earth, it emits the signals from which the psuedoranges are calculated, and another signal containing the data message. The data message includes spacecraft orbit parameters (derived from the predicted orbit) from which the position of satellite can be computed. This information is termed the 'broadcast ephemeris' and is described in more detail in Section 5.1.2.

5.1.2 Broadcast ephemeris

As stated in Section 5.1.1.3, the broadcast ephemeris contains estimates of future orbit information for each satellite which have been computed by the MCS based on observation data from monitor stations. The monitor stations receive all satellite signals from which their pseudoranges (from the station to the satellite) are determined. These are transmitted along with local meteorological data (which will affect the calculation of ranges) to the MCS. The MCS uses several days of data to pre-compute the satellite ephemeredes and the behaviour of the satellite clocks. These parameter sets cover several days and are transmitted to the ground antennas, then uplinked to the satellites which broadcast the appropriate set when transmitting to a receiver. Currently the satellite is uploaded with new orbital parameters approximately every two hours (Misra, P., 2001). For the ideal case of the 2-body problem, (Section 2.1), only 6 elements are required to specify the position and velocity of the satellite at any future time. For a real spacecraft, the perturbing forces cause the orbit to change with time, and the orbit has to be characterised by a set of time dependent parameters. GPS accounts for these perturbations with an expanded orbital set which retains a Keplerian "look". This parameter set was chosen in the 1970s as a compromise between obtaining the required accuracy without burdening a receiver with undue computational and storage requirements. The estimated satellite positions are represented by an expanded set of quasi-Keplerian parameters consisting of orbital elements at a particular epoch, parameters describing how the elements will change with time and additional perturbation and time-related parameters.

5.2 GPS IIR spacecraft description and data sources

The GPS spacecraft bus consists of a rectangular box with a shroud covering the antenna array which is on the +Z axis face (see Figure 5.1). The bus is mostly covered in multilayer insulation. Power is supplied to the spacecraft by silicon cells mounted on

solar arrays. The panel axis is aligned with the Y-axis, and two large solar panels flank each side of the bus. Large W-sensor antennae, used for military communication, are attached to the bus (Fliegel, H. & Gallini, T., 1996). The nominal mass of GPS Block IIR spacecraft is 1100kg, though the actual values vary slightly for each satellite, and change over time due to fuel burns.

A computer simulation of the spacecraft is shown in Figure 5.1. The raw data from which the spacecraft model was created have been derived from Fliegel (1996) and from technical drawings of the bus. This data is documented in Section 5.2.1. Curved surface structures are simulated using geometrical primitives such as paraboloids, cones and spheres, i.e. there is no simplification of the surface geometry. In total 218 components were used for the spacecraft model of GPS IIR. A series of quality control tests were carried out to assess the integrity of the simulations (Ziebart, M. et al., 2003b).

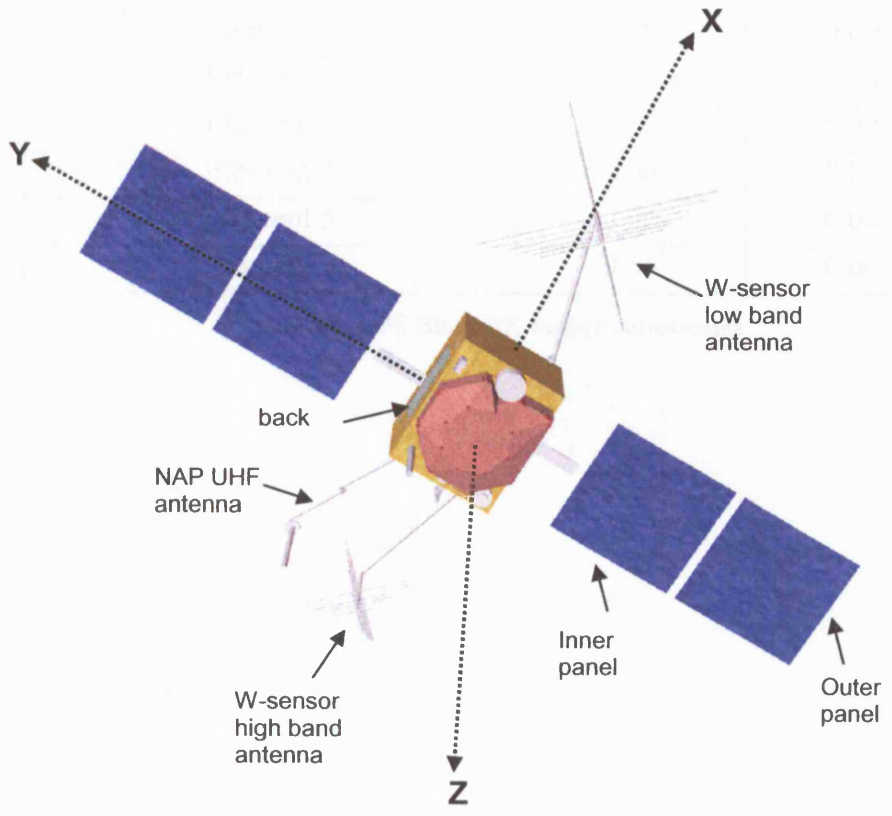

Figure 5.1: Geometrical form of the GPS Block IIR satellite used in this study

Table 5.1 contains optical properties of the surfaces on the GPS Block IIR spacecraft. Figures 5.2 and 5.3 are technical drawings of the spacecraft.

SV component	Reflectivity	Specularity
Exposed panel beams (each of two)	0.85	0.85
Plume shield	0.06	0.00
Antenna Shroud	0.06	0.00
W-sensor elements (low band)		
Element 1	0.06	0.00
Element 2	0.06	0.00
Element 3	0.06	0.00
Element 4	0.06	0.00
Element 5	0.06	0.00
Element 6		
W-sensor elements (high band)		
Element 1	0.06	0.00
Element 2	0.06	0.00
Element 3	0.06	0.00
Element 4	0.06	0.00
Element 5	0.06	0.00
Element 6	0.06	0.00

Table 5.1: GPS Block IIR surface components

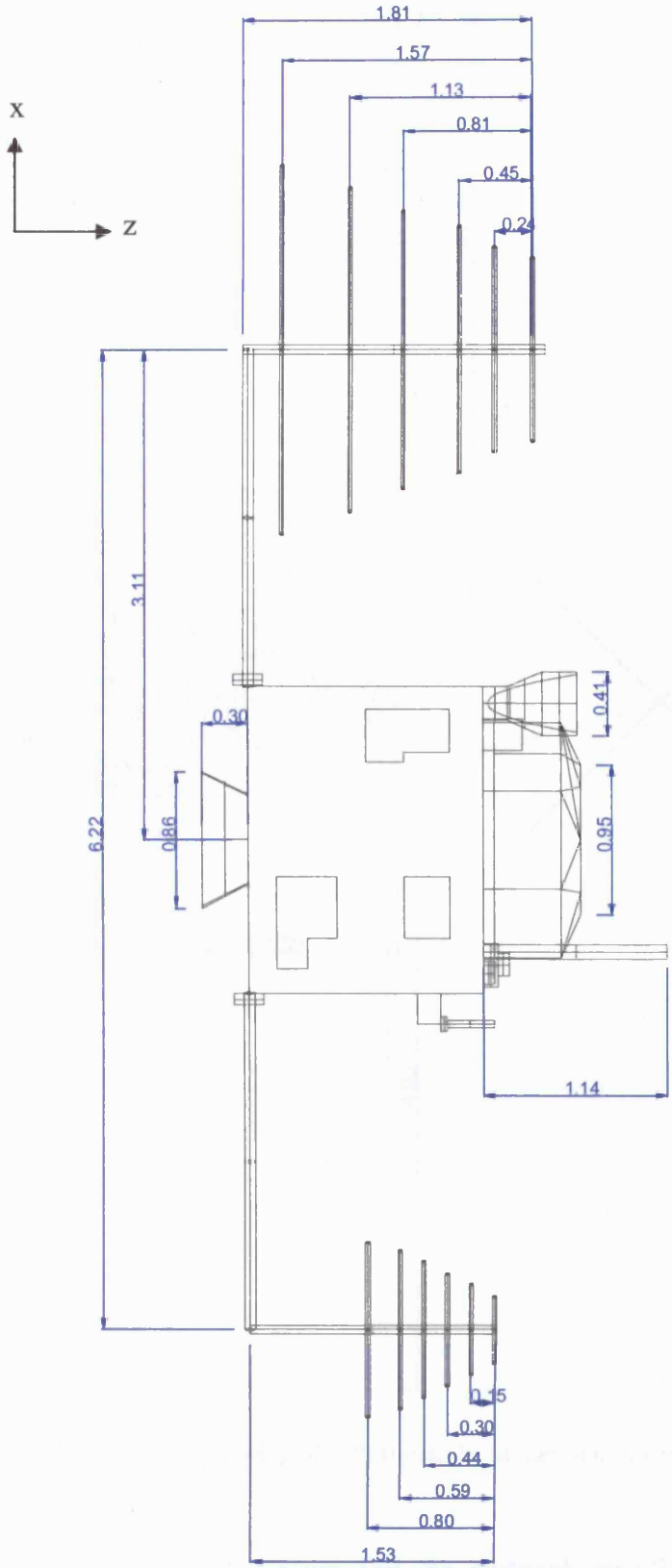

Figure 5.2: Technical drawing of GPS Block IIR (dimensions are in metres)

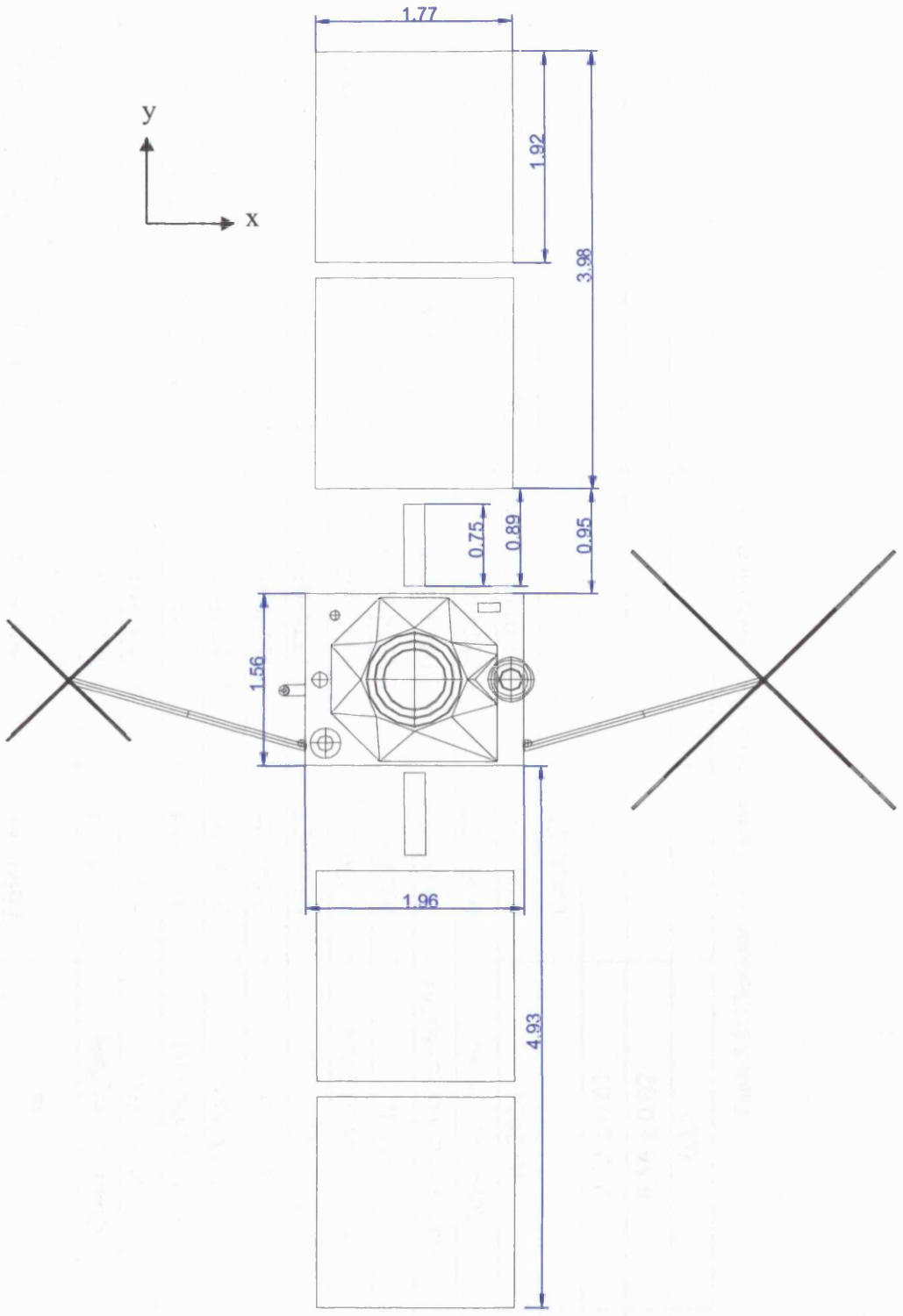

Figure 5.3: Technical drawing of GPS Block IIR (dimensions are in metres)

The solar panel comprises of 11 layers and the material specifications and optical properties of the front and the back of the solar panel are given in Table 5.2.

Layer	Material	Thickness (m)	Conductivity (W/m/k)	Density (kg/m^3)	Specific Heat Capacity (J/kg/K)
1	Quartz coverglass	0.000254	1.417322835	2615.751168	627.9867123
2	DC 93-500	5.08E-05	0.157480315	1079.516355	1674.631233
3	Silicon solar cell	0.000254	150	2524.407477	749.3952721
4	RTV 566	0.000102	0.157480315	1522.39486	1674.631233
5	Kapton	2.54E-05	0.157480315	1425.515187	1092.699084
6	BR36 adhesive	0.000127	0.157480315	1060.140421	1674.631233
7	Face sheet Al 2024	0.000254	188.976378	2767.990654	962.9129589
8	FM 36	0.000127	0.157480315	1154.252103	1674.631233
9	Al honey comb core (5056)	0.0254	2.031496063	33.21588785	962.9129589
10	Adhesive FM 36	0.000127	0.157480315	1154.252103	1674.631233
11	Al 2024	0.000254	188.976378	2767.990654	962.9129589
Total		**0.026975**			
Front face absorptivity	0.72 ± 0.03				
Front face emissivity	0.86 ± 0.02				
Back face emissivity	0.89				

Table 5.2: Characteristics of solar panel layers for GPS Block IIR

At any time, power is drawn from either the inner panels or the outer panels. (pers comms, Fliegel, H., April 2003); if power is drawn from a panel, it is at a nominal rate of 90 Wm^{-2}. This causes differences in temperatures and forces exerted by the inner and outer panels. Since GPS Block IIR attitude regime requires that the solar panels are always sun facing, the perpendicular area presented to the sun is constant and the resulting force varies as a function of sun-probe distance.

5.2.1 GPS IIR attitude

The attitude of the satellite is determined by the requirement that the navigation antennae which are aligned along the spacecraft fixed Z-axis point towards the geocentre and that the solar arrays, mounted along the spacecraft fixed Y-axis face the sun[8]. The spacecraft fixed X-axis is required to lie in the hemisphere containing the sun. Except at the two singular points when the Earth, Sun and spacecraft are collinear, this regime uniquely defines the attitude of the spacecraft. The angle between the Earth–satellite and the satellite-Sun lines is the Earth-Probe-Sun (EPS) angle (Figure 5.4). From the spacecraft point of view, the Earth is continually on the BFS Z-axis, and the Sun appears to rise and set confined to the BFS X-Z plane (Ziebart, M., 2004a). When the satellite is in full sunlight, its attitude is controlled to meet the above requirements based on the output of solar sensors mounted on the solar panels. When the spacecraft cannot see the sun, the attitude is set to a fixed yaw regime (the yaw refers to the rotation of the spacecraft bus). In this fixed yaw regime, the spacecraft emerges from the shadow region close to its nominal attitude[9] (Bar-Sever, Y., 1997).

---

[8] Mis-alignment of these panels could be the cause of reported Y-bias effects for some spacecraft (Fliegel, H. & Gallini, T., 1996)

[9] Originally, the yaw attitude of the spacecraft was determined by measurements made by solar sensors mounted on the solar panels. It was noticed however that for the Block II and IIA satellites, computed orbits of eclipsing satellites were less accurate than for their non-eclipsing counterparts. This was because in the absence of the sun, the output from the solar sensors was essentially zero, and the output was driven by noise in the system, leading to erratic yawing during shadow crossing. To fix this problem, a constant small bias was introduced, so that the sun sensor's signal was superposed with another signal (the bias), equivalent to a yaw error of 0.5°, to allow the attitude in eclipse to be modelled. As a result, when the sun was observed, the yaw attitude was in 0.5° error with respect to its actual orientation. It was expected that

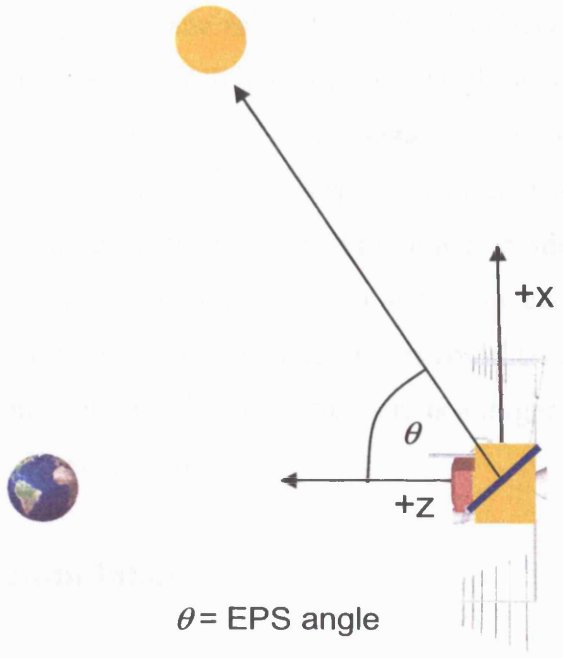

Figure 5.4: Attitude of GPS Block IIR

5.2.2 Antenna thrust

Transmission of the navigation signals results in a reactive force on the satellite, as described in Section 2.2.3.5. A value for the signal power of 77 W was supplied by JPL. This is equivalent to a force of 2.6×10^{-7} N, which acts constantly in the satellite radial direction.

5.2.3 Other surfaces

The remaining large structures on the surface of the GPS Block IIR spacecraft are the W-sensor high and low band antennae and the NAP UHF antenna (see Figure 5.1). These are composed of thin cylindrical components made of aluminium, covered in black tape (Fliegel, H. & Gallini, T., 1996). Due to the high conductivity of aluminium, it is probable that uniform temperature distributions about the axis of each cylinder will result. In these cases, any thermal force will be cancelled out by another in the opposite direction, and therefore the net force will sum to a zero.

---

this error would be negligible, but actually the yaw error appeared to be more than 0.5° in full sunlight, hence the new regime was implemented for GPS Block IIR (Bar Sever, Y., 1996a, 1996b).

In order to increase the lifetime of the electronic subsystems in the satellite bus, the internal temperature of the bus is maintained at (~20° C) (Galvin, D., 1999). The only means of rejecting heat generated within the bus is through radiation to space. The GPS satellites use radiators (see Figure 5.1). These radiators are on the +Y and –Y faces of the spacecraft positioned so as to avoid direct solar radiation. Unfortunately, no specific data was available for these vents. If the assumption is made that energy is output symmetrically, the forces due to this emission will also cancel each other out. If however they do not emit energy at the same rate, it could be another cause of the Y-bias effect (discussed in Section 3.3.2.2), where there is a larger force in the Y-direction than expected (Fliegel, H. et al., 1992).

5.3 Model computation

5.3.1 MLI

Almost all the faces of the GPS Block IIR bus are covered in MLI including the plume shield and the antenna shroud. The pixel array method was used to compute accelerations for SRP and thermal response of MLI surfaces. A pixel resolution of 2mm was used, with the pixel array positioned at separate points every 2 degrees around the satellite (that is a step size of 2° in EPS angle). A nominal flux value of 1 AU was used which was scaled for the actual probe-sun distance when used in an orbit computation.

Figure 5.5 shows the spacecraft BFS X, Y and Z accelerations as a function of EPS angle.

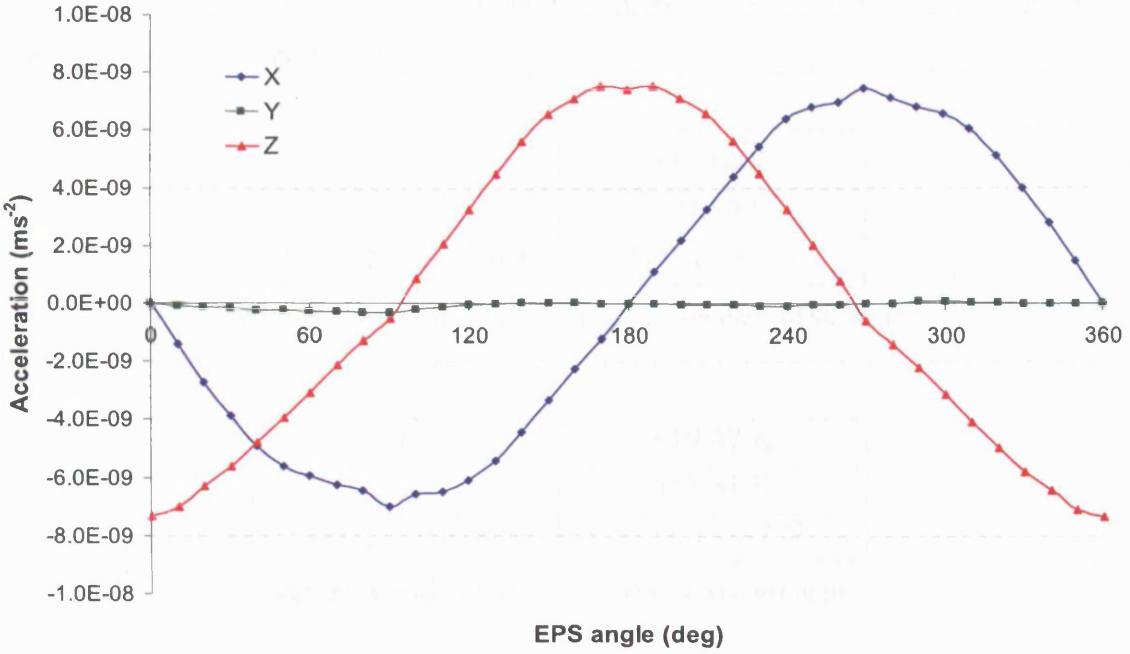

Figure 5.5: BFS X, Y and Z accelerations as a function of EPS angle due to MLI surfaces

The resulting accelerations were expressed as three Fourier series (accelerations as a function of EPS angle), each using 179 coefficients, one for each satellite BFS axis. On-orbit forces are determined based on the EPS angle at the epoch of interest.

The accelerations in the ±Y axis directions are non-zero due to the asymmetry of structures on the +Z face (mainly of the MLI shroud) of the GPS Block IIR spacecraft. This produces an a priori model of the Y-bias.

5.3.2 Solar panels

The total resistance was calculated by the method described in Section 4.2.2 to have the value of:

$$R_{total} = 0.016055929 \text{ KW}^{-1}$$

The temperatures of the panels at a particular epoch will differ depending on whether power is being drawn from the panels. Assuming that a power of 90 Wm^{-2} is drawn from a panel, Table 5.3 shows the temperatures of the front and back surfaces and the force that results at a distance of one astronomical unit from the earth (a solar flux of

1368 Wm^{-2}) when the solar flux is normal to the panels. Table 5.4 summarises the same information if no power is drawn.

T_f	311.64 K
T_b	304.59 K
Force per unit area	7.60 x 10-7 N

Table 5.3: Solar panel data assuming a power draw of 90 Wm^{-2}

T_f	319.47 K
T_b	311.81 K
Force per unit area	9.32 x 10-7 N

Table 5.4: Solar panel data assuming no power draw

In the calculation of the TRR force due to the solar panels, it is assumed that power is drawn from half the panels at any time, and that the power draw is symmetrical (i.e. both inner panels "on", or both outer panels "on").

The method described in Section 4.2.2.1 is used to calculate the function for the force F (in Newtons) due to the solar panels as a function of flux, x, and is given by:

$$F = -4.80 \times 10^{-13} x^2 - 9.70 \times 10^{-12} x + 1.47 \times 10^{-7} \text{ N}$$

where the force vector is in the probe-sun direction as shown in Figure 5.6.

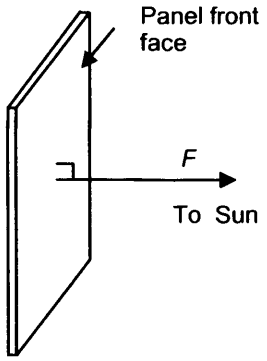

Figure 5.6: Direction of force vector

5.4 Testing methodology

The critical step in the process of modelling surface thermal forces is the evaluation of surface temperatures. In this section, the first two methods test how well the modelled solar panels temperatures compare to solar panel temperature data available from other sources. This study aims to develop force models which improve the definition of a satellite's motion. The third test method predicts orbits and examines whether predictions improve on the incorporation of the newly developed force models.

5.4.1 Testing methods 1: Comparison with telemetry

Telemetered data (of a few GPS Block IIR spacecraft) from temperature sensors situated on the front of the solar panels were available from Lockheed Martin. Comparison of modelled temperatures to these temperatures provide an independent check with which to compare the model outputs.

5.4.2 Testing Methods 2: Comparisons with other methods

There are many commercial software tools available for thermal modelling that use Finite Element Analysis (FEA) or Finite Difference solvers to predict heat flow and temperatures. ESATAN is one such tool that has been developed by Alstom[10]. It was released in 1985 and has been the standard thermal analysis code of the European Space Agency (ESA). Theoretically, this software can solve for steady state or transient temperatures for the whole spacecraft at all attitudes if sufficient input data is available, though it may be impractical to implement these results into orbit prediction/determination tools due to the high computational burden. This software is used as a check for the calculation of the solar panel surface temperatures. The results are given in Section 5.5.2.

Additionally, other independent researchers have published calculated values for solar panel temperatures. A comparison with these values is made.

5.4.3 Testing Methods 3: Orbit prediction

The thermal force models and eclipse related models are incorporated into software developed by the Geodesy Research Group at UCL which is used to integrate an orbit

[10] http://www.techcentreuk.power.alstom.com/pdf/ESATAN_Thermal_Analyser.pdf

forward from an initial state vector to produce a predicted orbit. The method of orbit prediction is presented here.

The force models described in Chapter 2 constitute an approximation to the true second-order differential equation of motion of the spacecraft. Shortcomings in the accuracy of the initial conditions (position and velocity at some epoch) and the force model cause the integrated trajectory to diverge from the true orbit. The degree of divergence is used to assess the degree of mis-modelling in the force model. In practice, of course, the true trajectory is never known as attempts to measure it always have some associated error. However, the precise orbits produced by centres such as JPL, CODE and GFZ provide best estimates of the true trajectory of a satellite given all the available data and models. In this analysis JPL precise orbit files were used. These orbit files contain state vectors at 15 minute intervals for GPS satellites.

The steps of the model testing procedure are as follows:

- A state vector is taken from a JPL precise orbit file and defined as the start point of the integration process.
- The spacecraft orbit is numerically integrated forward over 12 hours (one orbit) from this point.
- The position of the satellite is compared to that of the precise trajectory at each 15 minute intervals (this is the maximum resolution of data available in the precise JPL files).
- The difference vector between the predicted and the precise orbits are projected onto the Height-Cross-aLong track (HCL) (see Section 2.3) basis at 15 minute intervals over each trajectory.
- The root mean square errors in each of the height, cross and along-track axes are then calculated.
- The thermal models are then added to the existing model, and comparisons of errors are made before and after these are added.

The orbit prediction software uses an 8^{th} order embedded Runge-Kutta integrator; a ten-second integration step-size was chosen. Tests carried out with a one second step size showed a difference of <1% in orbit prediction results.

5.4.3.1 Force models

The basic force model is known hereafter as Model 1 and accounts for:

- Spherical harmonic Earth gravity field model, to degree and order 15 using GRACE GGM01C coefficients. (Increasing this degree and order added no significant improvement to the results.)
- 3rd body perturbations due to the Sun, Moon, Venus and Mars. Jet Propulsion Laboratory Developmental Ephemerides (JPL DE405) were used to compute third body effects.
- Custom analytical SRP models (Ziebart, M., 2004a) as described in Section 4.7.1.
- Custom albedo models (Ziebart, M. et al., 2004b) as described in Section 4.7.2.
- Solid Earth tide variations to Earth gravitational potential due to the Sun and the Moon
- General relativistic effects
- Pole tides
- Antenna thrust model

The thermal and eclipse related models are added one by one to Model 1 to generate Models 2-5 defined below.

Model 2 = Model 1 + steady state thermal modelling of solar panels, and penumbra flux
Model 3 = Model 2 + models for the parts of the satellite covered in MLI
Model 4 = Model 3 + forces due to thermal albedo
Model 5 = Model 4 but assuming the flux is zero in the penumbral region

Twelve hour arcs were predicted for 5 GPS IIR satellites - SVN 41, 43, 44, 46, 51 over 4 weeks (March 2004), using the models developed here. An arc length of one orbit was chosen to enhance the likelihood of detection of once per orbit revolution dynamic effects. These dates were chosen as masses of each of these satellites during this time were available (pers comms, Fliegel, H., April 2004) and are given in Table 5.5 below.

SVN number	Mass in March 2004 (kg)

41	1098.2535
43	1098.0510
44	1098.5375
46	1086.4512
51	1099.7369

Table 5.5: GPS Block IIR masses for March 2004

5.5 Results

5.5.1 Testing method 1: Comparison with telemetry

Table 5.6 contains the available data which was measured for the six satellites listed over a three year period. The average and standard deviation of the temperatures are given for both + Y and – Y panels at aphelion and perihelion.

	Temperatures (K)			
	+Y		-Y	
SVN	Perihelion	Aphelion	Perihelion	Aphelion
41	317.0	310.0	324.0	320.0
43	320.5	310.5	318.0	311.5
44	322.5	314.0	337.0	317.0
46	330.5	323.0	333.0	325.0
51	325.0	316.5	333.0	323.0
54	330.0	323.0	333.0	328.0
Average	324.3	316.2	329.8	320.6
SD	5.3	5.8	6.8	6.2

Table 5.6: Telemetered temperatures of solar panels

The modelled front face temperatures are:

Perihelion: 314.34 K

Aphelion: 308.54 K

Figure 5.7 shows the telemetered data for the -Y panel of SVN 43 and modelled temperatures over the same three year period.

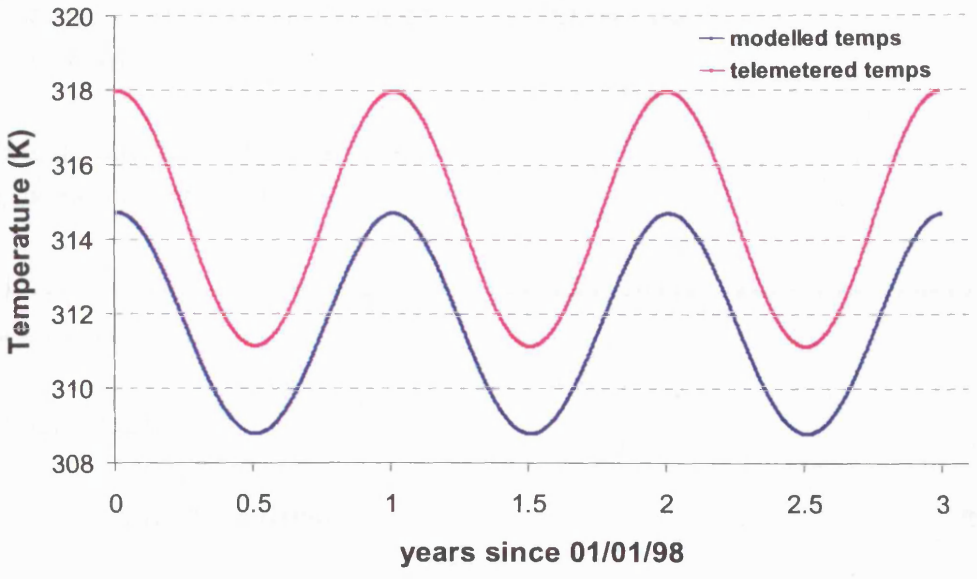

Figure 5.7: SVN 43 front face panel temperatures from telemetry and model data

The difference in temperature between aphelion and perihelion are clearly evident in both sets of data. The telemetered data and the modelled data both show the same pattern, but there is a nearly constant offset between the two of about 3K. Data telemetered from the other Block IIR satellites show constant offsets also, and with only one exception, the offset is always in the same direction.

5.5.2 Testing method 2: Comparisons with other methods

Steady state temperature results are presented using ESATAN. The output of the ESATAN program is included. Node 1 refers to the front face and Node 12 refers to the back face. Temperatures are given in °C. These temperatures are evaluated at a distance from the sun of one astronomical unit and a power draw of 90 Wm^{-2}.

```
EUROPEAN SPACE AGENCY THERMAL ANALYSIS NETWORK (VERSION 8.9.1) PAGE
6
 02   SEPTEMBER   2004                                    09:43:43
SOLAR_PANEL

 $Id: Solar Panel  2003/08/09 $
```

```
 TIMEN =  25000.00       MODULE SLCRNC       DTIMEU =     0.0051
 CSGMIN =**********  AT NODE * IN SUB-MODEL
+SOLAR_PANEL

 TABLE OUTPUT WITH ZENTS = 'L,T'
 FOR NODES OF ZLABEL = ' '

=========================================================================
=========

+SOLAR_PANEL

          NODE   LABEL                                          T (K)

            1    Front Face                                    311.67
            2    Bar                                           311.59
            3    Bar                                           311.53
            4    Bar                                           311.25
            5    Bar                                           311.18
            6    Bar                                           310.82
            7    Bar                                           310.82
            8    Bar                                           310.47
            9    Bar                                           305.07
           10    Bar                                           304.98
           11    Bar                                           304.98
           12    Back Face                                     304.69
           13    Deep space front                                  273.15
           14    Deep space back                                   273.15

=========================================================================
=========
```

5.5.3 Testing method 3: Orbit prediction

The results are presented for 12 hour orbit predictions for 5 GPS IIR satellites (SVN 41, 43, 44, 46, 51), one for each day, over the course of 4 weeks (March 2004), using the models developed here. Tables 5.7 - 5.11 give the mean RMS residuals and standard deviations for each satellite over the test period. Table 5.7 shows the results when no thermal model is included (Model 1); Table 5.8 gives the results when thermal modelling of the panels was included (Model 2) and Table 5.9 gives the results for the

final model which includes thermal modelling of solar panel and MLI (Model 3). Table 5.10 gives the results for when the thermal albedo effect is included along with all the other thermal effects (Model 4). Comparative tests were also carried out on eclipsing satellites with and without inclusion of the penumbra flux model (Table 5.11). No data was rejected on a statistical basis.

SVN	H	C	L	σH	σC	σL
41	1.371	0.262	2.2512	0.058	0.027	0.187
43	1.313	0.352	3.343	0.043	0.029	0.367
44	1.677	0.053	3.522	0.055	0.030	0.675
46	1.160	0.315	4.689	0.076	0.014	0.430
51	1.885	0.110	7.552	0.156	0.018	0.736
W Mean	1.411	0.233	2.997			

Table 5.7: Mean HCL residuals (m) from 28 days of 12 hour predictions, Model 1.

SVN	H	C	L	σH	σC	σL
41	1.248	0.231	2.051	0.053	0.026	0.179
43	1.180	0.322	2.978	0.042	0.028	0.338
44	1.508	0.049	3.168	0.054	0.028	0.595
46	1.049	0.282	4.228	0.076	0.013	0.433
51	1.714	0.109	6.862	0.154	0.017	0.730
W Mean	1.272	0.211	2.691			

Table 5.8: Mean HCL residuals (m) from 28 days of 12 hour predictions, Model 2.

SVN	H	C	L	σH	σC	σL
41	0.222	0.079	0.529	0.034	0.024	0.223
43	0.164	0.111	0.776	0.055	0.022	0.339
44	0.139	0.030	0.615	0.075	0.015	0.424
46	0.142	0.065	0.446	0.051	0.020	0.320
51	0.231	0.108	0.783	0.118	0.015	0.524
W Mean	0.187	0.075	0.586			

Table 5.9: Mean HCL residuals (m) from 28 days of 12 hour predictions, Model 3.

SVN	H	C	L	σH	σC	σL
41	0.223	0.079	0.522	0.033	0.024	0.208
43	0.161	0.111	0.745	0.054	0.022	0.335
44	0.136	0.030	0.585	0.074	0.015	0.419
46	0.144	0.065	0.459	0.051	0.020	0.330
51	0.234	0.108	0.803	0.117	0.014	0.528
W Mean	0.188	0.076	0.577			

Table 5.10: Mean HCL residuals (m) from 28 days of 12 hour predictions, Model 4.

SVN 44	H	C	L	σH	σC	σL
Without penumbra model	0.161	0.032	0.700	0.078	0.014	0.436
With penumbra model	0.130	0.030	0.556	0.069	0.015	0.398

Table 5.11: Mean HCL residuals (m) from 28 days of 12 hour predictions in eclipse

Figures 5.8-5.10 show bar-charts of the data given in Tables 5.7-5.9, and have the same vertical scale. Figure 5.11 represents the same data as Figure 5.10, but using a different scale. Figure 5.12 is a bar-chart of the final thermal model results.

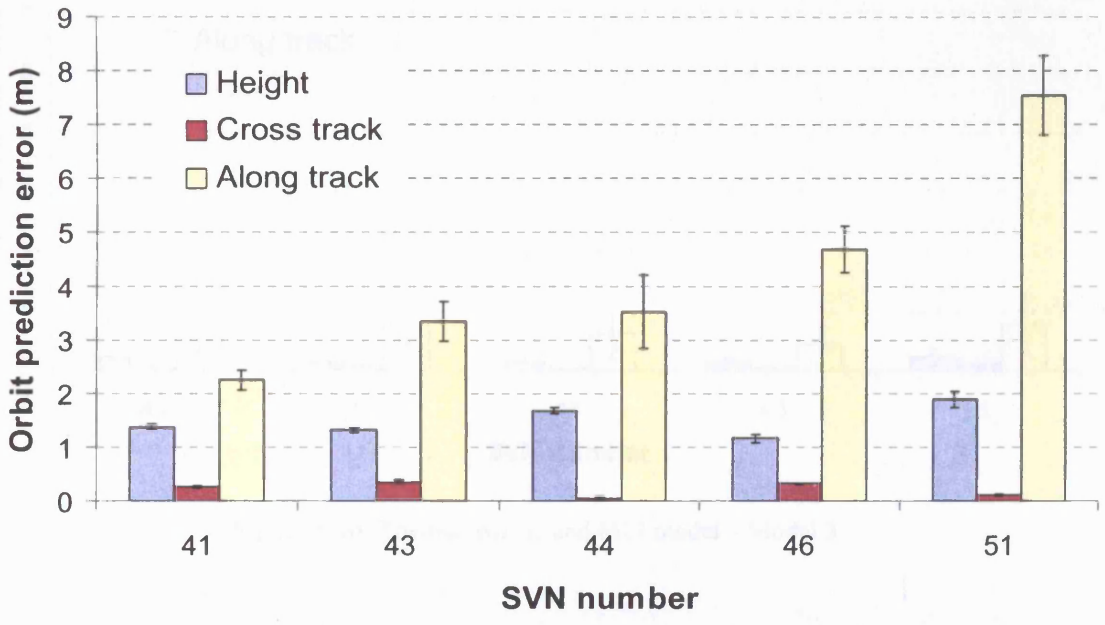

Figure 5.8: No thermal model - Model 1

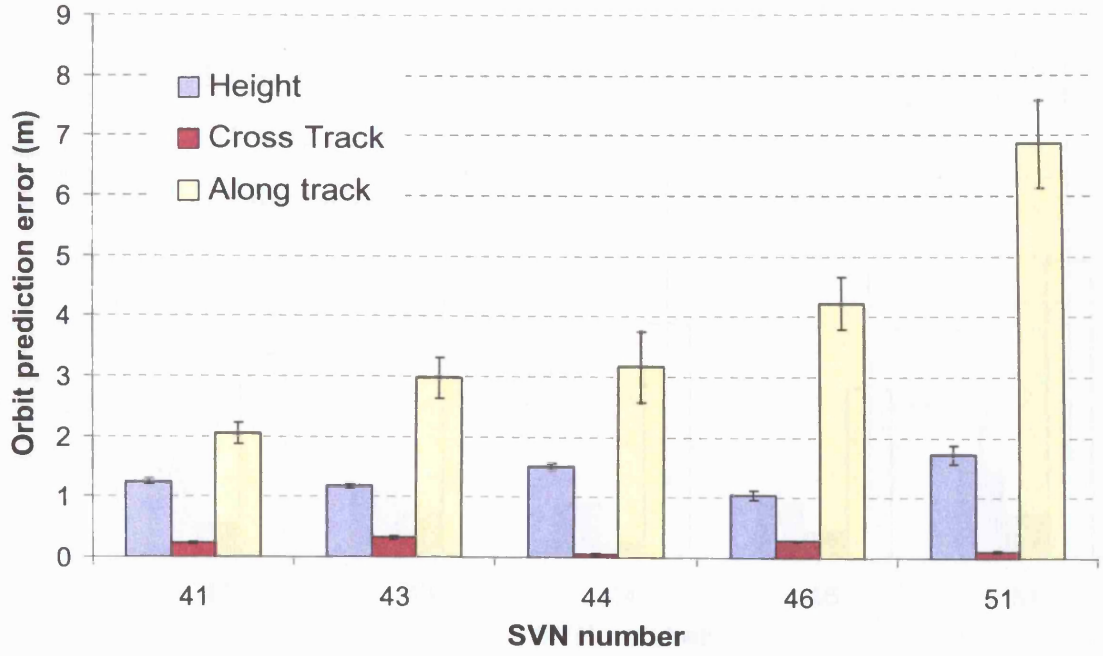

Figure 5.9: Thermal models of solar panels only –Model 2

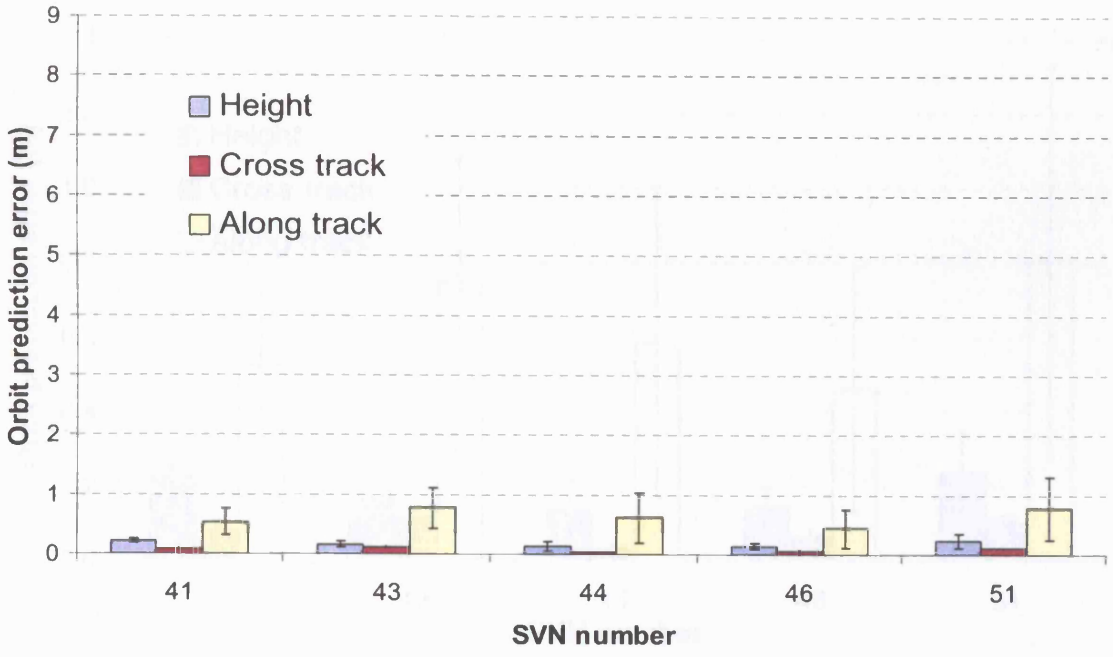

Figure 5.10: Thermal panels and MLI model – Model 3

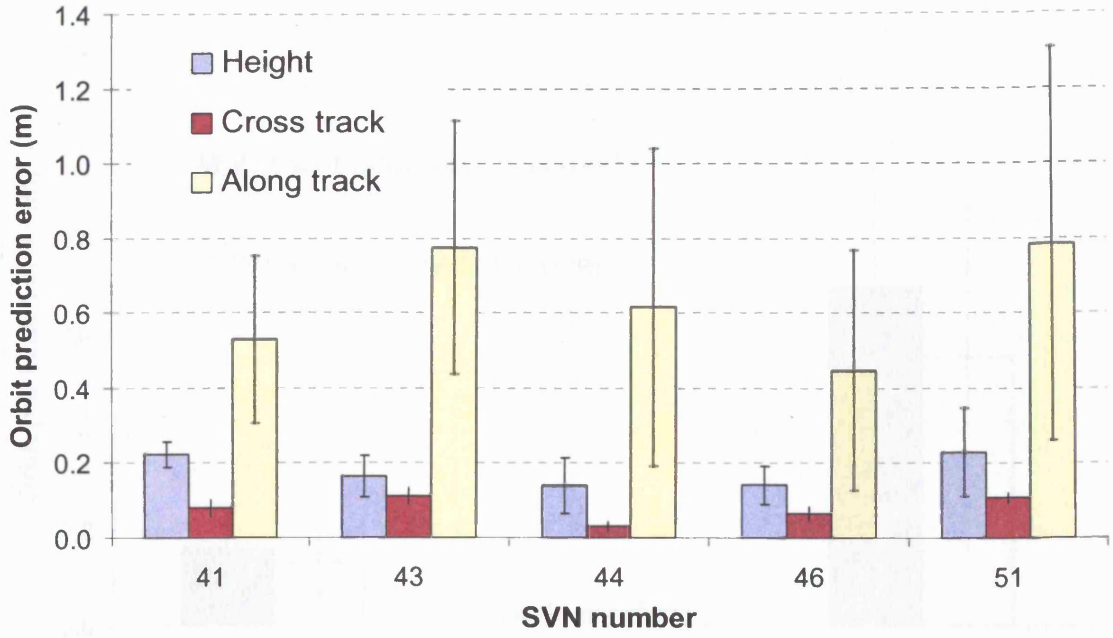

Figure 5.11: Scale change (thermal panel and MLI modelling) –Model 3

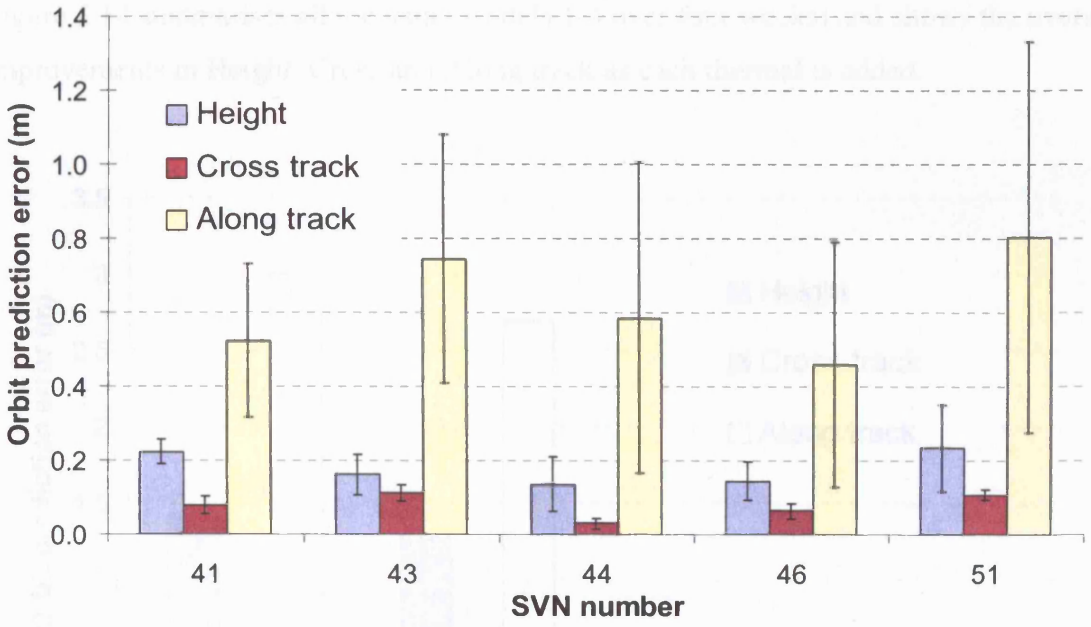

Figure 5.12: Full thermal model – Model 4

Figure 5.13 shows orbit prediction results with and without the penumbra flux model.

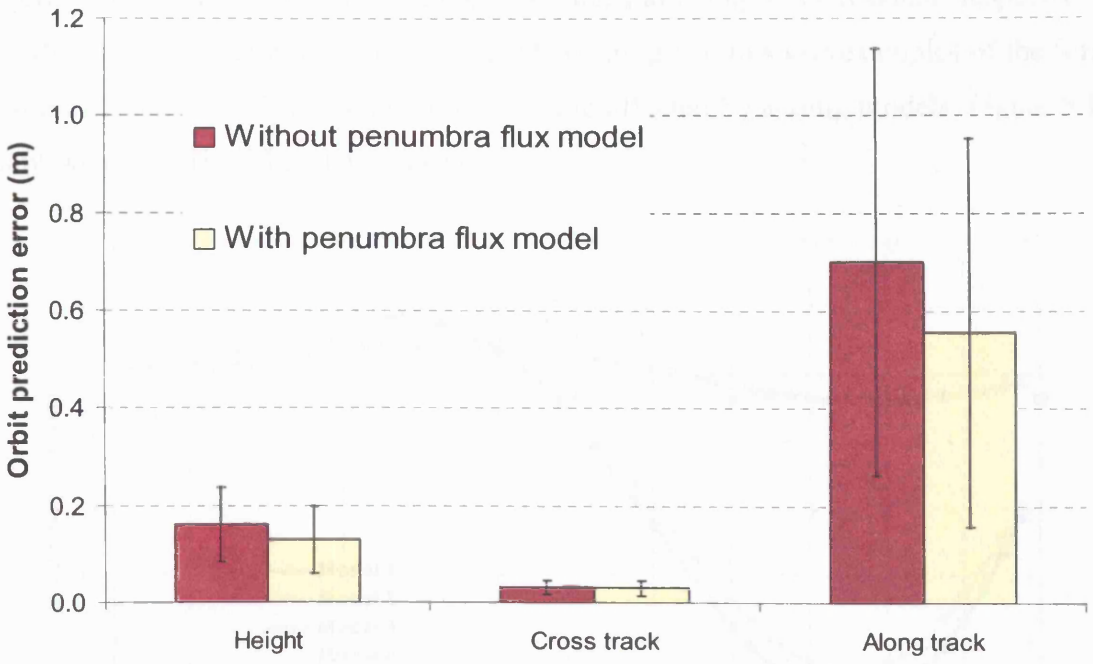

Figure 5.13: With and without penumbra flux modelling

Figure 5.14 summarises all the data (Models 1-4 over four weeks) and shows the overall improvements in Height, Cross and Along track as each thermal is added.

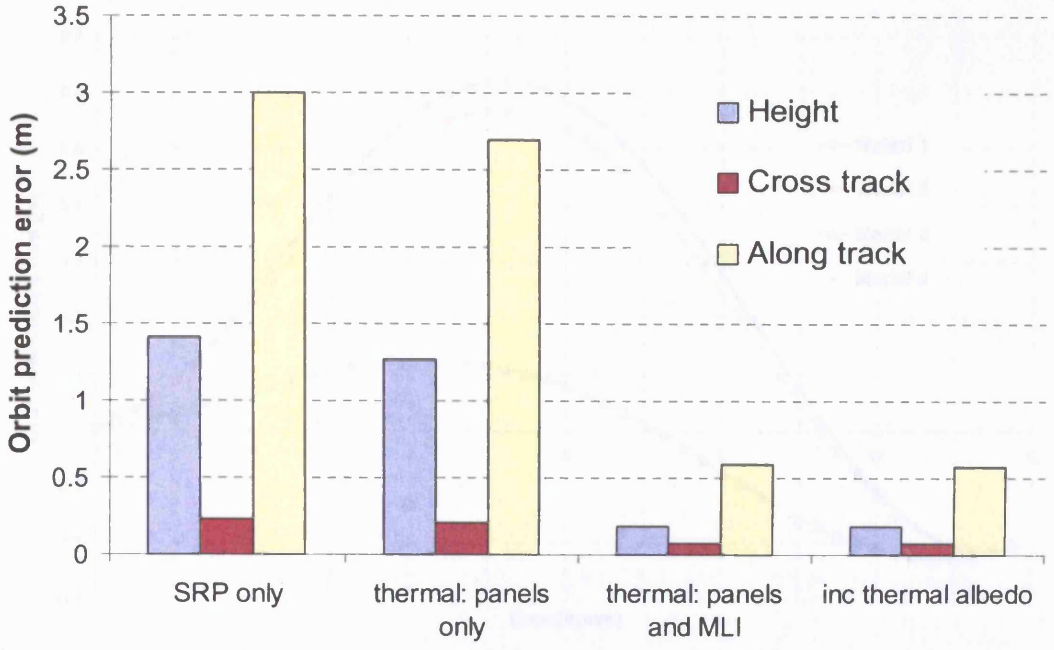

Figure 5.14: Summary of HCL results

Figures 5.15 - 5.17 show the Height, Cross track and Along track residuals respectively for Models 1 - 4 over one 12 hour orbit. These are given to show examples of the form of these errors over 12 hours, and how they are affected by adding models. Figure 5.18 shows an example of final HCL residuals.

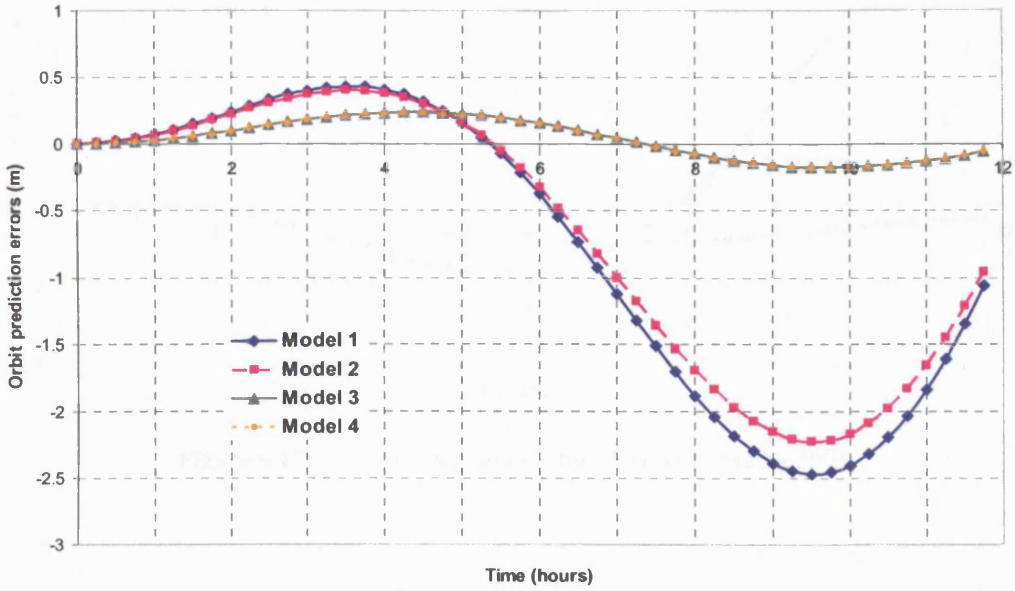

Figure 5.15: Height residuals for SVN 43, 3 March 2004

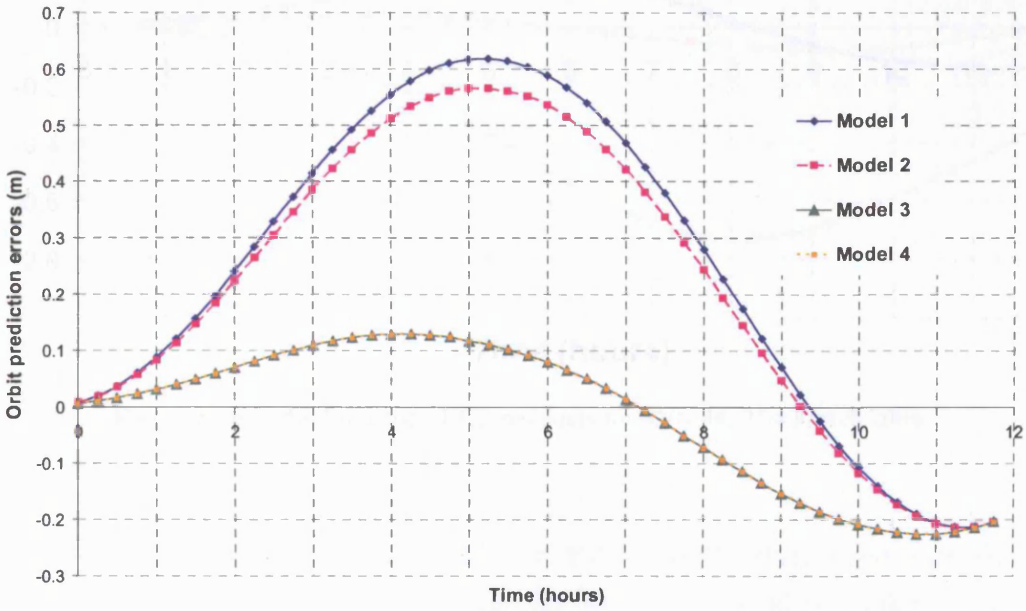

Figure 5.16: Cross track residuals for SVN 43, 3 March 2004

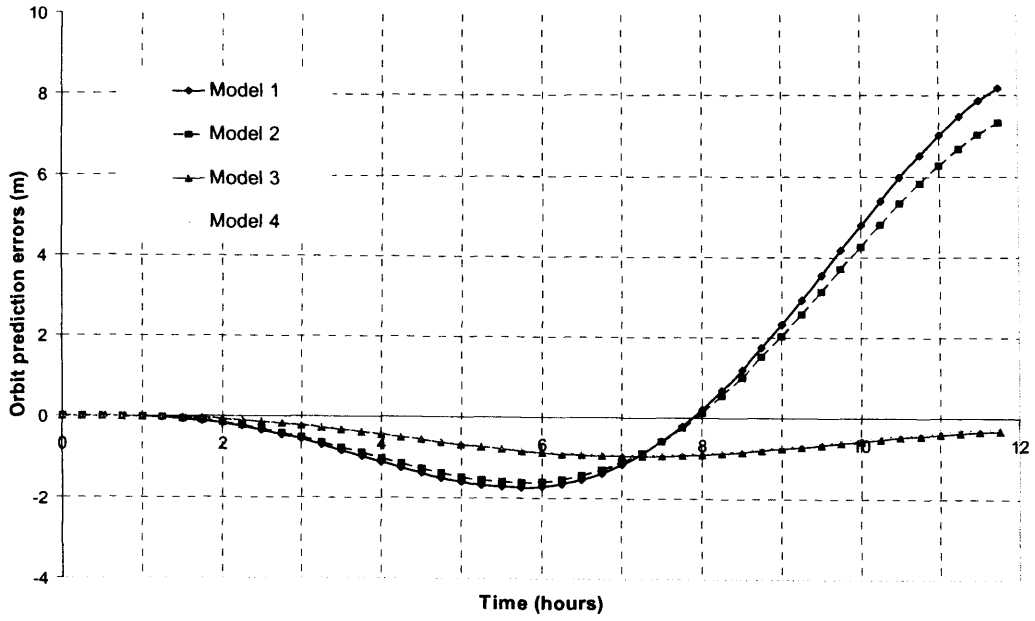

Figure 5.17: Along track residuals for SVN 43, 3 March 2004

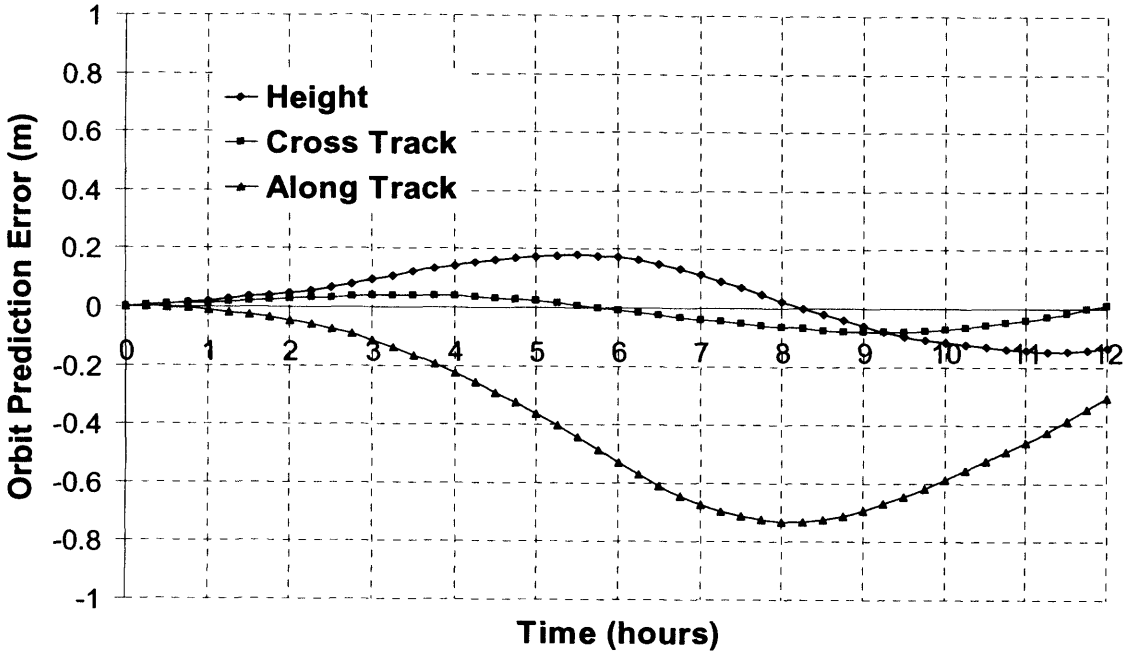

Figure 5.18: Orbit Prediction HCL residuals for SVN 44, 21st March 2004

5.6 Analysis and interpretation of results

5.6.1 Testing method 1: Comparison with telemetry

Figure 5.7 clearly shows the difference in temperature between aphelion and perihelion for both the telemetered temperatures and the modelled temperatures. In general the telemetered temperatures are much higher than the modelled temperatures. These discrepancies are analysed in Section 7.1.3 when the issue of power draw is discussed.

For SVN 43, the temperatures are higher than those predicted by the model by about 3K, but the temperature differences between aphelion and perihelion are much closer. Data telemetered from the other Block IIR satellites show this offset also. The forces derived from the telemetered data are higher than those modelled by ~12%, resulting in an acceleration error of ~1 x 10^{-10} ms^{-2}. This amounts to a maximum along track error of ~2 cm over 12 hours.

5.6.2 Testing method 2: Comparisons with other methods

The solar panel temperatures obtained through ESATAN which uses a finite element method give very good agreement with the model temperatures; the results are the same to within 0.02K. This provides some validation of the modelling technique used here. Vigue (1994) carried out a calculation based on the finite element method for GPS Block IIA panels, which were different to the Block IIR panels. Using these models, the same temperatures were produced. Fliegel (1996) calculated GPS Block IIR panel temperatures based on the same data set though details of his methods were not explicitly given. Again, the same temperatures were produced with these models.

5.6.3 Testing method 3: Orbit prediction

The improvements in orbit prediction using the thermal models are clear. Tables 5.7, 5.8 and 5.9 show how the average RMS along track error for a 12 hour orbit drops from 2.997m to 2.691m to 0.586m as first the solar panel thermal model is added, then the MLI model is added. The MLI is by far the largest contributor to the overall force. Figures 5.15, 5.16 and 5.17 show an example of how this error is consistently decreased over a 12 hour orbit in all three axes. Inclusion of the penumbra flux model also yields

significant improvements with the average along-tack acceleration over 28 orbits for SVN 44 dropping from 0.70m to 0.56m (shown in Figure 5.13).

Figure 5.18 shows an example of the HCL orbit residuals over 12 hours. These are much smaller than previously attained using purely analytical models. By way of comparison orbit prediction errors published in Fliegel (1996) were estimated to be at the 3-4m level over a similar arc length. These results are analysed further in Chapter 7.

Summary

This chapter presents an overview of the GPS system. The attitude, power draw, structure and surface properties of the GPS Block IIR spacecraft are specified and model computation is described. The main tests of the complete model were the comparison of numerically integrated predicted orbits with precise orbits. Four weeks worth of 12 hour orbits were predicted and residuals with respect to the precise orbit were calculated. Results showed that the addition of each successive model reduced the size of the residuals and that the largest impact was due to the modelling of the MLI. These results are analysed and discussed in more detail in Chapter 7 and 8. In Chapter 6, the methods are implemented for Jason-1 and tested in orbit determination.

Chapter 6 Jason-1

Chapter outline

This chapter provides a brief overview of the objectives of the Jason-1 mission. The spacecraft structure is described and the data used in the modelling process are given. The implementation of this data is outlined for the SRP and TRR models of the spacecraft bus and panels. Testing methods are explained and the results of these tests are shown. This is followed by a brief analysis and discussion of the results. A more detailed analysis of the results will follow in Chapter 7.

6.1 Mission overview

Jason-1 is an ocean altimetry satellite developed jointly by the French Space Agency, CNES, and NASA. It was launched into a near circular orbit, with an inclination of 66° and approximate altitude of 1335 km in December 2001. It has an orbit period of 112 minutes and a ground track repeat period of approximately 10 days. Jason-1 follows on from the TOPEX/Poseidon mission launched in 1992 (Fu, I. & Cazenave, A., 2000) and its main roles are to monitor global ocean circulation, study interactions of the oceans and atmosphere, improve climate predictions and observe events such as El Nino.

Jason-1 uses a radar altimeter instrument to measure ranges to the sea surface. The altimeter is a nadir-pointing instrument, which emits microwave signals. The time delay between the transmission of this signal and the reception of the reflected signal from the surface is measured and signal time-of-flight calculations are carried out to solve for the range between the spacecraft and surface. Figure 6.1 shows the Jason-1 measurement system.

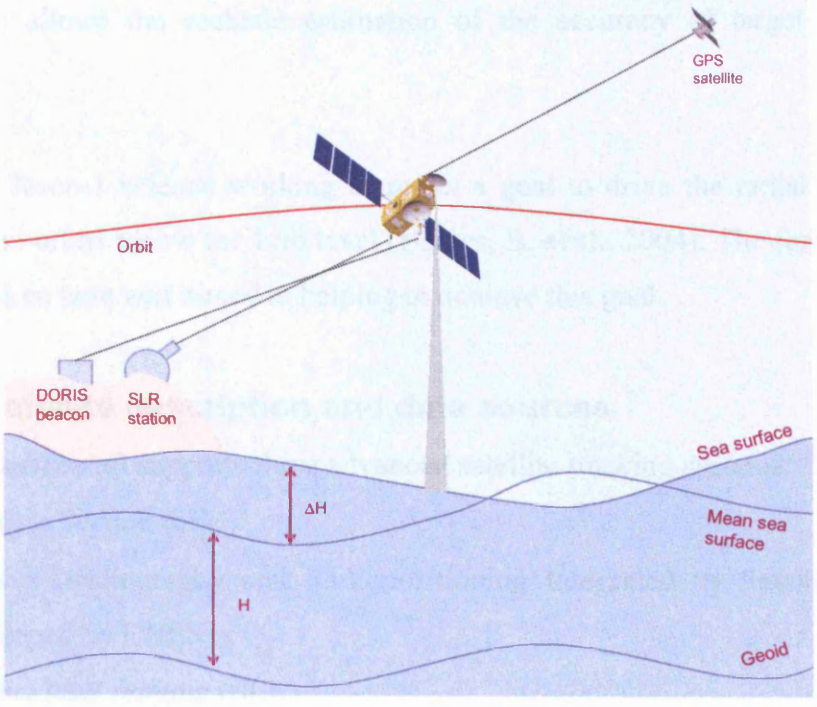

Figure 6.1: Jason-1 measurement system

The height of mean sea-surface above the geoid[11] is known as sea surface topography (SST), labelled H in Figure 6.1. It is caused by the quasi-stationary part of the dynamic topography which refers to large scale mean circulation in the oceans (caused by the earth's rotation, regional differences atmospheric pressure and salinity etc.). The instantaneous sea surface differs from the mean sea surface, by ΔH, and this is due to a time-variant component of the dynamic topography, caused by ocean tides, variations in local atmospheric pressures (the inverse barometric effect) and other smaller scale dynamic features such as ocean eddies. Depending on the desired quantity to be inferred form the altimetry measurements (e.g. H or ΔH), different models are required; these may be related to aspects of the stationary and time varying topography, the geoid or atmospheric influences which affect the measured range. The spacecraft position at the measurement epoch is also required and this is determined from the estimated orbit of Jason-1. Orbital errors are a source of systematic error in the determination of mean sea-surface heights and the accuracy with which they can be determined depends in part on

[11] Geoid models are estimates of the equi-potential surface which coincides with where the sea-surface level would be in the absence of all wind, circulation and tides.

the quality of the estimated orbits (Scharroo, R., 2002). The ability to quantify the errors in the orbits allows the realistic estimation of the accuracy of target geophysical parameters.

In 2002, the Jason-1 science working team set a goal to drive the radial precision of post-processed orbits below the 1cm level (Haines, B. et al., 2004). The force modelling work undertaken here was aimed at helping to achieve this goal.

6.2 Satellite description and data sources

The Jason-1 spacecraft supports three advanced satellite tracking systems:

- GPS (see Section 6.1)
- Doppler Orbitography and Radiopositioning Integrated by Satellite (DORIS) (developed by CNES)
- Satellite laser ranging (SLR)

  Data from these systems can be used separately or in combination to calculate the orbit of Jason-1.

Jason-1 is constructed around a central bus measuring approximately 0.96m x 0.96m x 2.25m. Power is supplied by solar panels arrays attached to the ± Y faces of the spacecraft; each array consists of four panels, each 1.49m x 0.8m. These arrays rotate about yokes aligned parallel to the spacecraft Y-axis and the +Y and –Y panel arrays can be steered by the solar array drive mechanism (SADM) independently of each other (see Figure 6.2).

The science payload is clustered around the upper half of the bus. These instruments include the Jason Microwave Radiometer (JMR), two turbo-rogue GPS Space receivers (TSRs), a laser retro-reflector array (LRA), a dual frequency DORIS antenna and the satellite altimeter dish and associated structures. Apart from the surfaces of the JMR, altimeter dishes and a number of thermal control radiators, the majority of the bus is covered in multilayer insulation. A pair of star sensors is mounted on the –Z face of the bus.

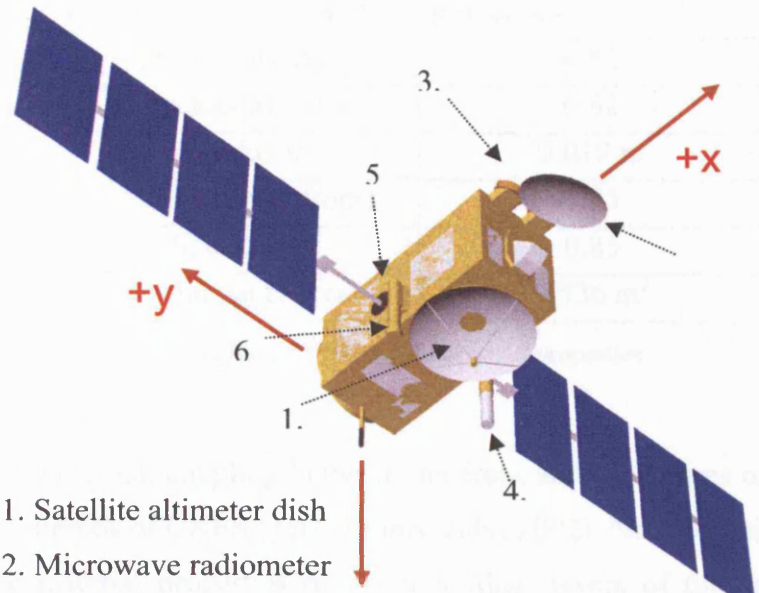

1. Satellite altimeter dish
2. Microwave radiometer
3. Turbo-rogue receivers
4. Doris antenna
5. SADM
6. Retro-reflector array

Figure 6.2: Geometrical form of Jason-1 used in this study

The spacecraft geometry was extracted from an ESABASE[12] file supplied by the spacecraft manufacturers ALCATEL. This data was used to create the computer simulation of Jason-1 in the same way as for GPS Block IIR described in Section 5.2. In total 114 interlocking components were used for the simulation.

6.2.1 Spacecraft material and optical properties

Surface material properties of the MLI and solar panels were also obtained from ESABASE files and are given in Table 6.1 and 6.2 below.

MLI properties	
Emissivity	0.77
Absorptivity	0.35
Specularity	0.5

Table 6.1: Properties of Jason-1 MLI

[12] ESABASE is an engineering tool supporting the harmonisation/standardisation of spacecraft analysis used by the European Space Agency

Solar panel properties	
Front emissivity	0.82
Back emissivity	0.82
Thickness	0.018 m
Absorptivity (front)	0.75
Specularity	0.85
Total panel area	9.536 m^2

Table 6.2: Jason-1 solar panel properties

A value for the thermal coupling between the front and back faces of 61 $WK^{-1}m^{-2}$ was supplied by J. Perbos of CNES (pers comms, July, 2002). No information was available regarding the material properties of the individual layers of the panel. The thermal coupling parameter describes the effective conductivity per unit length through the panel.

The power draw regime for the JASON panels was also provided by J. Perbos and is as follows:

> "The power draw from the panels depends on whether the power sections located on the panels are On or Off. The nearest panel with respect to the spacecraft body is always On as well as one fourth of the surface of the furthest panel from the body. The other power sections may be On or Off depending on the power needs along the orbit. When the power section is On, the power draw is typically 150 Wm^{-2} (the cells efficiency is 12%)."

This information is not specific enough to define accurately the power draw at any time. If it is assumed that the power draw from the inner and quarter of the outer panels is distributed over all the panels, a simple calculation yields a minimum power draw of 47 Wm^{-2}. This assumption will result in some inaccuracies; their magnitudes and implications are discussed in Chapter 7.

6.2.2 Attitude laws

Jason-1 has various attitude modes, although the majority of the time it is either in a sinusoidal or fixed yaw mode. The transition between these modes should occur at well defined times. The spacecraft attitude can be predicted from attitude control laws, or determined retrospectively from telemetered attitude quaternions and a set of SADM rotation angles[13]. This information is used to calculate the rotations that transform a vector in ECI coordinates to BFS coordinates, thus defining the attitude of the spacecraft bus and the pointing direction of the panels. In contrast to the case of GPS satellites (Section 6.2.1), the sun is not constrained to the body fixed XZ plane of the satellite, and can be tilted out of the plane by up to 15° on either side as shown in Figure 6.3.

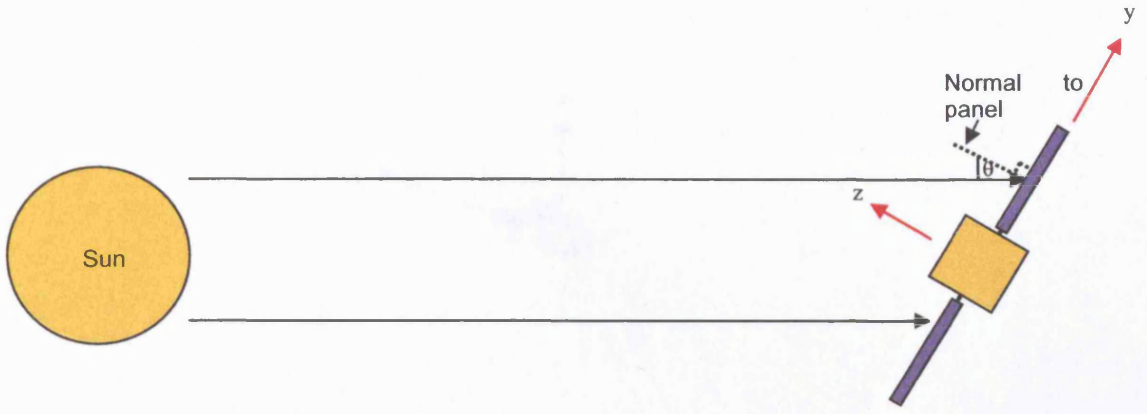

Figure 6.3: Possible attitude of Jason-1

6.3 Model computation

For Jason-1, only SRP and TRR models were tested. This was because of the nature of the testing, which was to be carried out by JPL in their orbit determination software GIPSY-OASIS II.

6.3.1 Spacecraft bus model

To compute the SRP and TRR forces due to the parts of the spacecraft bus, the pixel array method described in Section 4.7.1 was used. The SRP model accounts for the effects due to all surfaces. The TRR model only evaluates the response of parts of the spacecraft covered in MLI. The reasons for this and its implications are discussed in

[13] These can be obtained by via ftp from ftp://spike.csyt.cnes.fr/pub/POD/

Chapter 7. To account for accelerations due to all possible sun-facing spacecraft profiles, the Jason-1 bus model requires a 3D surface of accelerations (as opposed to the GPS 2-D case). To create this surface the pixel array was rotated all the way around the spacecraft in the BFS X-Z plane, sampling the bus accelerations at intervals of 10°. The pixel array was then tilted out of the XZ plane by 2.5° and again rotated 360° at 10° intervals in this plane. This "out of plane" modelling was carried out at 2.5° intervals up to 17.5° out of the X-Z plane to either side. This resulted in 15 x 36 data points (15 planes, 36 within each plane) where each data point represents the position of the sun with respect to the spacecraft (See Figure 6.4).

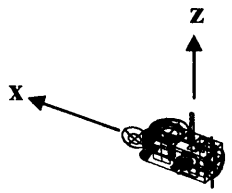

Figure 6.4: Directions from which the pixel array was projected

The commercial 3D surface mapping tool Surfer[14] is used to covert this data into 3 rectangularised grid files (one for each axis in the BFS basis) at 2.5° spacing in latitude and longitude of accelerations over a sphere centred on the spacecraft. A latitude and longitude of 0° coincides with the BFS X-axis, and a latitude of 90° coincides with the BFS Z-axis. The grid represents the accelerations due to SRP and TRR of the spacecraft bus at 1 AU with an assumed spacecraft mass of 489.1 kg (ESABASE file). Bilinear

[14] This software can be obtained from http://www.goldensoftware.com/products/surfer/surfer.shtml

interpolation between these grid points is used to calculate accelerations for any required latitude and longitude of the sun.

To demonstrate the magnitude of the thermal effect of the MLI surfaces, Figure 6.5 shows accelerations as a function of EPS angle (with the sun is confined to the XZ plane). The main contrast between Jason-1 and GPS Block IIR (Figure 5.5) MLI accelerations is in the relative sizes of the Z and X accelerations; the Z accelerations are larger in the Jason-1 case due to the higher surface area of the Z face relative to the X face.

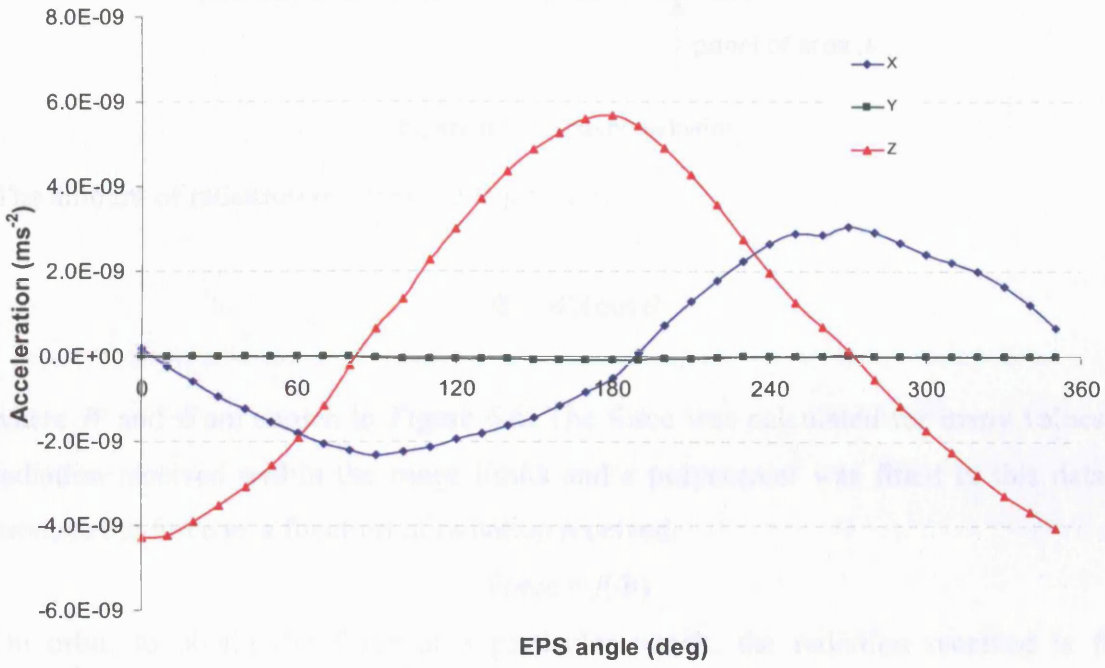

Figure 6.5: BFS X, Y and Z accelerations as a function of EPS angle due to MLI surfaces

6.3.2 Solar panels

The technique developed in Section 4.2.2 was applied for the calculation of force due to TRR of Jason-1's solar panels.

The thermal coupling parameter is equivalent to K_{eff}/L which is equal to $1/R_{total}$. In Equation 4.1.7, R_{total} was assigned the value of $1/61 = 0.016393$ KW^{-1}.

The TRR force due to the panels depends on the amount of radiation received, which in turn depends on the radiation flux in the vicinity of the spacecraft and the angle between the panel normal and (negative) direction of incoming radiation.

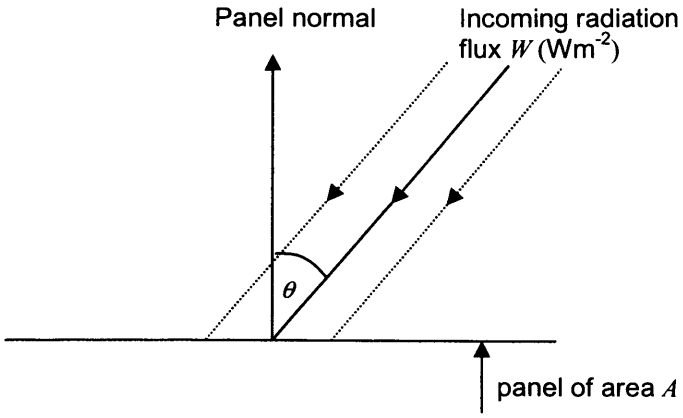

Figure 6.6: Incoming radiation

The amount of radiation received, Φ is given by:

$$\Phi = WA\cos\theta$$

where W and θ are shown in Figure 6.6. The force was calculated for many values of radiation received within the range limits and a polynomial was fitted to this data to produce the force as a function of radiation received.

$$\text{Force} = f(\Phi)$$

On orbit, to obtain the force at a particular epoch, the radiation received is first calculated from W and θ, and then the force equation is used to return the force perpendicular to the panels. The equation for the force F normal to the front face of the solar panel is:

$$F = -3.54 \times 10^{-13}\Phi^2 - 3.06 \times 10^{-10}\Phi + 1.11 \times 10^{-7}\ \text{N}$$

where the force vector is in the direction of the front face panel normal (see Figure 6.7).

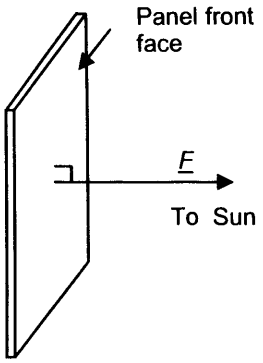

Figure 6.7: Direction of force vector

Values of temperatures and accelerations obtained at a sun-satellite distance of 1AU, a spacecraft mass of 489.1 kg and an angle of incidence of 0° are:

$T_f = 324.06K$

$T_b = 316.47K$

Acceleration = 2.005×10^{-9} ms^{-2}.

6.4 Testing methodology

The incorporation of positioning systems such as GPS in low earth orbiting spacecraft provides precise methods for the determination of satellite position and velocity. Testing of models for Jason-1 was based on incorporation of the SRP and TRR thermal models into GIPSY-OASIS II, JPL's orbit analysis tool. Though SRP and TRR modelling are grouped together, and their effects cannot be judged separately, the thermal accelerations constituted circa 15% of the magnitude of the SRP force on the body, and circa 5% of the panels. This is a substantial proportion so significant errors in thermal models would result in poor results overall.

The strength of the overall model was judged on comparison of orbit determination results using the CNES SRP and TRR models which were in place in GIPSY-OASIS II for routine orbit determination of Jason-1 at the time. The CNES model makes use of the same ESABASE data as was used in the UCL model. CNES used the data to compute a micro-model for the spacecraft central body. Simplifications were made in the geometries of some parts, eg the parabolic dish of the radiometer was treated as a cylinder and other curved surfaces such as the altimeter dish were made of tessellated triangular surfaces. Accelerations due to solar radiation were computed for all possible

incoming light directions using this model. A simplified 6-face box model was then optimally adjusted to reproduce these accelerations as accurately as possible. The optical properties and component areas which they represented were then estimated in a least squares sense to generate the same response of the spacecraft. The assumption inherent in this approach is that the empirically estimated parameters will soak up all the mis-modelled effects, which are inevitable due to the box and wing simplification (Ferrier, C. et al., 2002).

6.4.1 Orbit determination

A conceptual overview of the orbit determination (OD) process is presented here; for more detail the reader is referred to Tapley et al. (2004).

The goal in orbit estimation is to determine the satellite orbit that best fits a set of tracking data, whilst at the same time satisfying a set of differential equations specifying the system dynamics. Tracking data or "observation" data include any observable quantities that are a function of the position and/or velocity of a satellite at a point in time. These include range, range rate, azimuth and elevation from ground stations of known location, or ranges from other satellites such as GPS range observations. In the testing of the force models carried out here for Jason-1 orbits, only GPS observables are used as tracking data.

The GPS observations would represent the true state of the spacecraft if there were no noise or biases in the measurement systems and all factors affecting the measurements, such as signal delays due to atmospheric water vapour, were perfectly modelled. As this is never the case, there is always some discrepancy between the observations and the real state of the satellite. The aim in OD is to best estimate the parameters which influence observations, so that these parameters can then be used to re-produce an orbit which best fits the tracking data. Theoretically, any parameter which influences the tracking data either directly or indirectly can be estimated. Such parameters include satellite positions and velocities, tracking data biases, atmospheric drag parameters, solar radiation pressure parameters, and coefficients of the Earth's gravitational field. Once the parameters have been estimated, they are used to compute a set of measurements which are intended to reproduce the observations – C_i.

To compute C_i, an estimate of an initial state vector[15] is made. Integration of the orbit using the dynamic models (e.g. gravity field models, non-conservative force models), and application of measurement models (e.g. models of system noise) and models of the environmental factors affecting the measurements, are used to model the observations at the next measurement epoch. The model parameters are adjusted to minimise the residuals between the observed and computed observations using the observation equiation:

$$[A_i][x_i]=[b_i]$$

where x_i is a vector containing corrections to the initial estimates for the parameters used to compute the observations, A_i is the design matrix; it contains the partial differentials of the observations with respect to the model parameters and b_i is a vector containing the observed minus computed measurements $[O_i - C_i]$ (these are the computed residuals). When the model parameters have been optimised, the resulting spacecraft trajectory should be consistent with the physics of the mathematical model and the series of observations that are used to constrain the orbit. Figure 6.8 is a flow chart of the process.

[15] state vector here refers to the complete set of parameters that will be estimated

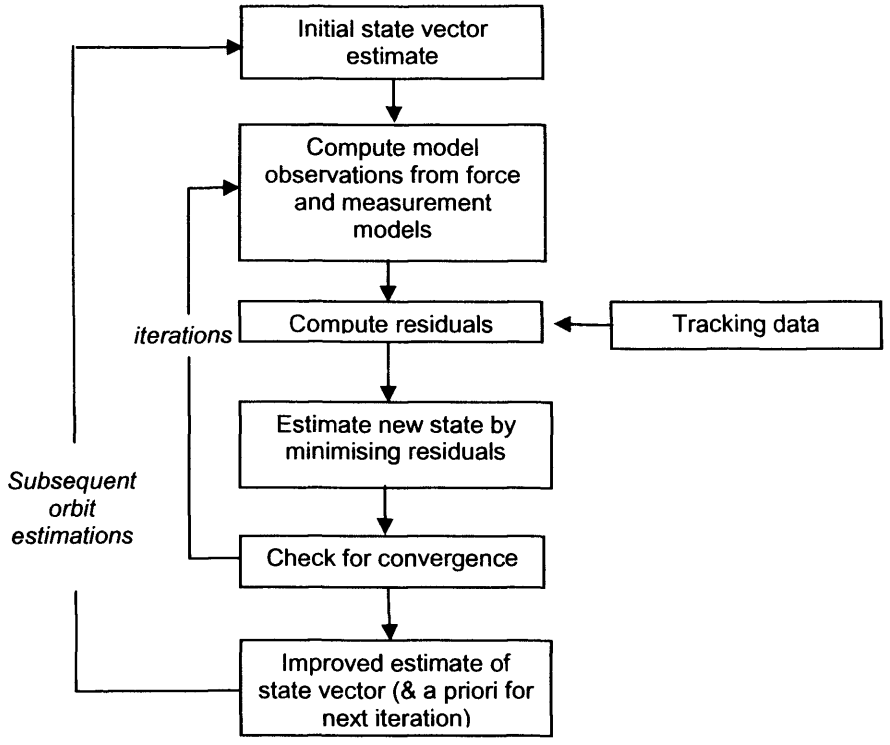

Figure 6.8: Flow chart of orbit determination process

It is critical for a successful estimation that the observations are well modelled, as poor models may result in large residuals which cannot be sufficiently minimised. The orbit determination software used here was GIPSY-OASIS II. A comprehensive description of this software and its usage can be found in a manual by Gregorius (1996). Points to note are that this software uses a sequential filter algorithm called a square root information filter (SRIF). SRIF is described in this manual as "a multi-satellite-batch-sequential-pseudo-epoch-state-process-noise-filter". It is, more basically, a modified Kalman filter. A Kalman filter is a least-squares process which uses the state vector from a previous epoch as the starting point for the next epoch. This avoids the need to invert large matrices by inverting lots of small matrices that are created sequentially for each time interval or "batch". SRIF differs from a Kalman filter in that it makes use of the square root of the covariance matrix, which is done to ensure a more numerically stable system of equations.

Within statistical orbit estimation, there are three different approaches for solving for the precise orbit, namely the dynamic, reduced dynamic and kinematic approaches. These are described below.

6.4.1.1 Dynamic strategy

In a dynamic orbit computation, the trajectory of a spacecraft is evaluated based on the a priori force model. This method is used when limited tracking data is available. Errors in the force model can be corrected for if some tracking data exists, through the estimation of a limited number of scale factors and once per revolution empirical terms. Analysis of the measurement residuals may tell us which element of the model is in error. This method is useful when models of the forces are required as end-products, for example in gravity field measurement satellites such as GRACE.

6.4.1.2 Reduced dynamic strategy

In this case a more accurate orbit can be computed by a greater emphasis on the observations than on the force model. This technique relies on the availability of large amounts of tracking data which are required to solve for the extended state vector which includes empirical accelerations to account for the errors in the force model.

6.4.1.3 Kinematic strategy

The kinematic strategy dispenses entirely with precise models of the forces underlying the satellite motion, relying instead on the geometric diversity, continuity, and precision of the GPS tracking measurements. Svehla and Rothacher (2003) have demonstrated orbit accuracies of 1–3 cm for the gravity gradiometry mission CHAMP using a purely kinematic (geometrical) approach to precise orbit determination. The kinematic approach, however, is highly sensitive to aberrations in the GPS viewing geometry. If the receiver loses lock or resets, which happens at least once per orbit (Haines, B. et al., 2002), there are no orbit solutions spanning the gap till lock is regained.

6.5 Testing methods: Comparison of orbit quality

Testing of the SRP and TRR models was carried out by the Earth Orbiter and Radiometric Systems Group at JPL using GIPSY-OASIS II. Generally smaller residuals imply more precise orbits. This does not necessarily mean more accurate orbits though,

as possible systematic errors in the tracking data could cause systematic errors in the orbit solution, without significantly affecting the residuals. Instead, the examination of a combination of parameters are carried out to infer orbit quality. The testing methods employed by JPL are discussed in Sections 6.5.1-6.5.5.

6.5.1 Solar scale

For testing purposes only, an empirical scale factor for solar radiation is estimated in the adjustment process. The solar scale gives an indication of how well the SRP force models reflect the truth on average. A large or small value of the solar scale (i.e. $<<1$ or $>>1$) would imply substantial errors in the a priori model, whereas a value close to 1 would indicate that the model might be correct, or at the least, it cannot be improved simply by a scaling factor. A scale factor of 1 is not conclusive evidence that the "form" of the force function is correct but it can be used alongside other tests to evaluate the accuracy of the a priori model.

6.5.2 Atmospheric drag coefficient

The coefficient of atmospheric drag is another parameter estimated in the OD process and the changes in its stability over time can be used alongside the solar scale as a metric of orbit quality. It is possible for aliasing to occur between the solar scale and this coefficient. Thus, when both solar scale and drag parameters are applied, the estimated atmospheric drag parameter could absorb errors in the solar radiation model, causing the solar scale to be close to 1. This would however cause the atmospheric drag coefficient to vary substantially in order to absorb these errors. Analysis of the solar scale and atmospheric drag coefficient parameters together is a useful method of model evaluation.

6.5.3 Orbit overlaps

The consistency of orbit solutions during the overlap periods is a good indicator of orbit precision i.e. internal consistency. Because of adjustments in the initial conditions of each arc, the final positions from the previous arc will generally not match the initial points of the next arc exactly, even though both are supposed to represent the satellite position at the same points in time. The consistency of the orbit solutions during overlap periods is an important, albeit potentially optimistic, indicator of the orbit quality and should be considered principally an indicator of orbit precision rather than accuracy.

6.5.4 Crossover residuals

At locations where ascending and descending tracks cross over oceans, the altimeter aboard Jason-1 is able to sample the sea-surface on the same location but at different epochs. These locations are generally known as crossovers. Crossover residuals refer to the differences between the mean sea surface heights measured at each epoch. These residuals can partly be attributed to an actual sea level change between the two epochs, and to reduce this, a limit is placed on the time difference between the epochs of measurement (e.g. < 10 days). Other causes could be errors in the applied altimetric range corrections, tide models or the computed orbit altitude (Scharroo, 2002). If the errors are temporally invariant, they will be removed in the differencing, but if these errors are different on different arcs, then they will show up in the crossover residuals. Greater precision is attributed to smaller difference in these heights and these can be explained by a more precise orbit. The crossover residuals provide no information on the absolute errors, but only on their relative values. Again, this technique is a test of the orbit model precision, not accuracy.

6.5.5 High elevation SLR biases

Laser-ranging observations of the Jason-1 satellite can be used to assess the accuracy of the GPS-based orbits independently. In this test, the satellite laser ranging (SLR) data are not allowed to influence the orbit solution. When the satellite flies almost vertically over an SLR station, the residuals between GPS derived orbits and laser orbits at that point are representative of the radial orbit error. Comparison of the residuals of a GPS derived orbit with the SLR ranges is a powerful test of orbit accuracy, since the SLR data is totally independent of the GPS data.

6.6 Results

Sections 6.6.1-6.6.3 show results of comparisons of solar scale, atmospheric drag coefficients and orbit overlap tests carried out by JPL. These were carried out on 90 days of dynamic orbits, estimated for Jason-1 using GIPSY-OASIS II, JPL's routine orbit determination software, using the UCL SRP and TRR model and the CNES model. Sections 6.6.4 and 6.6.5 give results of crossover residuals and SLR biases from two years of data.

6.6.1 Solar scale

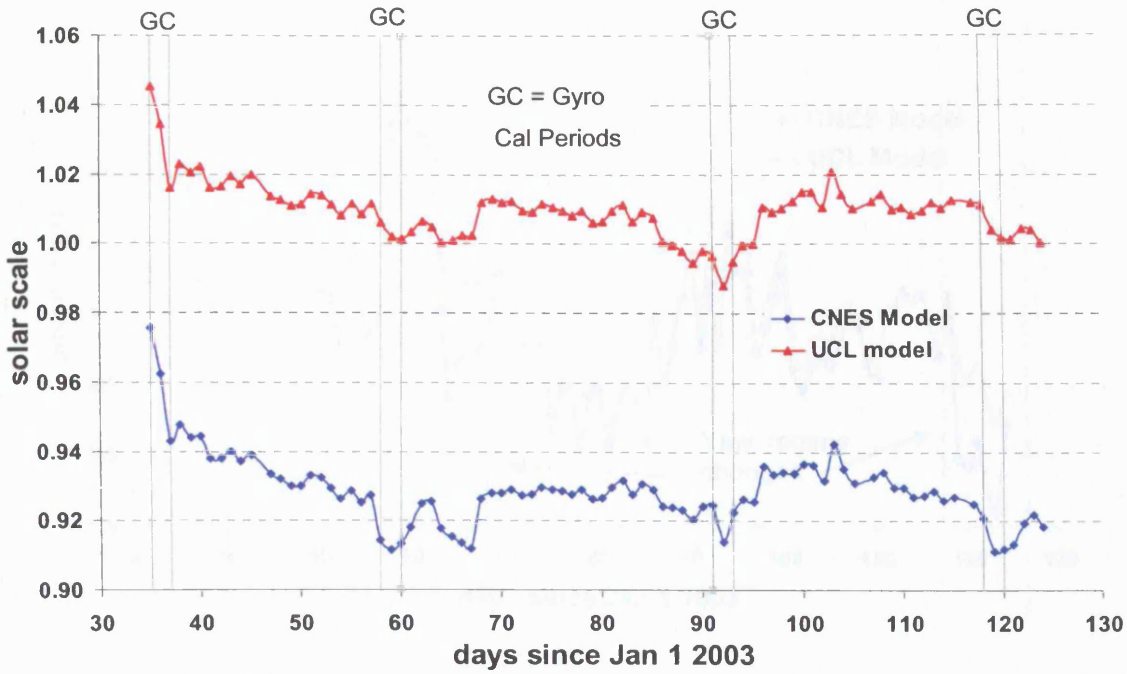

Figure 6.9: Solar scale

The four "gyro cal" periods refer to times when calibration of the gyro took place. During this time the spacecraft was spun rapidly, and the time resolution of the attitude quaternions would not be high enough to register these manoeuvres. During these times the value of the solar scale can be ignored. Table 6.3 shows the values and standard deviations of the solar scale. "Gyro cal" periods have been taken out.

	Mean solar scale	Standard deviation
UCL	1.009	0.0062
CNES	0.929	0.0074

Table 6.3: Jason-1 solar scale results

6.6.2 Atmospheric drag coefficient

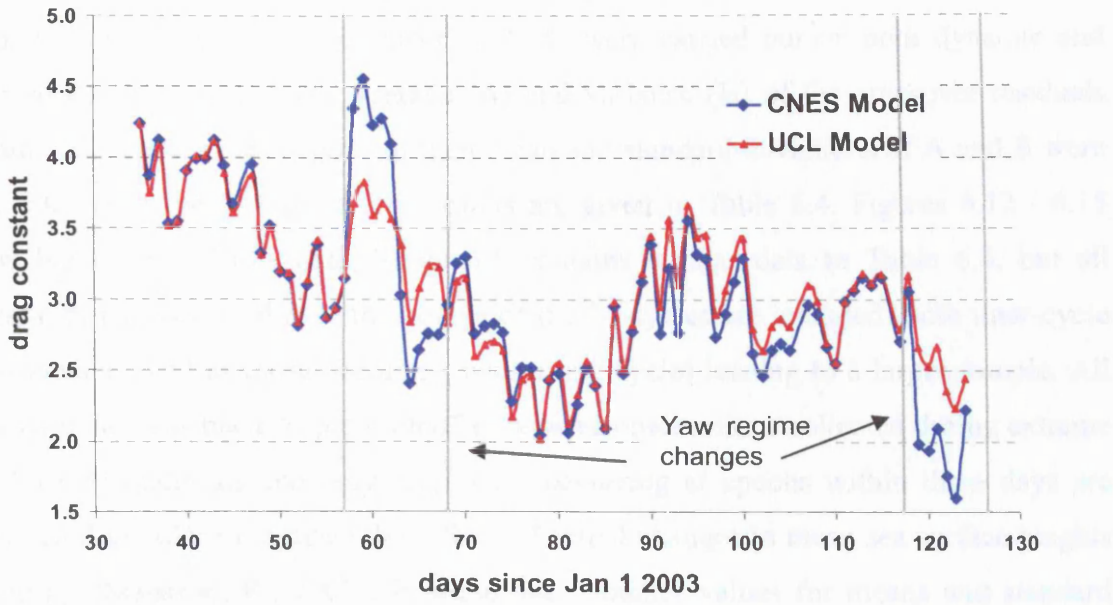

Figure 6.10: Linear interpolation of daily atmospheric drag coefficients

6.6.3 Orbit overlaps

Figure 6.11 shows difference in mm in orbit overlap residuals (UCL – CNES). A negative value implies better performance by the UCL model. The periods marked as yaw regime changes are valid and significant.

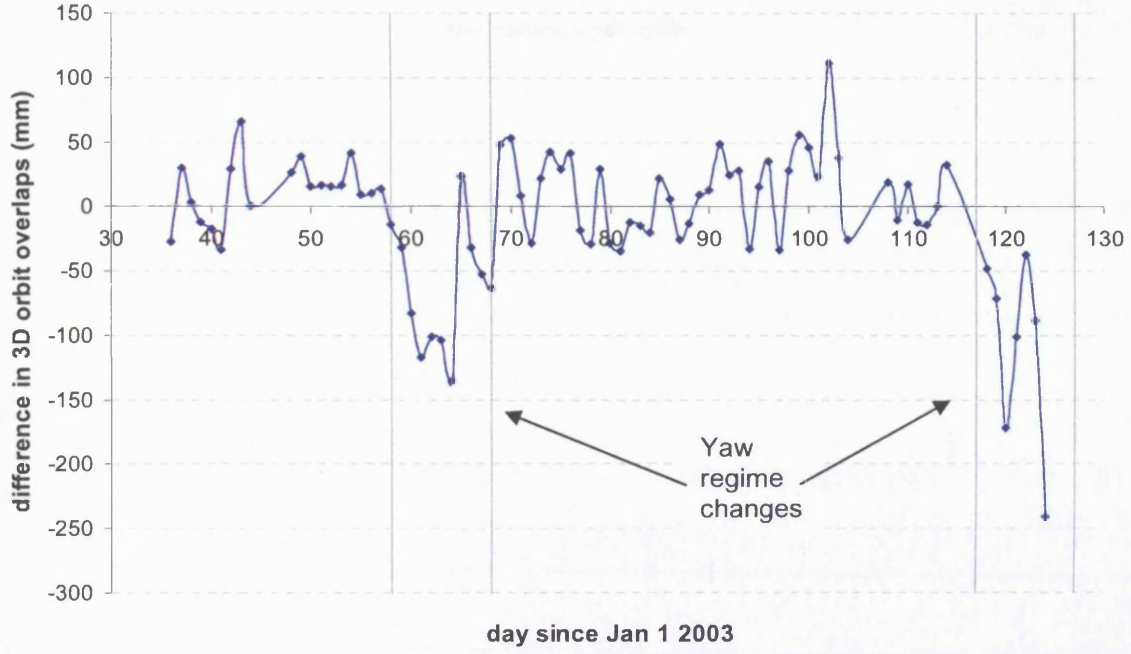

Figure 6.11: (UCL-CNES) orbit overlap residuals

6.6.4 Crossover residuals

In this comparison, data was taken from 74 cycles, where each cycle is one 10 day ground track repeat period for Jason-1. Tests were carried out on both dynamic and reduced dynamic orbits. The average (A) and variance (B) of the crossover residuals within each cycle were calculated; then mean and standard deviations of A and B were calculated *over* the 74 cycles. The results are given in Table 6.4. Figures 6.12 - 6.15 show bar charts of this data. Table 6.5 contains similar data to Table 6.4, but all crossovers that occurred over the course of the 74 cycles are included (both inter-cycle crossovers as well as those occurring within one cycle) leading to a larger sample. All crossover data has been "super-edited" to remove observations collected during extreme wind/wave conditions and only crossovers occurring at epochs within three days are considered in order to mitigate the effects of actual changes in mean sea surface heights occurring (Scharroo, R., 2002). In these data, smaller values for means and standard deviations indicate more consistent orbits.

	Mean A (mm)		Variances B (mm^2)	
	Average of A	Std. Dev of A	Average of B	Std. dev of B
CNES Model Dynamic	1.05	7.17	2263.13	395.87
UCL Model Dynamic	0.94	7.05	2254.35	375.20
CNES Model Reduced	0.90	5.39	2105.89	232.26
UCL Model Reduced	0.91	5.09	2104.06	230.74

Table 6.4: Crossover residuals for Jason-1: Average and standard deviation over all 74 cycles of mean and variance per cycle

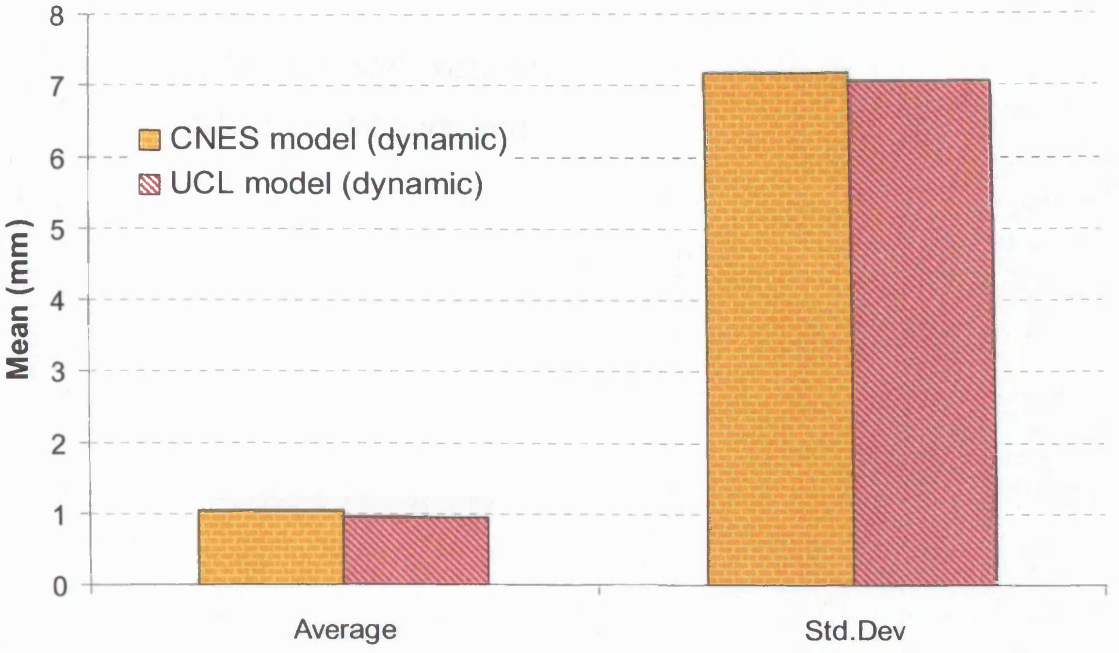

Figure 6.12: Mean crossovers over 74 cycles, dynamic orbits

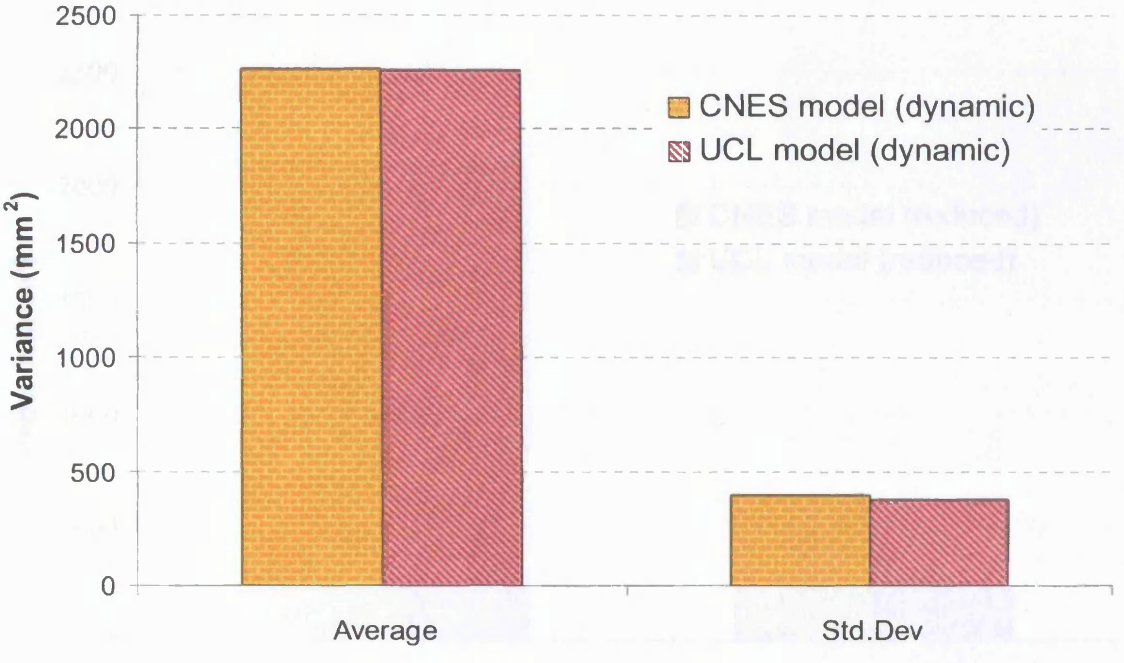

Figure 6.13: Variances over 74 cycles of crossovers, dynamic orbits

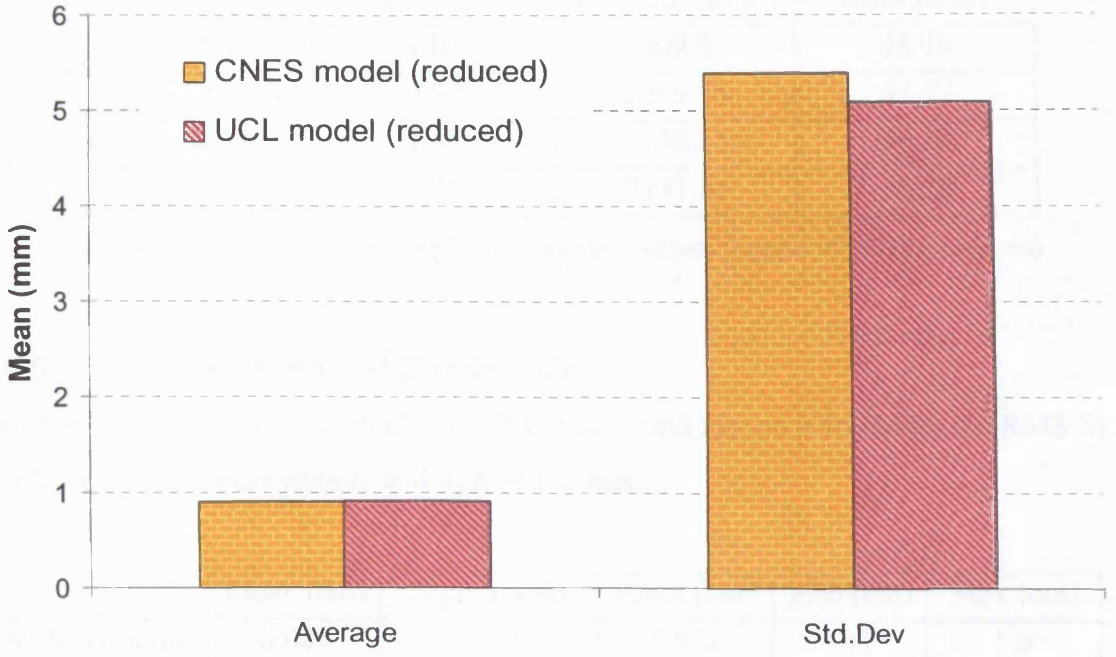

Figure 6.14: Mean crossovers over 74 cycles, reduced dynamic orbits

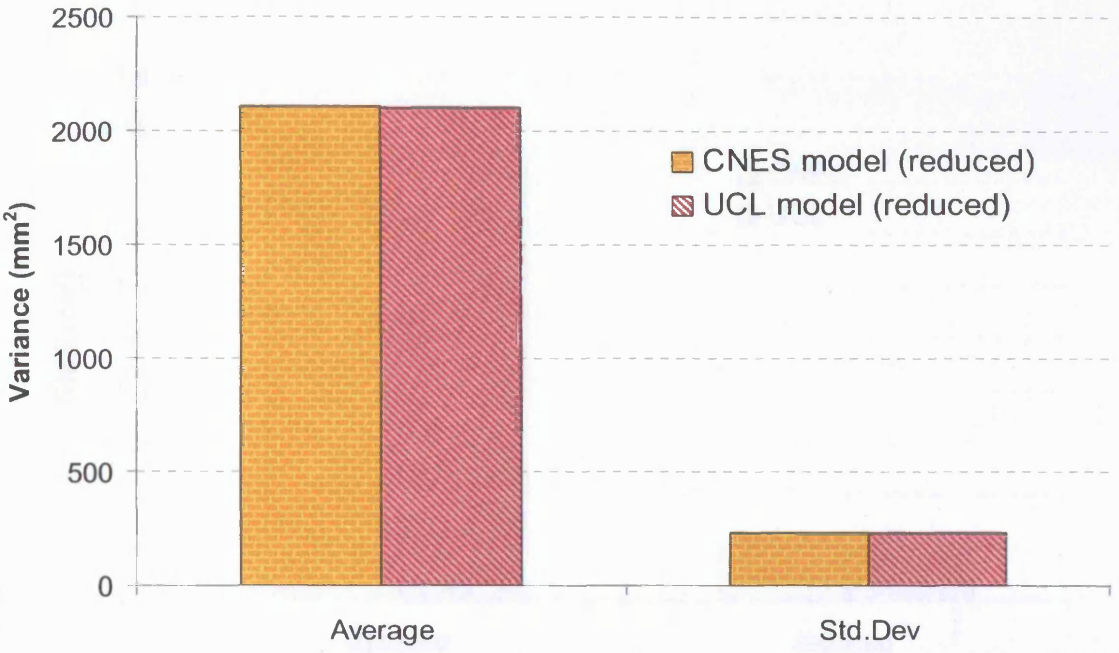

Figure 6.15: Variances over 74 cycles of crossovers, reduced dynamic orbits

	Mean (mm)	Variance (mm^2)	RMS (mm)
CNES Dynamic	1.03	2309.81	48.08
UCL Dynamic	0.97	2299.75	47.97
CNES Reduced	1.45	2136.15	46.23
UCL Reduced	1.46	2131.61	46.18

Table 6.5: Mean, variance and RMS of crossover residuals (sample of 39310 crossovers)

6.6.5 High elevation SLR residuals

Table 6.6 gives the SLR residuals over 1409 arcs, and Figure 6.16 shows the RMS SLR residuals for reduced-dynamic and dynamic orbits.

	Mean (cm)	Sigma (cm)	RMS (cm)	Min (cm)	Max (cm)
CNES Dynamic	0.081	1.54	1.541	-7.1	5.9
UCL Dynamic	0.074	1.531	1.532	-6.9	5.6
CNES Reduced	0.026	1.152	1.152	-4.3	4.4
UCL Reduced	0.027	1.148	1.148	-4.4	4.6

Table 6.6: High Elevation SLR Range Bias Residuals over 1409 arcs

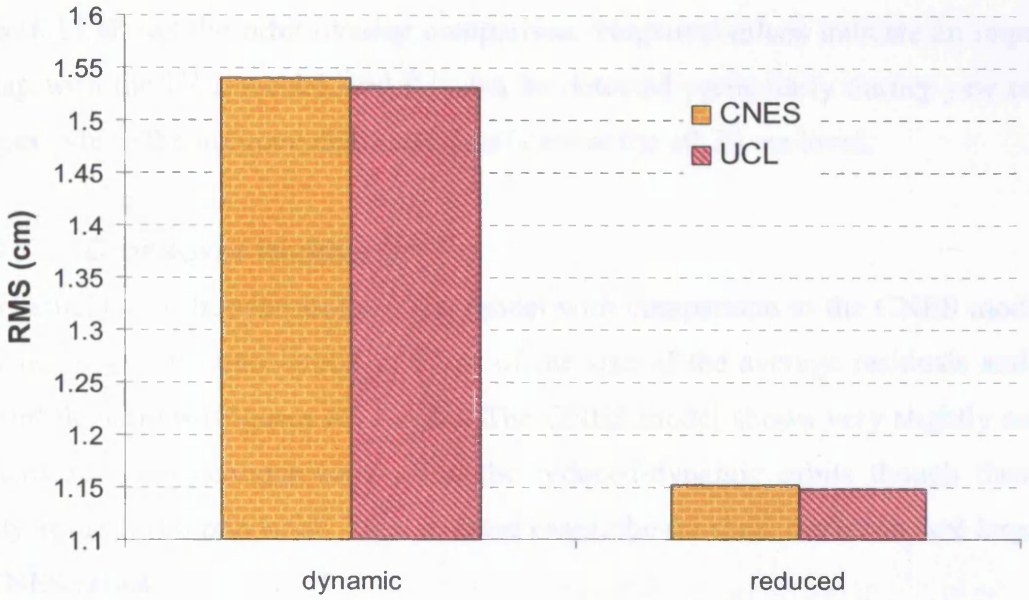

Figure 6.16: SLR RMS residuals for dynamic and reduced dynamic orbits

6.7 Discussion of results

6.7.1 Solar scale

Figure 6.9 shows that the estimated solar scale with the UCL SRP and TRR model is much closer to unity than the nominal model and the average scale factor is 1.01. The nominal model has a scale of 0.93. More importantly, the variation around the mean of the solar scale with the UCL models (as can be seen from the standard deviations) is smaller than with the nominal model and this implies better model fidelity. The periods marked as "gyro cal periods" can be ignored as there was likely to have been unmodelled attitude manoeuvres occurring at these times.

6.7.2 Atmospheric drag coefficients

Figure 6.10 shows the variation of the drag constant over the 90 day period. The variations are less with the UCL model than with the nominal model. This coefficient stability, combined with the solar scale parameter (average value of 1.01) shows that aliasing between the two parameters is reduced, which implied higher fidelity in the modelling.

6.7.3 Orbit overlaps

Figure 6.11 shows the orbit overlap comparison. Negative values indicate an improved overlap with the UCL model, and this can be detected particularly during yaw regime changes, where the improvements are significant at the 10-20 cm level.

6.7.4 Crossover residuals

Improvements can be seen in the UCL model with comparison to the CNES model for every test using dynamic orbits in terms of the size of the average residuals and their standard deviations (Figures 6.12-6.15). The CNES model shows very slightly smaller residuals for some comparisons using the reduced-dynamic orbits though these are mainly at the 1/100 mm level. Even in these cases, the standard deviations are larger for the CNES orbits.

As dynamic orbits rely more heavily on the force models than the reduced dynamic orbits, we expect the largest differences in these orbits.

UCL models improved crossover residual variances by ~10 mm^2 for the dynamic orbit case and ~5mm^2 in the reduced dynamic case. By comparison, the incorporation of GPS antenna phase centre variation maps improved cycle-averaged cross-over variances[16] by ~7mm^2 for Jason-1. This result was viewed as significant (Haines, B. et al., 2004).

6.7.5 SLR residuals

In these tests the UCL residuals and standard deviations are smaller than for the CNES models for the dynamic orbit. Though the residuals are slightly better for the CNES reduced dynamic models than UCLs, again the standard deviations are larger. It should be noted here that the absolute values are very small.

Summary

In this chapter an SRP model and a thermal model for Jason-1 were implemented into GIPSY-OASIS II. Various tests were carried out on dynamic and reduced dynamic orbits created using these models, and compared against the CNES models, which were the nominal models in use for Jason-1 orbit modelling at the time of testing. The tests compared values of solar scale, atmospheric drag, orbit overlaps, crossover residuals and satellite laser ranging residuals. In all dynamic orbit tests, and for almost all reduced dynamic orbit tests, the UCL model performs better than the CNES model. In Chapter 7, the results of thermal model testing for Jason-1 and GPS Block IIR will be analysed.

[16] This analysis was based on 62-10 day repeat cycles

Part IV

Chapter 7 Analysis

Chapter outline

In Part III, the models developed in this thesis are applied to the GPS Block IIR and Jason-1 satellites and results of orbit prediction and orbit determination tests are given. In this chapter, the errors associated with model parameters are discussed and their likely effects on the results are quantified. The effect of components which have not been taken into account is estimated. Orbit residuals obtained during model testing are analysed and remaining sources of error are identified and discussed.

7.1 Errors in model parameters

The accuracy of computed models depends directly on the uncertainties associated with the parameters used. Parameters required in the evaluation of the TRR force include solar irradiance, surface optical properties, solar panel material properties, spacecraft mass, spacecraft attitude and the amount of power drawn from the solar panels to the spacecraft bus.

The solar irradiance is known to vary over a number of periods. The high frequency component (X-rays and gamma rays) related to solar rotation represents only a tiny fraction of the total solar irradiance (TSI) and can be safely ignored. Over the solar cycle, which has periods of between nine and fourteen years, the TSI varies by up to only 1.4 Wm^{-2}. This represents a maximum change of 0.1% over the whole cycle. The variation could be crudely modelled but is unlikely to yield any great benefit over short arc analysis. Some gains may be realised over longer arcs.

Data relating to the properties of surface materials can be very difficult to acquire. This is most unhelpful given that these coefficients have a strong effect on computed models and subsequent orbit computations. Though optical properties of many materials are available in manuals, they are often given as crude values with large ranges.

A related problem is the gradual change in surface properties of a spacecraft due to space weathering. The principle environmental factors affecting surface properties are solar UV radiation; bombardment by monatomic oxygen; electron and proton radiation and micrometeoroids. Efforts have been made to examine the effects of these processes; the Long Duration Exposure Facility (LDEF) was launched in April 1984 and lasted for six years. On board were 57 experiments containing over 10000 specimens. The aims of the experiments were to test the effects of the low earth orbit space environment on materials, components and systems.

The general result of these experiments showed an increase in solar absorptivity of materials with little or no effect on infra-red emittance (Gilmore, D., 1994). White paints are affected strongly by UV radiation and protons and electrons and their absorptivities can degrade from 0.2 to 0.7 in just a few years. Kapton surfaces (used in MLI materials) also show substantial degradation and can turn almost black after several years in orbit. High absorptance surfaces, such as black paints, generally do not degrade. There may be however, a slight reduction in absorptivity over time due to UV bleaching. By contrast, quartz surfaces (such as front face solar panel surfaces) experience essentially no damage due to UV and charged particle environment, leaving contamination the only source of increased absorptivity. Contamination results when volatile condensable materials are out-gassed from spacecraft components, primarily electronic boxes, and then deposited onto external surfaces. This out-gassing is strongest early in the mission, followed by a small steady increase until the end of life.

The mass of a spacecraft changes over time as a result of small fuel burns applied to adjust the orbit of a satellite. Individual GPS spacecraft masses differ, and though variations are small, if they are not taken into account substantial orbit errors result. There will inevitably be some error in the pointing accuracy of individual spacecraft as well, causing the actual forces on each spacecraft to deviate from their modelled directions. The amount of power drawn from the solar panels affects surface temperatures and hence the TRR force. It has proved difficult to get reliable information regarding power draw and how it changes with time. No information was available for power draw regimes in penumbral regions, or how the regimes are affected as the efficiency of the solar cells decrease over time.

Sections 7.11-7.13 contain quantitative analyses of these uncertainties and their effects on the thermal forces.

7.1.1 Parameter sensitivity

The sensitivity of the force models to the optical properties and other model parameters is investigated for both the solar panels and the MLI.

7.1.1.1 Solar panels

The basic equations, taken from Section 4.2.2, used to evaluate the solar panel force, are:

$$T_f = T_b + R_{total}\varepsilon\sigma A T_b^4 \tag{4.16}$$

$$\varepsilon\sigma(T_b + R_{total}\varepsilon\sigma A T_b^4)^4 + \varepsilon\sigma T_b^4 + q_{elec} - \alpha W\cos\theta = 0 \tag{4.17}$$

$$F = \frac{-2A\sigma(\varepsilon_f T_f^4 - \varepsilon_b T_b^4)}{3c} \tag{4.18}$$

Equation 4.17 is solved for the back face temperature using the Newton-Raphson method, which is substituted into 4.16 to calculate the front face temperature, and Equation 4.18 is then used to calculate the force. It is not straight forward to carry out an analytical error analysis for the force due to the interdependency of variables in Equation 4.18; hence a numerical error analysis is conducted.

The errors in some variables are small and have negligible effect on the force. These include the dimensions of the panel, which have been measured with millimetric precision and associated errors are at the 0.01% level. Similarly the error in the solar irradiance due to the solar cycle are at the 0.1% level, and will have no significant effect on the force either. Physical constants such as the speed of light and the Stefan Boltzmann constant are sufficiently well determined to contribute no error to the final model. The power draw issue requires lengthier discussion and is treated separately in Section 7.1.3. For the GPS Block IIR solar panels, the remaining parameters, their associated uncertainties and corresponding uncertainties in the force are given in Table 7.1. Where the uncertainty is written in parentheses, a true value was unobtainable and an estimated value has been given. Maximum along-track orbit errors after 12 hours

caused by each parameter have been calculated by assuming the force acts constantly in one direction, which is perpendicular to the panel.

Parameter	Nominal value	Uncertainty	Uncertainty in force (N)	Max along-track error after 12 hrs (m)
α	0.72	(± 0.03)	7.693×10^{-8}	0.0653
ε_f	0.86	± 0.02	3.082×10^{-7}	0.2615
ε_b	0.89	(± 0.02)	2.909×10^{-7}	0.2468
θ	0	±1°	2.755×10^{-10}	0.0002
R_{total}	0.0161 m^2KJ^{-1}.	(± 0.0008)	5.860×10^{-8}	0.0497
W	1368 Wm^{-2}	± 0.7 Wm^{-2}	9.259×10^{-10}	0.0008
A	13.62547 m^2	± 0.00005 m^2	5.605×10^{-13}	4.75×10^{-7}

Table 7.1: GPS Block IIR solar panel surface parameters and uncertainties

The magnitude of the force produced using nominal values of the parameters at one astronomical unit is -7.64×10^{-7} N (in a direction normal to the front face of the solar panels). Combining the errors calculated above yields a maximum possible force error of 6.33×10^{-7} N and maximum distance errors of ~50cm.

A similar analysis was carried out for Jason-1. No uncertainty parameters were supplied for Jason-1 properties, and those of the GPS Block IIR panels were used. The results are shown in Table 7.2. Along track errors are shown over one orbit (112 minutes).

Parameter	Nominal value	Uncertainty	Uncertainty in force (N)	Max along-track error after 1 orbit (m)
α	0.75	(± 0.03)	6.872×10^{-8}	0.0035
ε_f	0.82	± 0.02	2.407×10^{-7}	0.0123
ε_b	0.82	(± 0.02)	2.353×10^{-7}	0.0121
θ	0	±1°	1.274×10^{-9}	6×10^{-5}
R_{total}	0.0164 m^2KJ^{-1}.	(± 0.0008)	4.739×10^{-8}	0.0024
W	1368 Wm^{-2}	± 0.7 Wm^{-2}	8.922×10^{-10}	5×10^{-5}
A	9.563 m^2	± 0.00005 m^{-2}	5.090×10^{-12}	3×10^{-7}

Table 7.2: Jason-1 solar panel surface parameters and uncertainties

The magnitude of the force produced using nominal values of the parameters at one astronomical unit is -9.71 x 10^{-7} N (in a direction normal to the front face of the solar panels).

Combining the errors calculated above yields a maximum possible force error of -5.70 x 10^{-7} N. After one Jason-1 orbit, this maps into a distance error of ~3cm. Due to the higher area to mass ratio of Jason-1 compared to GPS Block IIR, after twelve hours, the errors reach the 1 metre level.

These errors are substantial. It should be noted that these distances are overestimates, since the TRR force does not always act in the same direction. By far the largest source of error is due to the front and back emissivities; within the range of the parameters, the resultant force varies hugely as can be seen in Table 7.1 and 7.2. This is because the front and back emissivities are scaled by the fourth power of the temperatures. As stated earlier, it would be greatly beneficial if more research was directed towards defining these parameters with greater certainties. It is likely that some of the remaining orbit prediction residuals, which are at the 0.6m level as an RMS range over twelve hours, can be explained by erroneous values being used in this model.

The nominal solar panel force is higher for Jason-1 than for GPS Block IIR. This is mainly due to the fact that GPS Block IIR panels have a higher back face emissivity than front face emissivity. This leads to a high degree of cancellation of the force produced from the front face. For Jason-1, the front and back emissivities are equal and hence less cancellation occurs.

7.1.1.2 MLI

The temperature of the MLI and the corresponding TRR force are given in Equations 4.34 and 4.35, which were derived in Section 4.3.2.

$$T_{MLI}{}^4 = \frac{\alpha W \cos\theta + \varepsilon_{eff}\sigma T_{sc}{}^4}{\sigma(\varepsilon_{mli} + \varepsilon_{eff})} \tag{4.34}$$

$$F = -\frac{2}{3c}\sigma\varepsilon_{MLI}T_{MLI}{}^4 \tag{4.35}$$

Table 7.3 contains the parameters used in the MLI models for GPS Block IIR spacecraft.

Parameter	Nominal	Uncertainty	Uncertainty in force (N)	Max along-track error after 1 orbit (m)
α	0.94	(± 0.03)	8.9470×10^{-8}	0.0758
ε_{MLI}	1	(- 0.1)	6.1370×10^{-9}	0.0052
ε_{eff}	0.02	±0.02	3.5167×10^{-8}	0.0298
θ	0	±1°	4.2699×10^{-10}	0.0004
T_{sc}	298 K	±25 K	5.7643×10^{-9}	0.0049
Solar irradiance	1368 Wm^{-2}	±0.7	1.4345×10^{-9}	0.0012

Table 7.3: GPS Block IIR MLI parameters and uncertainties

The nominal force per unit area of MLI is 2.823×10^{-6} Nm^{-2}. Using the errors calculated above, the maximum force error (at the one sigma level) is -2.8661×10^{-8} Nm^{-2} and the maximum displacement arising from this error is ~10cm.

The MLI model is not highly dependent on the emissivity of the MLI. This is because a higher value of this parameter acts to decrease the temperature and reduce the force, but also to increase the amount of energy emitted and hence increase the force, with little net change in the resultant force. This error analysis shows that the MLI model is not strongly dependent upon the accuracy of the surface parameters. The same result was found for Jason-1's MLI surfaces.

7.1.2 Mass sensitivity

The nominal mass quoted for GPS Block IIR spacecraft is 1100 kg (Bar-Sever, Y., 1997). Table 7.4 shows masses of some GPS Block IIR spacecraft in March 2004 which have been used in the orbit prediction tests described in Section 5.4.3. It can be seen that most spacecraft masses are fairly close to their nominal mass during this period, apart from SVN 46. Accurate mass data is not readily available; the data in Table 7.4 was only obtained close to the end of this study but its impact on the results was very significant, especially for SVN 46.

SVN number	Mass in March 2004 (kg)
41	1098.2535
43	1098.0510
44	1098.5375
46	1086.4512
51	1099.7369

Table 7.4: Mass of GPS Block IIR spacecraft in March 2004

Table 7.5 show the results of 12 hour orbit predictions using actual masses and nominal masses for SVNs 41, 43, 44, 46 and 51. The greatest departure from nominal mass is for SVN 46, which differs from the nominal by ~1.5%.

SVN	12 hour RMS GPS Block IIR orbit prediction residuals					
	Nominal masses			Real masses		
	H (m)	C (m)	L (m)	H (m)	C (m)	L (m)
41	0.25	0.08	0.55	0.22	0.08	0.53
43	0.17	0.11	0.72	0.16	0.11	0.75
44	0.14	0.03	0.58	0.14	0.03	0.59
46	0.29	0.07	1.02	0.14	0.07	0.46
51	0.24	0.11	0.82	0.23	0.11	0.80

Table 7.5: HCL residuals for 12 hour orbits averaged over 4 weeks in March 2004

A bar chart of the residuals for SVN 46 is shown in Figure 7.1.

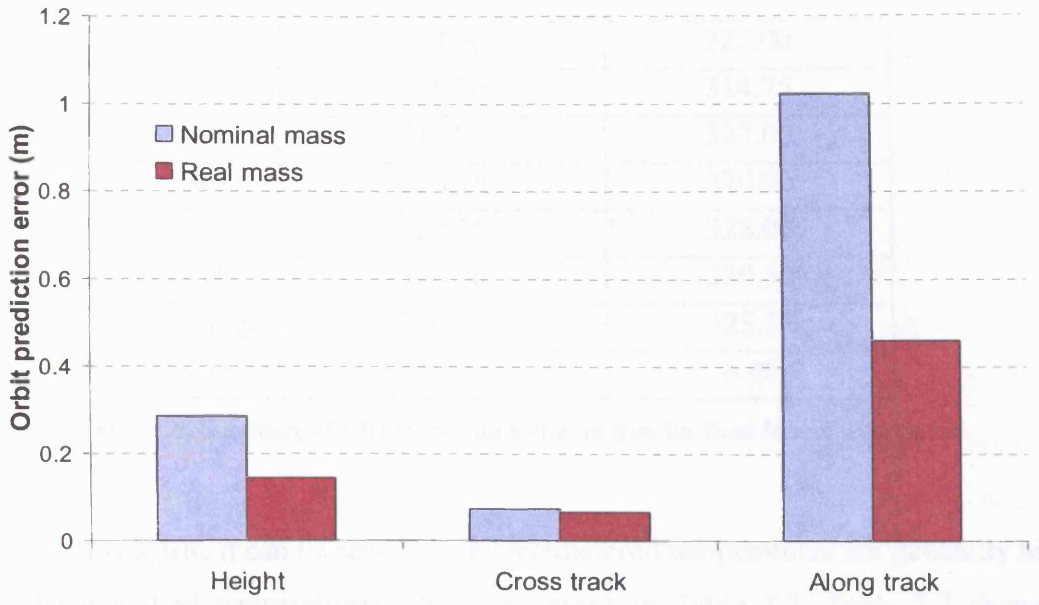

Figure 7.1: Orbit prediction errors for SVN 46, using real and nominal masses

The improvements in residuals show the importance of using accurate masses in orbit prediction. A time series of accurate masses is not publicly available, making testing at other time periods very difficult. In orbit determination, incorrect mass is likely to be less problematic as a scale factor should soak up any errors associated with it.

7.1.3 Solar panel power draw

This section attempts to discuss possible reasons for the discrepancy between the modelled and telemetered temperatures (which was given in Section 5.5.1.) and to show how much the models are affected by the assumed power draw. Table 7.6 summarises the telemetered data from temperature sensors on the Block IIR satellites, The ±Y refer to the sides of the spacecraft. For GPS Block IIR, power is drawn from either the inner or the outer panels. Unfortunately no information was available as to which panels the temperature sensors are mounted on, hence it is unclear whether power is being drawn from them or not.

SVN	Average telemetered temperatures (K)	
	+Y	-Y
41	313.50	322.00
43	315.50	314.75
44	318.25	327.00
46	326.75	329.00
51	320.75	328.00
54	326.50	330.50
Average	320.21	325.21
SD	5.60	6.40

Table 7.6: Summary of telemetered temperature data for front face of solar panels.

For GPS Block IIR, it can be seen that the telemetered temperatures are generally higher than the modelled temperatures which are given in Table 7.7. Table 7.7 shows the modelled front face temperatures change as the amount of power drawn is varied. Column A shows the modelled temperature derived when nominal values for optical parameters were used (α = 0.72, ε_f = 0.86, ε_b = 0.89). In column B, the optical parameters have been changed to values within their formal error margins (α= 0.75, ε_f= 0.88, ε_b = 0.87), to create the highest realistic temperatures.

Power draw (Wm^{-2})	Modelled temperature (K)	
	A	B
90	311.67	315.90
50	315.20	318.55
0	319.47	322.68

Table 7.7: Front face panel temps for varying power draw and optical parameters

Using a power draw of 90 Wm^{-2}, the modelled temperatures are significantly lower than the telemetered temperatures but by decreasing the amount of power draw, this difference is reduced. When the optical properties are modified by their uncertainties, the temperatures become very similar to the telemetered ones. If the solar sensors are located on panels from which power is not being drawn, this could explain the discrepancies between the two sets of temperatures. The telemetered data varies hugely between the spacecraft and between the ±Y sides. From Tables 7.6 and 7.7, it can be

seen that the models and observations are consistent within one standard deviation of the observations.

A number of other factors could also account for some or all of the temperature discrepancy. Firstly, the telemetered data higher for the –Y panels than for the +Y panels, for all but one satellite. This is unusual in that the physical structure of the satellite and its design modes are nominally symmetrical. If one of the panels was somehow mis-pointing, the flux received by the –Y side would be different to the flux received for the +Y side (see Figure 7.2). Mis-pointing might be as a result of either manufacturing errors, incorrect deployment of the solar panels, or general wear and tear over the lifetime of the spacecraft. However, a mis-pointing angle of one of the panels by 5° would cause a temperature difference of less than 0.5K, so this would not explain the differences that can be seen in the telemetered data.

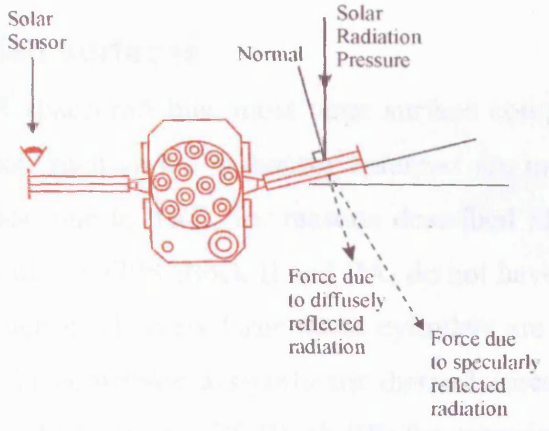

Figure 7.2: A mis-pointing panel

A more reasonable argument for the discrepancy might be that power is not being drawn equally from both sides. The temperature differences between the left and right panel can be recreated if the average power draw is kept at $90Wm^{-2}$ but more is taken from one side than the other. It is unlikely that the power draw regime is as simple as a standard value of 90 Wm^{-2} from either the inner or outer panels, though this was the data available to us. A variable power draw regime is more likely, as is the case for Jason-1 (described in section 6.3.2). A measure of the accuracy of the temperature sensors and how well they are calibrated is required to better interpret and attain confidence in the data. The large variations in temperature between the satellites and

discrepancies between the left and right panels raise questions as to how sensitive and accurate these instruments are.

As described in Section 5.2.4, thermal radiators on the ± Y faces of the spacecraft vent heat away from the spacecraft bus. It was assumed that heat was vented equally from both sides. From a design viewpoint this would be preferable, though no data was available to support this. If, however, the internal components of the bus are arranged in such a way that one part of the bus produces more heat than other parts, this might cause heat to be vented out of the bus asymmetrically. (In the GPS Block IIR spacecraft, the navigation computer and clocks are situated on the –Y side of the spacecraft bus). If the vented heat impacts upon the solar panels, this would cause the panels to warm up somewhat and may explain why the telemetered temperatures are higher than those modelled. If the heat venting is asymmetrical, then this could also explain the discrepancies between the +Y and –Y panels.

7.2 Unmodelled surfaces

For the GPS Block IIR spacecraft bus, most large surface components are covered in MLI. Those that are not, such as the W-sensor antennas are unlikely to have a large effect on the acceleration due to TRR, for reasons described in Section 5.2.4. Earlier models of GPS spacecraft, i.e. GPS Block II and IIA, do not have a shroud covering the +Z face antennas, and hence relatively large metal cylinders are exposed. It is unlikely however that they would contribute a significant thermal force because of the same argument used for the W-Sensors on GPS Block IIR: the antennas are cylindrical, fairly thin, and made of a highly conductive material (aluminium), thus a roughly symmetrical temperature distribution about the central axis of each cylinder is expected and emission will be almost equal in all directions perpendicular to this axis at each point along its length. Due to the cancellation of forces in opposite directions, only a small net force is expected.

For Jason-1, some sizeable surfaces remain un-modelled from a thermal re-radiation point of view. This is partly because it is impossible to obtain detailed structural data about these objects; the data files included only surface properties. If the structural and material property data were obtainable, a finite element analysis method could in theory

be employed. As mentioned in Section 5.4.2, many commercial packages which carry out detailed thermal analyses exist, (eg ESATAN[17] and Radtherm[18]). The problem with incorporating these methods is that the computational burden may well outweigh any gains in accuracy, given that even fairly crude models are likely to be complex. It is however important to quantify what affect these models have and whether their omission is justified.

The largest structures on the surface of Jason-1 are the radar altimeter dish and the microwave radiometer dish shown in Figure 7.3.

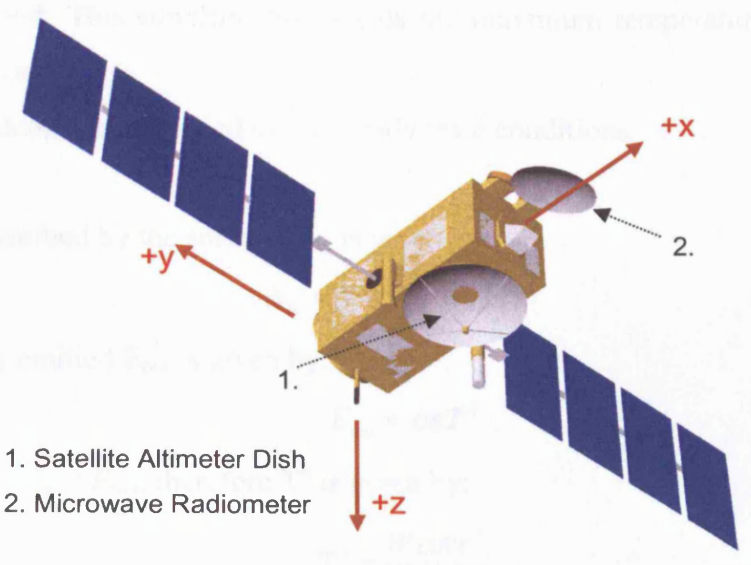

Figure 7.3: Large un-modelled features on Jason-1 spacecraft

A calculation was made to estimate the acceleration caused by the microwave radiometer and is based on the following arguments:

- The sides and rear of the dish are covered in MLI. For the most part, the +Z face of the spacecraft faces earth and will not receive much solar radiation. As a result of the inclination of the spacecraft and its low altitude, when the EPS angle is close to 180°, the spacecraft is in eclipse, preventing the +Z face from receiving much radiation. Therefore, in this calculation, it is assumed that the

[17] For details see http://www.techcentreuk.power.alstom.com

[18] For details see http://www.thermoanalytics.com/products/radtherm

emitting source is the Earth. At the orbit altitude of Jason-1 the Earth flux is estimated to have a maximum value of about 250 Wm^{-2}. This is based on interpolations between calculated values for GPS Block IIR and GRACE (altitude ~ 500km) (pers comms, Edwards, S., Aug 2004).

- The inner surface of the dish is a paraboloid. Assuming that the dish is a flat circle will, if anything, over-estimate the force while simplifying the calculation. The dish has a radius of ~ 0.5m.
- The dish is covered in white paint and has an absorptivity of 0.28 (ESABASE file)
- It is assumed that no thermal coupling takes place between the dish and the spacecraft. This simplification yields the maximum temperature and force that can occur.
- The calculation is carried out in steady state conditions.

The energy absorbed by the surface, E_{in} is given by:

$$E_{in} = W\alpha A = W\alpha\pi r^2 \tag{7.1}$$

and the energy emitted E_{out} is given by:

$$E_{out} = \sigma\varepsilon T^4 \tag{7.2}$$

In steady state, $E_{in} = E_{out}$, therefore T^4 is given by:

$$T^4 = \frac{W\alpha\pi r^2}{\sigma\varepsilon} \tag{7.3}$$

and the force F is given by:

$$F = -\frac{2\sigma\varepsilon T^4}{3c} = -\frac{2W\alpha r^2\pi}{3c} \tag{7.4}$$

This force results in an acceleration of 5.11 x 10^{-11} ms^{-2}; doubling this to include an estimate for the radar altimeter gives a total acceleration of 1.22 x 10^{-10} ms^{-2}.

Over one orbit of Jason-1 (112 mins), this could cause a *maximum* displacement of ~3 mm though it would actually be smaller than this. At the current level of modelling, this can be considered negligible. The acceleration is small partly due to the low absorbtivity of the white paint. Over longer arcs (for example 12 hours) a maximum

displacement of ~10cm could occur if the effect were systematic over many orbits, and may no longer be considered negligible.

7.3 Once per revolution fitting

The fitting of once per orbit revolution (once per rev) empirical terms to soak up un-modelled effects is a commonly employed process in orbit determination (see Section 3.3.2). Different orbit determination schemes choose different frames of reference in which to fit such once per rev terms. CODE for example uses the YPS basis and whereas GIPSY-OASIS II uses the BFS XYZ basis. Depending upon the periodicity and signature of the un-modelled effect, fitting will be more successful in some frames than in others (Ziebart, M. et al., 2003a).

The periodicity of the thermal force was investigated by transforming the calculated force into different coordinate systems (described in Section 2.3). These were:

1. Earth Centred Inertial (ECI)
2. Height Cross Along track (HCL)
3. Y Probe-sun (YPS)
4. Body Fixed System XYZ (BFS)

The accelerations in each basis for SVN 43 over for one orbit on the 3rd March 2001 are given as an example in Figures 7.4 – 7.7. The black lines show once per rev fits for the acceleration in each component.

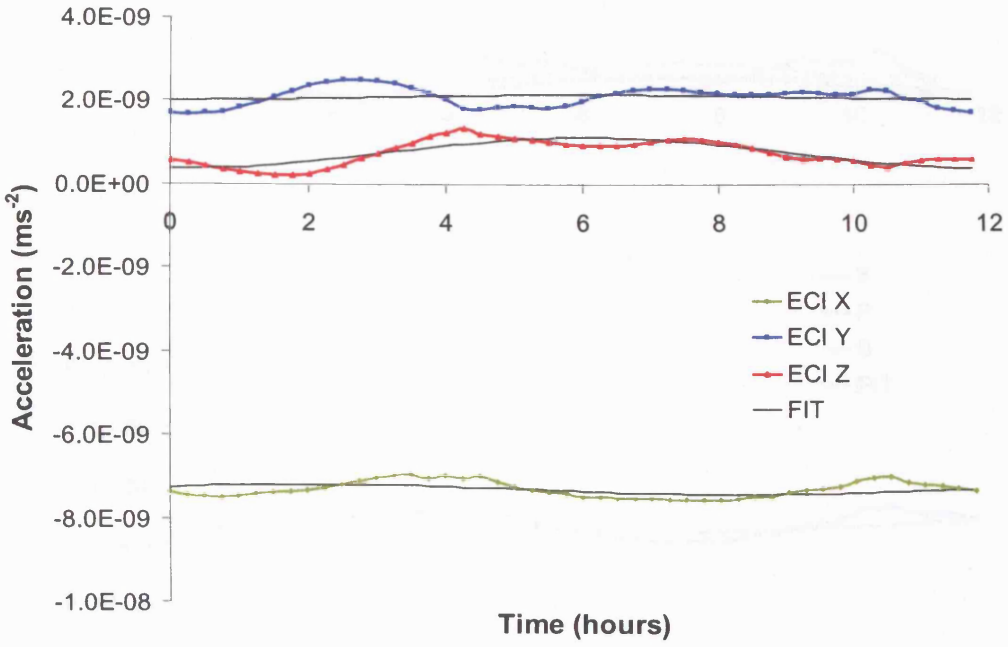

Figure 7.4: Thermal force in ECI frame

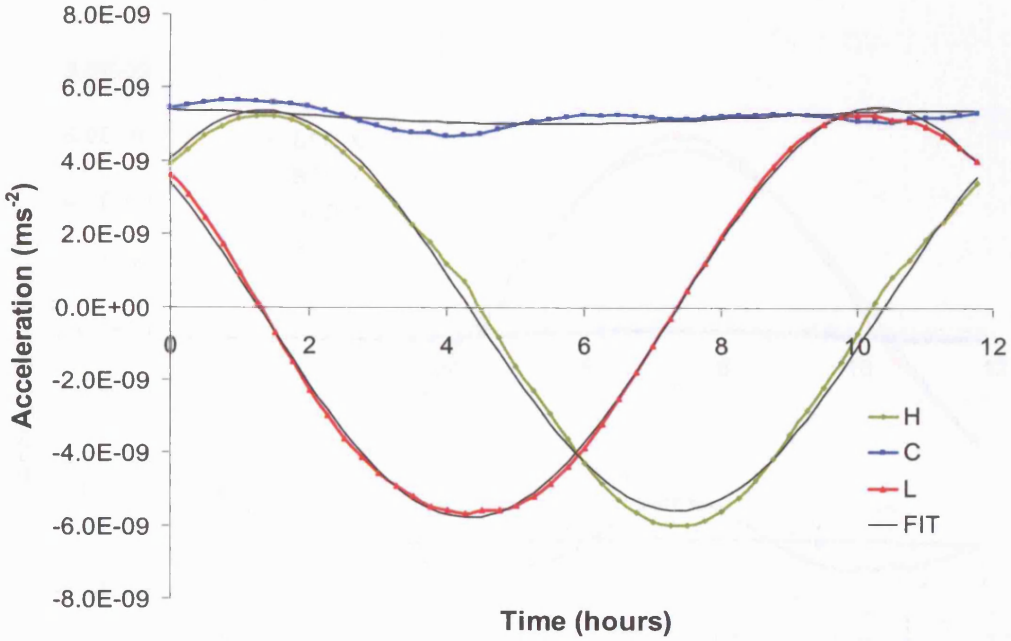

Figure 7.5: Thermal force in HCL frame

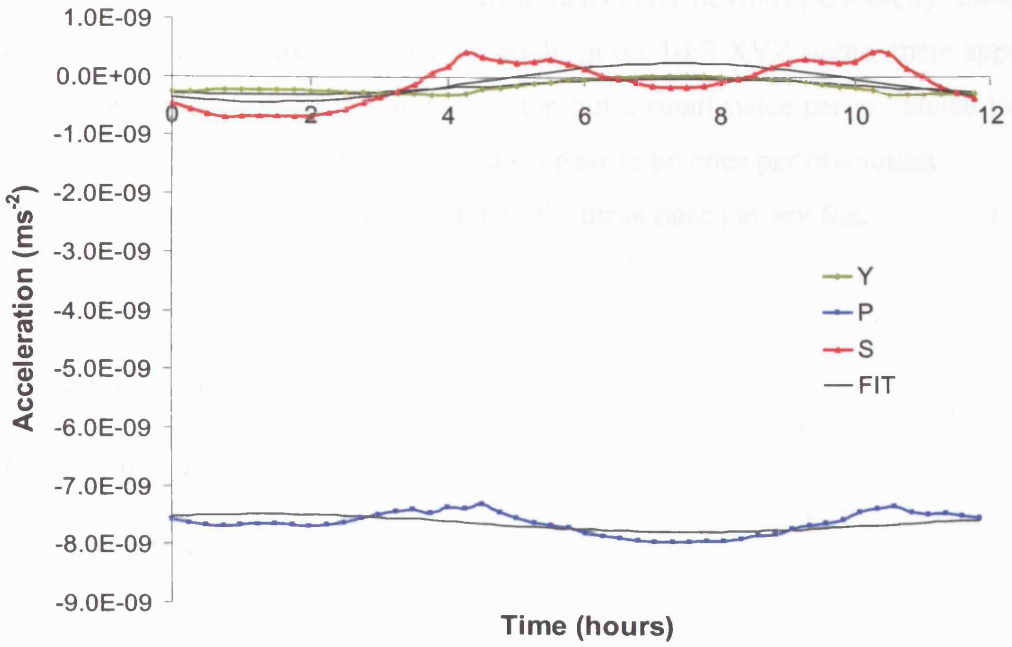

Figure 7.6: Thermal force in YPS frame

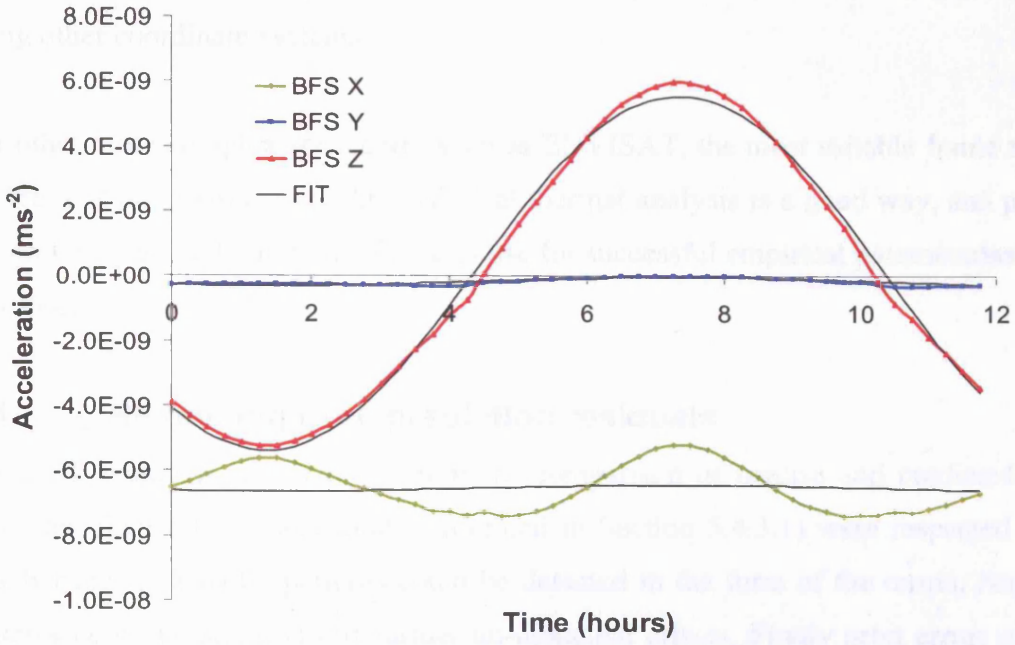

Figure 7.7: Thermal force in BFS XYZ frame

In the ECI and YPS frames, it is difficult to detect any obvious periodicity, though the variations in accelerations are relatively small. In the BFS XYZ frame, there appears to be a once per revolution fit in the Z direction but a small twice per rev signal in the X direction. In the HCL frame, the signals do appear to be once per revolution.
RMS acceleration residuals were calculated for these once per rev fits:

HCL: 3.3×10^{-10} ms^{-2}

YPS: 3.2×10^{-10} ms^{-2}

ECI: 3.3×10^{-10} ms^{-2}

BFS: 7.5×10^{-10} ms^{-2}

These results show that parameterisation in either the ECI, HCL or YPS frames give good fits with once per rev parameters, though it is the HCL frame which shows the most once per revolution periodicity. GIPSY-OASIS II carries out parameterisation in the BFS XYS frame as does the Master Control Station when processing GPS orbits. This frame leads to the highest residuals for GPS spacecraft, more than double the size using other coordinate systems.

For other more complex spacecraft, such as ENVISAT, the most suitable frame may be different, if one exists at all. An analytical thermal analysis is a good way, and perhaps the only way to find out which frame to use for successful empirical parameterisation of this force.

7.4 Remaining orbit prediction residuals

The HCL residuals which arose from the comparison of precise and predicted orbits using the final set of force models (defined in Section 5.4.3.1) were inspected to see whether any systematic patterns could be detected in the form of the errors. Any such patterns could be signifiers of further un-modelled effects. Firstly orbit errors over 12 hours were visually examined for each individual spacecraft over the course of the four weeks in March 2004. No clear pattern emerged, suggesting that it is unlikely that spacecraft specific effects are causing systematic deviations to the predicted orbits.

For forces which are dependent on the solar flux, it is possible that errors may be associated with the beta angle. The beta angle is defined as the acute angle between the Sun-Earth vector and the orbit plane (Bar-Sever, Y., 1996b) and for GPS satellites will range between ± 90° over one year. GPS spacecraft occupy six planes, separated by 60°, labeled A-F. Table 7.8 shows the planes of all the GPS Block IIR spacecraft analysed.

SVN	Plane
41	F
43	F
44	B
46	D
51	E

Table 7.8: GPS Block IIR orbit planes

Both SVN 41 and 43 occupy the same plane (F) and hence have the same beta angle for any epoch. The patterns of HCL residuals were compared for these two satellites for the same day throughout March 2004. Figures 7.8 and 7.9 are the HCL residuals for the 2nd March and 10th March 2004 and are given as examples.

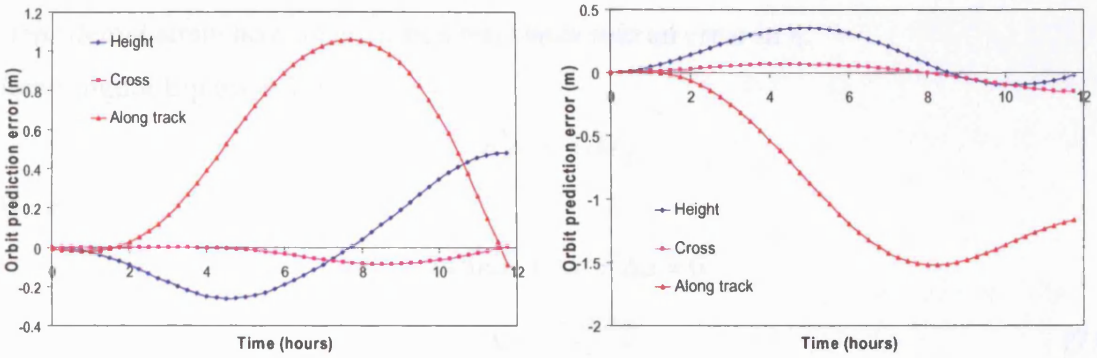

Figure 7.8: HCL residuals for 2nd March 2004 (SVN 41 left, SVN 43 right)

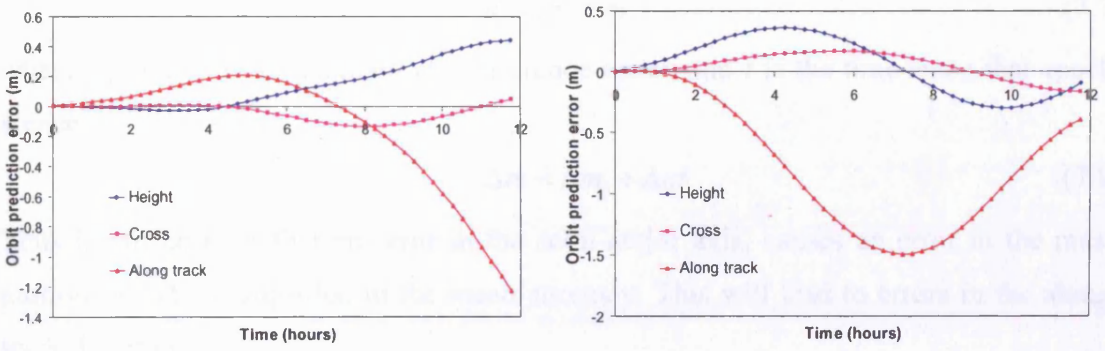

Figure 7.9: HCL residuals for 10th March 2004 (SVN 41 left, SVN 43 right)

This analysis showed no clear similarities in the patterns of residuals for SVN 41 and 43, it is not possible to see a particular effect occurring as a function of beta angle.

An interesting feature which was apparent in many of the orbits predictions, was that the error in the height direction appeared to have a once per rev signature, and was small compared to the along track errors. In most cases, when the radial error returns to zero after one orbit, as in Figure 7.9 (right), there is usually no resultant error in the along track direction. Equally, when the radial error continues to increase, as in Figure 7.9 (left), so does the along track error.

An explanation as to why a radial error may be associated with a larger along-track error follows. The mean motion n of a satellite describes the average angular frequency at which a spacecraft moves in orbit (following from Kepler's third law) and is defined by:

$$n = \sqrt{\frac{GM_E}{a_{sm}^{\ 3}}} \tag{7.5}$$

where a_{sm} is the semi-major axis (Montenbruck, O. & Gill, E., 2000). The following steps demonstrate how an error in a translates into an error in n:
Rearranging Equation 7.5:

$$n^2 a^3 = GM_E$$

Hence:

$$2n\Delta n a^3 + 3a^2 n^2 \Delta a = 0$$

$$\Delta n = \frac{-3n\Delta a}{2a} \tag{7.6}$$

The mean anomaly m is defined as:

$$m = m_0 + nt \tag{7.7}$$

where m_0 is the mean anomaly at a reference epoch and t is the time since that epoch. Hence:

$$\Delta m = \Delta m_0 + \Delta n t \tag{7.8}$$

Thus it can be seen that an error in the semi-major axis, causes an error in the mean motion, which is amplified in the mean anomaly. This will lead to errors in the along-track direction.

7.5 Erroneous initial state vector

For GPS Block IIR, the force models were evaluated by how well predicted trajectories compared to a JPL precise orbit. This method of evaluation is based on the assumption that the initial state vector is a very good estimate of the position and velocity of the spacecraft. It will however have some errors associated with it. Small inaccuracies in this initial state vector, especially in the velocity would cause the predicted trajectory to diverge even more from the precise orbit than they would if based solely on the errors in the force models. Thus it could be that the dynamic models are more accurate than the orbit prediction results suggest. Precise orbit positions are quoted to be accurate to ~ 3cm (http://igscb.jpl.nasa.gov/components/prods.html) but no value is quoted for the accuracy of velocities.

If this hypothesis is true there should exist a set of initial conditions which, when propagated forward, result in trajectories closer to the precise orbits than those obtained using the initial conditions taken from the precise orbit files.

A method for testing this hypothesis is to use a least squares fitting technique to solve for the set of initial conditions which allow the predicted trajectory to best fit the precise trajectory, and then to re-compute the predicted trajectory with this set of initial conditions.

Equation 7.9 is the matrix form of the normal equations used in the least squares estimation process.

$$[\Phi][\Delta x] = [B] \tag{7.9}$$

where $[\Phi]$ is the design matrix which contains the partial derivatives of the state vector (position and velocity) at each epoch with respect to the initial state vector. $[\Delta x]$ is the one dimensional matrix containing corrections to the initial conditions and B is the difference between the precise orbits and the predicted orbit. Equation 7.10 shows the matrix elements. The subscript n denotes the epoch which run from 0 to n. Rows 0 to $n+1$ contain the partial derivatives of the x element of the position vector with respect to the initial state vector at each epoch; rows $n+2$ to $2(n+1)$ contain the partial derivatives

of the y element of the position vector with respect to the initial state vector at each epoch and so on.

$$\begin{bmatrix} \frac{\partial x_0}{\partial x_0} & \frac{\partial x_0}{\partial y_0} & \frac{\partial x_0}{\partial z_0} & \frac{\partial x_0}{\partial u_0} & \frac{\partial x_0}{\partial v_0} & \frac{\partial x_0}{\partial w_0} \\ \frac{\partial x_1}{\partial x_0} & \frac{\partial x_1}{\partial y_0} & \frac{\partial x_1}{\partial z_0} & \frac{\partial x_1}{\partial u_0} & \frac{\partial x_1}{\partial v_0} & \frac{\partial x_1}{\partial w_0} \\ \vdots & & & & & \vdots \\ \frac{\partial x_n}{\partial x_0} & & & & & \vdots \\ \frac{\partial y_0}{\partial x_0} & & & & & \vdots \\ \vdots & & & & & \vdots \\ \frac{\partial y_n}{\partial x_0} & & & & & \vdots \\ \vdots & & & & & \vdots \\ \frac{\partial w_0}{\partial x_0} & & & & & \vdots \\ \vdots & & & & & \vdots \\ \frac{\partial w_n}{\partial x_0} & \cdots & \cdots & \cdots & \cdots & \frac{\partial w_n}{\partial w_0} \end{bmatrix} \begin{bmatrix} \Delta x_0 \\ \Delta y_0 \\ \Delta z_0 \\ \Delta u_0 \\ \Delta v_0 \\ \Delta w_0 \end{bmatrix} = \begin{bmatrix} (precise - predicted)x_0 \\ (precise - predicted)x_1 \\ \vdots \\ (precise - predicted)x_n \\ (precise - predicted)y_0 \\ \vdots \\ (precise - predicted)y_n \\ \vdots \\ (precise - predicted)w_0 \\ \vdots \\ (precise - predicted)w_n \end{bmatrix} \tag{7.10}$$

To populate the design matrix at each epoch, we need to calculate the partial derivative of each element of the state vector with respect to the initial state vector. At epoch n, x_n is computed by integration of the dynamic model using x_0 as the start point. x_0 is then changed by a small amount and x_n recalculated. This is repeated for eight values of x_0 and an eighth order polynomial is fitted to these points, as shown in Figure 7.10. This can be differentiated and evaluated at x_0. This process needs to be repeated for each element of the state vector at each epoch.

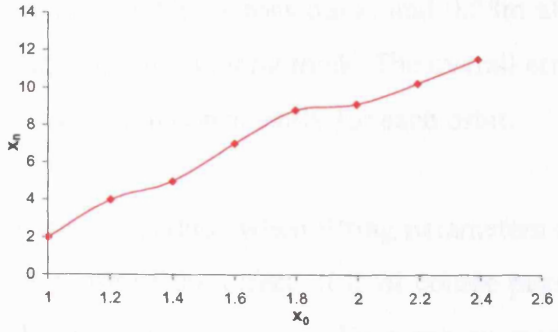

Figure 7.10: Plot of x_n against x_0

Equation 7.10 can be solved by the least squares solution:

$$[\Delta x] = [\Phi^T \Phi]^{-1} [\Phi]^T [B]$$

When the solution converges, the initial condition which causes the dynamically modelled trajectory to best fit the precise orbit has been obtained.

For a twelve hour integrated orbit, the initial conditions were estimated based on the first two hours of the arc. The precise orbit gives a state vector at 15 minute intervals and so Φ is a 48 x 6 matrix: (6 x 2 x 4) x (6): 6 for each element in the state transition matrix, 2 for the number of hours, and 4 for the number of data points per hour).

7.5.1 Results

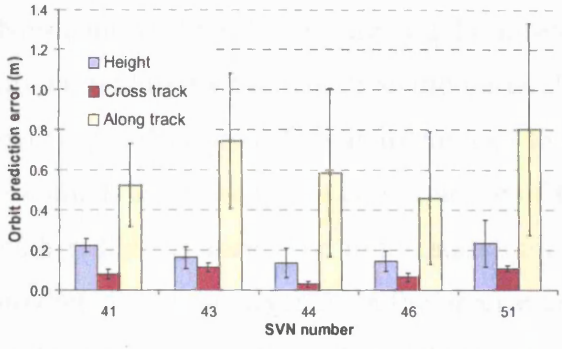

Figure 7.11: Full orbit prediction results optimised initial (same as Figure 5.11)

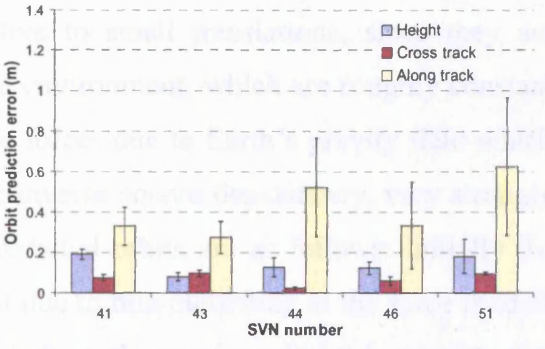

Figure 7.12: Orbit prediction results using conditions

Figures 7.11 and 7.12 are the results of 12 hour orbit predictions for March 2004, using the initial state vector from the precise ephemeris and the estimated initial state vector. Error bars showing the standard deviations are shown. The mean RMS residuals have

reduced from 0.19m in height, 0.07m across track, and 0.58m along track to 0.12m in height, 0.06m across track, and 0.42m along track. The overall errors have been reduced by ~30%. Improvements were seen consistently for each orbit.

Indeed, the residuals will always reduce when fitting parameters using least squares and this does not "prove" the cause of the effect. It is of course possible that adjusting the initial conditions could be partially accounting for some un-modelled or mis-modelled effect which is correlated with the initial velocity. A key point here is that the initial conditions were optimised using only the first two hours of precise orbit data, whereas the RMS residuals consistently improved over twelve hours of orbit propagation. The results imply that a substantial proportion of the error remaining after the thermal models have been applied may not be due to inaccuracies in the force models, but inaccuracies in our "truth" model, which we know to be erroneous at some level.

Though this result is not directly useful in orbit prediction as initial conditions can only be optimised once the precise orbit is known, it does however highlight the sensitivity to the initial conditions, and suggest that a substantial part of the remaining residuals may not be due to failings in the dynamic model.

7.6 Earth's gravity field

Non-conservative forces are highly insensitive to small translations, since they are driven mainly by the radiative and particulate environment, which are roughly constant over short distances. This is in contrast to the forces due to Earth's gravity field which are much larger and, as a consequence of the inverse square dependency, vary strongly with radial distance. The implications for predicted orbits are as follows: initially the predicted orbit diverges from the precise orbit due to mis-modelling in the force models and inaccuracies in the initial state vector taken from the precise orbit. It is possible that once small divergences have occurred, these are then exacerbated by the application of position dependent forces, such as the Earth's gravity force. To demonstrate this point, the following situation is considered: if at one epoch, the predicted position of the spacecraft has a larger radial value than its precise position, a smaller Earth's gravitational force will be applied to it, causing its radial component to become even

larger. This will result in further deviation from the precise trajectory, again implying that not all the error is a direct result of inadequacies in the force model.

A ball park figure can be estimated for the difference in gravity caused by 10 cm radial error at an orbit altitude of GPS satellites. Considering the action of the monopole term only, Equation 7.11 gives the difference in acceleration Δg:

$$\Delta g = GM\left(\frac{1}{r^2} - \frac{1}{(r+\Delta r)^2}\right) \tag{7.11}$$

where:

$GM = 398600.4415\ \mathrm{km^3 s^{-2}}$

$r = 26000\mathrm{km}$ (approximate value for the semi-major axis)

$\Delta r = 1 \times 10^{-4}\ \mathrm{km}$ (10 cm)

Substituting these values into Equation 7.11 yields:

$$\Delta g = 4.5\mathrm{E}-9 ms^{-2}$$

This difference in acceleration has a similar magnitude to many of the non-conservative forces, albedo, thermal forces, antenna thrust, and will definitely cause an appreciable deviation of the predicted orbit from the precise orbit. To investigate how much this contributes to the residuals resulting from orbit prediction, the predicted trajectory is produced by integration of the force models as before, but at each epoch, the gravity field term derived from the precise orbit position is applied to the integrated position.

The following bar-charts show the orbit integration results obtained when this technique was applied. Figure 7.13 shows results of the orbit predictions when the integrated position derived gravity terms were used. Figure 7.14 shows these results when the

gravity field has been adjusted and the initial state vector has been optimised.

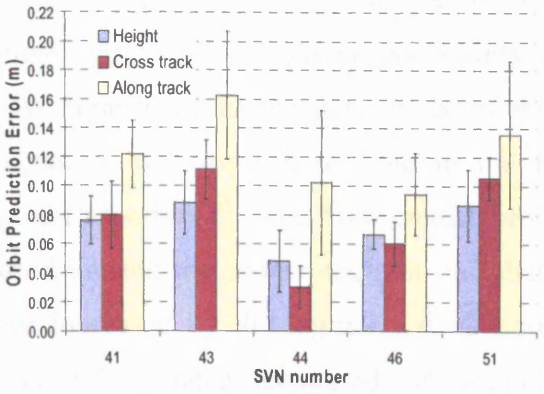

Figure 7.13: HCL residuals: adjusted gravity field

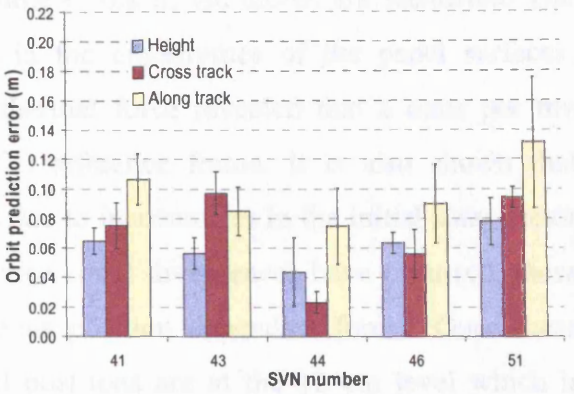

Figure 7.14: HCL residuals: adjusted gravity field and initial state vector

The mean RMS residuals for the results shown in Figure 7.13 are 0.07 m in height, 0.07 m across track, and 0.12 m along track. The mean RMS residuals for the results shown in Figure 7.14 are 0.06m in height, 0.06m across track, and 0.09 m along track.

These results show that small errors in the estimations of position will escalate into larger errors caused by using an incorrect gravity term. From an orbit prediction point of view, we cannot achieve results at the 10 cm level, but our force modelling only needs to improve a little for the final orbit prediction errors to reduce significantly. Put another way, the error represented by the residuals is not solely due to errors in the modelling of the forces.

Inclusion of the thermal re-radiation obviously leads to clear gains, and remaining errors can be reduced by improvements in models of non SRP and TRR effects. Agencies such as the IGS[19] use orbit prediction to produce ultra rapid orbits (which are accurate to ~10 cm in the radial direction) and clocks for use in near real time and real time positioning. They achieve improved orbit predictions (compared to the broadcast ephemeris) by empirically modelling other effects which impact on the orbit. A predicted orbit which incorporates both accurate force modelling and better modelling of other factors is likely to give the best solution.

[19] http://igscb.jpl.nasa.gov/components/prods.html

Summary

In this chapter, significant sources of possible errors in the model are identified. The most significant parameter uncertainty is in the emissivities of the panel surfaces. Investigations into the periodicity of the thermal force revealed that a once per rev signature was most noticeable in the HCL reference frame. It is also shown that predicted orbits diverge from precise orbits due to inaccuracies in the initial state vector used to seed the orbit integrator and that once small divergences have occurred, these are increased by the application of erroneous position dependent forces. Once these factors have been accounted for, predicted positions are at the 12 cm level which is getting close to the noise level of precise orbits (~5cm). Chapter 8 contains a general appraisal of the models developed in this thesis and discusses specific applications in which they have been used.

Chapter 8 Discussion

Chapter outline

In this chapter the main strengths and weaknesses of the models developed in this thesis are discussed. The impact of the thermal re-radiation force in mission design and operation are outlined and areas where the work developed in this thesis is directly being applied are briefly described.

8.1 Model evaluation

8.1.1 Thermal models

The results of the orbit prediction tests for GPS Block IIR consistently showed significant improvements with the addition of each thermal model. Inclusion of the solar panel model reduced the 3D RMS error by 10%. Thermal modelling of the MLI yielded much larger improvements, reducing the average error by a further 80%. This is contrast to the analysis of Vigue (1994), who stipulated that for GPS Block IIA, the solar panels would be the major contributor to the thermal force, since they were large, flat and constantly sun-facing. The dominance of the MLI model is a consequence of several factors. For GPS Block IIR, the blackening of the MLI gives rise to its high absorptivity, and emissivity, and causes a very large thermal force to result. The force effect of the panels on the other hand is particular low due to the emissivity of the back face (ε_b= 0.89) being higher than the emissivity of the front face (ε_f = 0.86). Even though panel front-face temperatures are higher than back-face ones, a higher proportion of available energy is emitted by the back face causing a substantial degree of cancellation in the resultant force.

The thermal albedo models cause a drop of only 1% in the residuals. This is due to the low earth radiation flux at the altitude of GPS satellites.

For those satellites in eclipse, inclusion of a penumbra flux model reduced 3D RMS errors by 20%. Final twelve hour orbit prediction errors for five GPS Block IIR

spacecraft over four weeks are 0.19 m in height, 0.07m across track and 0.57m along track.

For Jason-1, though the effect of the thermal force alone is hard to assess, it is a significant part of the total SRP and TRR model. Several tests indicate the improvement of the combined UCL SRP and TRR models in orbit determination compared to the CNES model. The scale factor, which is an important metric of model accuracy and stability, is now at the 1% level, compared to the previous value of 7%.

From these results, it can be stated that errors in orbit computations are reduced when the thermal models developed in this thesis are applied. A major strength of all the models produced in this thesis is their simplicity. They account for the precise shape and structure of real spacecraft without producing long algorithms which are difficult to implement.

A deficiency in the thermal models is the neglected affect of thermally re-radiated energy coming from the Earth. Jason-1 orbits at an altitude of 1336km, specifically chosen to minimise large drag affects, whilst still maintaining a high resolution of the earth's surface. At this altitude, the flux from Earth will be considerable and thermal re-radiation of this flux will undoubtedly cause perturbations to the spacecraft orbit. Though a method for this was developed and implemented for GPS block IIR, accurate flux models were not available to apply this method to Jason-1, and it was beyond the scope of this project to create them. If the earth radiation flux data set is created and implemented for Jason-1 it might account for some of the remaining 1% error in the solar scale.

Other factors which affect the accuracy of the models are the uncertainty with which particular parameters are known. These were discussed in Chapter 7 and mainly include solar panel front and back face emissivities, and the power draw regime of the panels. Agencies procuring a spacecraft from a manufacturer should request full information relating to material types used in the spacecraft construction, and their properties when known, in order to pass this on to mission analysis teams. Further research is needed in this area to improve knowledge of both properties and their associated uncertainties. It is hoped that an understanding of their importance may spur further research in the

determination of these parameters. It may also urge spacecraft manufacturers to document information to the best of their knowledge and ease its provision to mission scientists.

The thermal responses of some surfaces on Jason-1 have not been modelled. The effects of these surfaces were analysed in Section 7.2. For spacecraft with exposed surface components that are thought to contribute a high thermal force, finite element analysis (FEA), which was used as one technique for the thermal analysis of the solar panels in Section 5.4.2, could be used. There are many commercial packages which carry out thermal analysis using FEA. A significant problem faced when using these techniques is the lack of detailed structural and material properties data, which is extremely difficult to obtain. The suitability of these techniques must be judged depending on whether sufficient data is available, for example for the thermal coupling between the surface instruments and the inside of the bus and the structure and physical properties of the insides of the instruments, and whether the accuracy gains are worth the extra computational loads.

In general, since many missions fundamentally require thermal stabilisation of the spacecraft bus (Gilmore, D., 1994), most surfaces apart from antennas are substantially covered in MLI. Figure 8.1 shows a photograph of ENVISAT which was taken in a clean room. It is clear that vast surfaces of the spacecraft are covered in MLI. This gives another example of the importance of the MLI models, and how they are likely to be dominate the thermal models for a spacecraft.

Figure 8.1: ENVISAT in clean room

8.1.2 Eclipse and penumbra models

The problem of computing entry and exit times of spacecraft travelling through shadow regions is very important in many space projects when considering thermal, electrical power, and attitude control issues. It also has a crucial role in precise orbit determination and prediction.

The main operational software requirements for the computation of precise orbit trajectories are accuracy and efficiency. An important part of this must be the correct determination of eclipse shadow boundary transition times, as these boundaries control the periods over which SRP and TRR non-conservative force models should be applied. A review of the publicly available literature on this subject indicates that current methods are either accurate or efficient, but not both. By modelling the Earth as a spheroid, the above method retains the physical complexity inherent in the problem, yet the algorithm is as simple computationally as techniques which model the Earth as a sphere; this results in a highly efficient approach. Results of the tests carried out (Section 4.5.2) confirm the ability of this algorithm to be able to determine shadow crossing times for low Earth orbiting satellites when compared to photometric observations (ENVISAT) better than the spherical Earth models. Not only were the RMS offsets smaller, but the errors appeared to be more normally distributed that the

biased offsets obtained with the spherical Earth models. This means that any errors in the SRP and TRR modelling which could occur as a result of incorrect eclipse transition times should be minimised if this algorithm is used for LEO satellites.

The model however does not take into account the effects of the atmosphere on the shadow boundaries. The true transition between sunlight and darkness does not have hard boundaries but is actually a very complicated phenomenon. Absorption and refraction of radiation by the atmosphere and the apparent deformation of the solar disk as seen though the earth limb, influence the level of illumination of a spacecraft (Vokrouhlicky, D. et al. (III), 1994). While models of these phenomena exist, the complexity and computational burden imposed by such sophisticated shadow models has inhibited their widespread application (Hujsak, R., 1993).

These effects are less problematic for low earth orbiters, where the effect of light-bending is less severe, but at higher altitudes the degree of bending causes more blurring of the penumbra and umbra boundaries. A method to account for these effects without having to model the atmosphere would be to use photometry data to estimate boundary crossing times for many spacecraft orbits at a particular altitude, and then estimate the earth radii parameters (equatorial and polar radii) in a least squares sense which best fit the photometry data. These parameters could then be used when predicting orbits or determining orbits (pers comms, Ziebart, M., 2004).

So far only a very simple penumbra flux model has been implemented. A more accurate solution would depend upon calculating the exact area of the sun occluded by an oblate earth. This would results in a complex solution for the penumbral flux function, but should improve the characterisation of solar flux incident on the spacecraft and therefore yield a more accurate force due to SRP.

In this research, only solar radiation occlusion by the earth was studied. For a more rigorous determination of solar fluxes at all times, lunar eclipses could be included as well. Though the effect to a trajectory is likely to be small, at current levels of orbit prediction and determination it may yield small but consistent improvements.

8.2 Impact on GNSS constellation design

8.2.1 Constellation design

It is important to be able to predict long term orbit evolution of spacecraft when planning a constellation to ensure satellite visibility requirements on the ground are met. Satellite orbits are fundamentally shaped by the initial orbit and injection conditions of position and velocity, and the forces that subsequently act upon the satellite. Ziebart et al., (2003c) assess the impact of GNSS spacecraft structural design and conventionally ignored force effects on the long-term evolution of the orbit and shows that incorrect masses and surface optical properties will result in considerable differences to the long-term prediction of a satellite position. In this thesis, it has been shown that the thermal force causes perturbations at the level of a few metres after just twelve hours. The GPS system performs small fuel burns to correct the orbit when needed, hence the consequences of not accounting for the thermal forces are limited.

Europe's own GNSS system Galileo, is scheduled to be fully operational in 2008. The Galileo constellation will comprise 30 satellites in circular orbits at 23,616 km altitude. A paper by Mozo-Garcia et al., (2001) described how the projected orbit parameters for Galileo satellites were optimised so that orbit adjustments would not be necessary throughout the intended lifetime (typically ~10 years) of the constellation. It was planned that satellites would be built without the capability to make corrective burns as one method of reducing costs. This investigation did not take into account the effects of the thermal force in the orbit analysis; in fact the only non-conservative force considered was a very crude SRP model. In this thesis, an investigation was carried out to see what the long term impacts on an orbit were due to the effect of the thermal force. Orbits were predicted over a two year period, with and without inclusion of the thermal force, and errors in the range and in the Keplerian elements were analysed to investigate perturbations due to the TRR force. Figure 8.2 shows the size of the 3D differences in trajectory over the 2 year period.

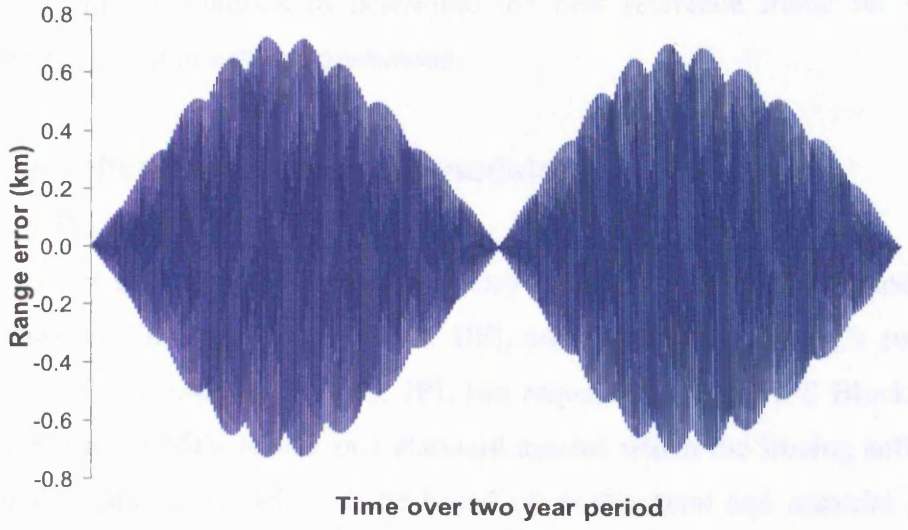

Figure 8.2: Range error resulting from no thermal force model

The maximum range error is ~0.8 km and this is reached after 6 months. The range error is observed to have an annual period, which was also seen for the eccentricity, the right ascension of the ascending node, and the inclination. This demonstrates that although substantial range errors occur over the course of an orbit, due to the once per orbit revolution nature of this force, the long term effects are not severe. The annual signature could be explained by the β angle, which is the angle between the orbit plane and the earth-sun line. As the earth rotates around the sun, this angle varies with (to first order) an annual period. After a year, the perturbations cancel and no overall changes to the orbit are detected. In terms of constellation design therefore, the thermal force is unlikely to affect the long term evolution of the orbit.

8.2.2 GNSS operation

For successful empirical parameterisation of un-modelled forces, it is important to choose a suitable reference frame. In the GPS system, the satellite ephemerides are calculated by the Master Control Station using parameters for the SRP and TRR forces modelled in the BFS XYZ system. The two parameters, K1 and K2 represent a solar scale and a y-bias term respectively. In Section 7.3, it was shown that modelling the thermal force in the body fixed XYZ frame with once per revolution parameters give rise to much larger residuals than when modelled in other axes systems, and as such it is unlikely that these could best correct for the effects. The Galileo constellation could

benefit from similar analyses to determine the best reference frame for empirical parameterisation used in orbit computations.

8.3 Applications of thermal models

8.3.1 GPS Block IIR

The US Airforce has contracted Boeing to carry out SRP, TRR and ERP modelling for the next phase of GPS spacecraft (Block IIF), and require that Boeing's software be validated by JPL. In order to do this, JPL has requested UCL's GPS Block IIR non-conservative force models to use as a standard against which the Boeing software will be measured. Boeing's models will be based upon structural and material properties data provided by UCL for a direct comparison. If both sets of resulting accelerations are similar within an acceptable margin of error, then Boeing's own software will be used for the work. Otherwise it is possible that Boeing may subcontract UCL to provide them with models.

8.3.2 Jason-1

As described in Chapter 7, UCL's SRP and TRR models have been tested in GIPSY-OASIS II by JPL. Test results showed significant improvements using the UCL model compared to the CNES model which were in place at the time. Since then, UCL models have been adopted for routine use in the orbit determination of Jason-1. Further involvement is anticipated for the Ocean Surface Topography Mission (OSTM) which is the follow-on to the Jason-1 mission, scheduled for launch in 2008.

8.3.3 ENVISAT

The Department of Geomatic Engineering at UCL is part of a Natural Environment Research Council (NERC) Centre of Excellence known as the Centre for the Observation and Modelling of Earthquakes and Tectonics (COMET). COMET scientists use satellite observation data to model the deformation of the Earth's crust in order to study the earthquake cycle, the affect of faulting and uplift on the Earth's surface, and the physics of continental deformation (http://comet.nerc.ac.uk/). COMET aims to use InSAR data acquired by the European satellite ENVISAT. Currently UCL's SRP and TRR models are being implemented for ENVISAT, as part of an effort to improve the accuracy of current ENVISAT orbits which are required for the correct interpretation of

InSAR measurements. Figure 8.3 shows the structure of the ENVISAT bus. The solar panel is not shown. The structure is largely covered in MLI and has a much more complex structure than GPS Block IIR. It is expected that the thermal force will be more difficult for a once per revolution empirical parameter to absorb.

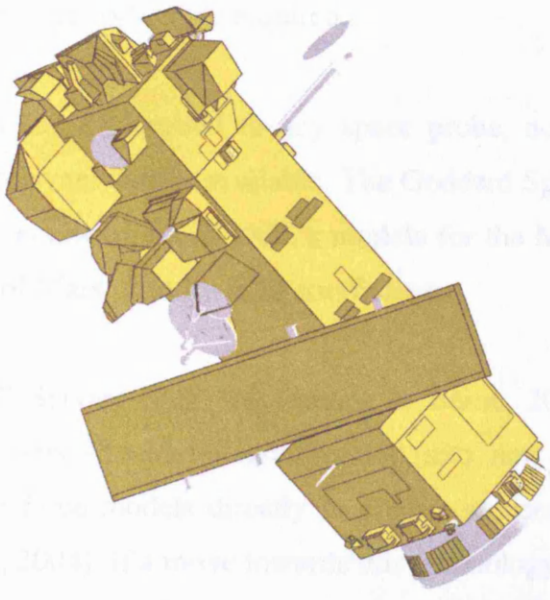

Figure 8.3: Model of ENVISAT bus

8.3.4 Future applications

In theory these techniques are applicable to all spacecraft, and as orbit precision requirements increase in geodesy and navigation applications, more missions will require detailed analytical non-conservative force models. Several current missions have expressed interest in the application of UCL's models to their spacecraft. Examples include:

- GRACE

  GRACE is a dedicated satellite mission whose objective is to map the global gravity field. It uses an on-board accelerometer to measure the non-conservative forces which are assumed to consist mainly of atmospheric drag, SRP, ERP and TRR forces. By physical modelling of the SRP, ERP and TRR, the accelerometer measurements can be used to derive the force due to drag, and hence atmospheric densities.

- Cryosat

  The purpose of the CryoSat mission is to determine trends in the ice masses of the Earth. Of principal importance is the testing of the predicted thinning of Arctic sea ice due to global warming, which could change the climate of the Arctic and possibly other regions. For the correct determination of the thickness of the ice-sheets, precise orbits are required.

Potentially these models can be applied to any space probe, not only earth-orbiting satellites, as long as the relevant data is available. The Goddard Space Flight Centre are currently considering the employment of UCL's models for the Mars Global Surveyor satellite for the recovery of Mars' gravity field coefficients.

At the International GPS Service (IGS) conference in Berne, 2004, one presentation suggested that force models should be incorporated into new GPS receivers. The receiver would use these force models directly to predict spacecraft positions in real-time (DiEsPosti, R. et al., 2004). If a move towards this technology were made, accurate prediction using force models would be a necessity.

Summary

The models have been evaluated based on their performance in orbit prediction and orbit determination tests. Test results suggest that the models are successful in accounting for a thermal force. Areas in which further research could improve the thermal models have been identified. These are mainly in the development of a thermal force due to earth radiation for Jason-1, and a more detailed description of the flux in penumbra regions, accounting for atmospheric effects. In this chapter, the impact of this force on the design and operation of missions has been discussed. Current applications of this work are outlined, and some examples of potential projects that the thermal models may be used for in the near future are given. In Chapter 9, the main conclusions of this study are given.

Chapter 9 Conclusions

Chapter outline

This chapter starts with a brief overview of the study. A statement of the study's principal conclusions follows this and the final section lists possible avenues of further research arising from the work presented in the thesis.

9.1 Overview of study

The main objectives of this research were to develop techniques to estimate spacecraft surface thermal re-radiation forces in order to increase accuracies with which orbits can be predicted and determined. In this thesis, generic methods are developed to calculate forces arising from the re-radiation of absorbed solar energy. Specific methods were developed for surfaces covered in multilayer insulation blankets and for solar panels. Other surface components were dealt with on a part by part basis where additional thermal data was available. The thermal forces arising from earth emitted radiation has also been investigated and implemented for GPS spacecraft. Additionally, efficient algorithms have been developed to calculate eclipse boundary crossing times, taking into account the earth's oblateness (Adhya, S. et al., 2004). A method for estimating the variation of solar flux in penumbral regions has also been developed. These methods are described in Chapter 4. The GPS Block IIR spacecraft and Jason-1, the US/French altimetry satellite were chosen as test cases for the evaluation of these models.

The GPS Block IIR models were tested by predicting orbits using numerical integration of a set of differential equations. The resulting trajectories were compared with precise Jet Propulsion Laboratory (JPL) non-fiducial ECI orbits. The complete force model included the GRACE GGM01C earth gravity to degree and order 15, solid Earth, secular and poletide variations in the geopotential coefficients, third body gravity due to the Sun, Moon, Jupiter, Mars and Venus, general relativistic effects, solar radiation pressure, earth radiation pressure and antenna thrust forces. Four weeks worth of twelve hour orbits for five GPS Block IIR spacecraft were predicted; Chapter 5 documents the

results of these tests. When thermal modelling of the solar panels was added to this, relatively small but consistent reduction in the differences between predicted orbits and precise orbits was observed. On average root mean square errors in the height, cross and along track (HCL) directions dropped from 1.41m, 0.23m and 3.00 m to 1.27m, 0.21m and 2.69 m. The impact of including modelling of MLI models further reduced HCL errors to 0.19m, 0.08m and 0.59m. Considering only the subset of satellites in eclipse season, inclusion of a penumbra flux model caused HCL residuals to drop from 0.16m, 0.03m and 0.70 m along track to 0.13, 0.03 and 0.56 m. The thermal albedo model did not greatly affect results, causing the overall range error to drop by ~ 2cm.

For Jason-1, combined solar radiation pressure and thermal models were implemented into JPLs orbit determination software GIPSY-OASIS II. Orbits were created using UCL models and JPLs existing models, which were developed by CNES. These orbits were compared in terms of parameters related to the size and variation of the solar scale, atmospheric drag, crossover residuals, orbit overlaps and laser ranging residuals. The results of these tests are documented in Chapter 6. The UCL models performed significantly better than in all dynamic orbit tests and in almost all reduced dynamic orbit tests. The outcome of these tests led to the incorporation of UCL's SRP and TRR models into JPLs routine orbit determination of Jason-1. The model is also currently being implemented by NASA Goddard Space Flight Centre.

9.2 Principal conclusions

The average total thermal force for GPS Block IIR is estimated to be 8.2 x 10^{-6} N, corresponding to an acceleration 7.4 x 10^{-9} ms^{-2} of which ~90 % is due to the spacecraft bus, and ~10 % due to the solar panels. For Jason, the thermal force had a magnitude and of 3.2 x 10^{-6} N, which corresponds to an acceleration of 6.6 x 10^{-9} ms^{-2}, of which 70% is due to the bus and 30% is due to the panels. From the GPS Block IIR orbit prediction results, the largest improvements were in the along track direction, though improvements were seen in all components. The modelling of the thermal forces has significantly improved both orbit prediction and orbit determination capabilities.

Accurate calculation of the thermal force depends mainly upon: solar irradiance in the vicinity of the spacecraft; spacecraft structure, surface absorptivities and emissivities,

conductivities of components that affect surface temperatures, spacecraft attitude and for low earth orbiters, radiation coming from the earth. It was found that the force model is most sensitive to errors in the front and back face emissivities of the solar panel. These parameters commonly have values between 0.8 to 0.9, and uncertainties of approximately 2.5%. This level of error can cause the force due to the solar panels to vary by a maximum of ±80%, which corresponds to variation of about 10% in the total TRR model. More accurate determination of these parameters would greatly reduce our uncertainty in the overall TRR model.

The magnitude of the thermal force is strongly dependent on the absorptivity of the multilayer insulation which covers the majority of surfaces of many spacecraft. The MLI on GPS Block IIR has a particularly high value of the absorptivity (0.94) because it is blackened, and thus gives rise to a high thermal force, with accelerations of the order of 6.6×10^{-9} ms^{-2}. This constitutes on average ~25% of the force due to the SRP force on the GPS Block IIR bus. The TRR acceleration due to the solar panels is only ~1% of the SRP force on the panels. For Jason-1, the MLI has a lower absorptivity and bus accelerations are about 3.5×10^{-9} ms^{-2}, which is ~15% of the force due to SRP. The solar panel TRR accelerations are ~5 % of the SRP force on the panels.

The remaining orbit prediction residuals (the differences between the precise and predicted orbits) for GPS Block IIR appeared to be chaotic; if a clear pattern had emerged, this would have strongly suggested an unmodelled or poorly modelled effect. This was not the case.

An important question when producing high precision analytical force models is whether they can be adequately modelled with empirical parameters if given sufficient tracking data. In Chapter 7, tests were carried out to examine how well once per orbit revolution parameters could model the thermal force for a GPS satellite. It was found that the reference frame in which the once per revolution parameters were applied made a difference to how well the thermal force was replicated. In the HCL basis, the thermal force appeared to have strong once per revolution characteristics, but in the spacecraft body fixed XYZ system, fitting a once-per rev term gave residuals which were twice the size. In the GPS system, the Master Control Station uses parameters in this frame, as

does GIPSY-OASIS II. It is unlikely that the thermal force will be correctly soaked up in this frame. Of course, empirical parameterisation can only soak up un-modelled effects when a large amount of tracking data is available; real time GPS orbit prediction does not afford this luxury, and the force model plays a much greater part in accurate positioning. Satellites which have more complex surface structures such as ENVISAT are likely to produce more complicated signatures and may be impossible to model with once per-rev parameters. It is only by a study of analytical models that the most appropriate frame for a particular effect can be identified. Moreover, the choice of frame for the empirical parameterisation may be driven by larger unmodelled effects. Clearly if a force can be dealt with analytically and efficiently, it improves the model redundancy and reduces the need to compromise the choice of reference frame for empirical parameterisation.

In Chapter 8, it was shown that a substantial part of the remaining orbit prediction error may be due to inaccuracies in the initial state vector used to seed the numerical integrator. A least squares adjustment process was used to calculate a set of initial conditions which was then used to seed orbit propagation. This led to a reduction of residuals by ~30% from an average RMS errors of 0.14m in height, 0.06m across track, and 0.42m.

Further analysis confirmed the sensitivity of the gravity field to small radial distance errors, and the impact of this on predicted orbits. It was found that once a divergence of the predicted orbit from the precise orbit occurred, this would then be exacerbated by application of a gravity force that was either larger or smaller than the gravitational force that the spacecraft would actually have been subject to. Application of the precise satellite position gravity field to the predicted orbit positions reduced RMS range residuals to 0.07m in height, 0.07m across track and 0.12m along track, and when the initial state vector was estimated as well, final orbit residuals reached 0.06m in height, 0.06m across track, and 0.09m. Though this knowledge cannot improve orbit prediction, it strongly supports the argument that the force models themselves are not as deficient as the residuals suggest. Final residuals of this size imply that the modelling of dynamic forces is close to the noise level, that is, these residuals are comparable to the accuracy at which post-processed precise orbits are known.

9.3 Future work

In order to further refine the force models and the ability to correctly define the trajectory of a spacecraft, several further areas of study have been identified. In terms of thermal modelling, complex instruments on the surface that are not covered in multi-layer insulation have not been modelled. Commercially available finite element software exists which can be used to calculate the spatially and temporally distributed temperatures. This could be used in theory, if detailed information about the internal structure and material properties of the spacecraft were obtainable, though this is often not the case. Care must be taken to ensure that the computational burden involved in the implementation of such analyses in orbit prediction/determination software should not be too high as to render it impractical. As computational power increases, computational intensity become less limiting in the development of new techniques.

The eclipse boundary crossing time model and penumbra flux model could be improved by taking into account simple models of atmospheric refraction effects, or attempting to account for them empirically as described in Chapter 8.

The current GPS earth radiation pressure models used in this study are detailed in that they use high temporal and spatial resolution data. However, the spacecraft bus model used in this process is relatively crude and treats the spacecraft bus as a flat plate. Although these models are currently the most developed that exist, they could be refined by applying the Earth fluxes to a more realistic spacecraft structure.

Earth radiation pressure models used in the orbit determination of Jason-1 are much less detailed than those used for GPS Block IIR. As Jason-1 is in a low orbit, it is likely that it will be more sensitive to the spatial distribution of the earth's radiation. Similar data to that used to create albedo models for GPS Block IIR, could be used to create an earth radiation pressure for Jason-1. This albedo model would enable the thermal effects arising form earth radiation pressure to be calculated as described in Section 5.4, and may account for the 1.01 scale factor for Jason-1. It is highly unlikely that the thermal response of the spacecraft to both solar radiation and earth radiation will have a once per orbit revolution effect, and it could be a fruitful topic for further research.

In terms of analytically modelling the forces on a spacecraft, this research, along with vast improvements in the gravity field and other non-conservative forces appears to bring predicted orbits at a level close to the noise boundary. The models could be improved by the techniques outlined above, but it is most likely that much higher accuracies will not be reached without significant improvements in the spacecraft engineering data used.

References

Adhya, S., Sibthorpe, A., Ziebart, M., & Cross, P. 2004, "Oblate Earth Eclipse State Algorithm for Low Earth Orbiting Satellites", *Journal of Spacecraft and Rockets*, vol. 41, no. 1, pp. 157-159.

Bapat, S. L., Narayankhedkar, K. G., & Lukose, T. P. 1990, "Experimental Investigations of Multilayer Insulation", *Cryogenics*, vol. 30, pp. 711-719.

Bar-Sever, Y. 1996a, "A New Model for GPS Yaw Attitude", *Journal of Geodesy*, vol. 70, pp. 714-723.

Bar-Sever, Y., Bertiger, W., Davis, E., & Anselmi, J. 1996b, "Fixing the GPS Bad Attitude: Modelling GPS Satellite Yaw During Eclipse Seasons", *Navigation*, vol. 43, no. 1, pp. 25-39.

Bar-Sever, Y. 1997, *IGS Electronic Mail* 1653.

Barkstrom, B. R. 1984, "The Earth Radiation budget Experiment (ERBE)", *Bulletin of the American Meteorological Society* no. 65, pp. 1170-1185.

Behr, J., King, N., & Hudnut, K. W. 1998, "Monitoring Structural Deformation at Pacoima Dam, California Using Continuous GPS", *11th Int.Technical Meeting of the Satellite Division of the U.S.Inst.of Navigation GPS ION-98, Nashville, Tennessee, 15-18 Sept.,59-68.*

Bertiger, W. 2004, "Five-Millimetre Orbit Determination for Ocean Altimetry", *Aviso Newsletter, Centre National d'Etudes Spatiales* no. 10.

Beutler, G., Brockmann, E., Gurtner, W., Hugentobler, U., Mervant, L., Rothacer, M., & Verdun, A. 1994, "Extended Orbit Modeling Techniques at the CODE Processing Center of the International GPS Service for Geodynamics (IGS)", *Manuscripta Geodetica* no. 19, pp. 367-386.

Bomford, G. 1971, *Geodesy*, Third edn, Oxford University Press.

Borderies, N. & Longaretti, P. 1990, "A New Treatment of the Albedo Radiation Pressure in the Case of a Uniform Albedo and a Spherical Satellite", *Celestial Mechanics* pp. 69-98.

Chapman, A. J. 1984, *Heat Transfer* Macmillan.

Colombo, O. 1989, "The Dynamics of GPS Orbits and the Determination of Precise Ephemerides", *Journal of Geophysical Research* , vol. 94, pp. 9167-9182.

Cook, R. A. 1989, *The Effects of Thermal Imbalance Forces on Simple Spacecraft,* Centre for Space Research, University of Texas, Austin.

DiEsPosti, R., DiLellio, J., Kelley, C., Dorsey, A., Fliegel, H., Berg, J., Edgar, C., Mc Kendree, T., Fullerton, P., & Shome, P. 2004, "The Proposed State Vector Representation of Braodcast Navigation Message for User Equipment Implementation of GPS Satelltie Ephemeris Propagation", *Proceedings of the Institute of Navigation, January 2004, San Diego, CA.*

Ferrier, C., Gratton, S., & Mercier, F. "Radiation Pressure Modelling of Jason-1 and Empirical Parametrisation", Jason-1 Science Working Team Meeting, Biarritz, France, 2002.

Fliegel, H. F., Gallini, T. E., & Swift, E. R. 1992, "Global Positioning System Radiation Force Model for Geodetic Applications", *Journal of Geophysical Research*, vol. 97, no. 1, pp. 559-568.

Fliegel, H. F. & Gallini, T. E. 1996, "Solar Force Modelling of Block IIR Global Positoning System Satelliltes", *Journal of Spacecraft and Rockets*, vol. 33, no. 6, pp. 863-866.

Fortescue, P., Stark, J., & Swinerd, G. 2003, *Spacecraft Systems Engineering*, Third edn, Wiley.

Frolich, C. & Lean, J. 1998, "The Sun's Total Irradiance: Cycles, Trends and Related Climate Change Uncertainties since 1976", *Geophysical Research Letters*, vol. 25, no. No. 23, pp. 4377-4380.

Fu, L. & .Cazenave, A. 2000, *Satellite Altimetry and Earth Sciences A Handbook of Techniques and Applications*, 69 edn, Academic Press.

Galvin, D. M. 1999, "History of the GPS Space Segment From Block I to the New Millenium", *Proceesings of ION GPS International Technical Meeting of the Satellite Division,Sept.1999, Nashville, TN.*

Gilmore, D. 1994, *Satellite Thermal Control Handbook* The Aerospace Corporation Press, El Secundo, California.

Gregorius, T. 1996, *GIPSY-OASIS II How it Works*, Department of Geomatics, University of Newcastle upon Tyne.

Haines, B., Bertiger, W., Desai, S., Kuang, D., Munson, T., Young, L., & Willis, P. 2002, "Initial Orbit Determination Results for Jason-1: Towards a 1-cm Orbit", *Proceedings of ION GNSS International Technical Meeting of the Satellite Division, 21-24 Sept.2002, Portland, Oregon.*

Haines, B., Bar-Sever, Y., Bertiger, W., Desai, S., & Willis, P. 2004, "One-Centimeter Orbit Determination for Jason-1: New GPS-Based Strategies", *Marine Geodesy*, vol. 27, p. 299–318.

Hatch, R. R. 1995, "Relativity and GPS (Section I: Special Relativity)", *Galilean Electrodynamics*, vol. 6, no. 3, pp. 51-57.

Heroux, P., Gao, Y., Kouba, J., Lahaye, F., Mireault, P., Collins, P., Macleod, K., Tetreault, P., & Chen, K. 2004, "Products and Applications for Precise Point Positioning-Moving Towards Real-Time", *Proceedings of ION GNSS 17th International Technical Meeting of the Satellite Division, 21-24 Sept.2004, Long Beach, CA.*

Hudnut, K. W. 1995, "Earthquake Geodesy and Hazard Monitoring", *Reviews of Geophysics (Supplement: U.S.National Report to IUGG)* pp. 249-255.

Hugentobler, U. & Beutler, G. 2003, "Strategies for Precise Orbit Determination of Low Earth Orbiters Using the GPS", *Space Science Reviews*, vol. 108, pp. 17-26.

Hugsak, R. S. 1993, "Solar Pressure", *Proceedings of the Artificial Satellite Theory Workshop.*

Incropera, F. P. & Dewitt, D. 2002, *Introduction to Heat transfer*, Fourth edn, John Wiley and Sons.

Jacchia, L. G. 1977, *Thermospheric Temperature, Density, and Composition: New Models*, Smithsonian Astrophysical Observatory, 375.

Kaplan, E. D. 1996, *Understanding GPS Prinicples and Applications* Artech house Publishers.

Knocke, P. C., Ries, J. C., & Tapley, B. D. 1998, "Earth Radiation Pressure Effects on Satellites", *American Insstitute of Aeronautics and Astronautics* pp. 1-11.

Laxon, S. Physics of the Earth. wwwcpg.mssl.ucl.ac.uk/people/swl/lectures, 2003. Ref Type: Electronic Citation

Leick, A. 2004, *GPS Satellite Surveying*, Third edn, John Wiley and Sons Inc..

Lemoine, F. G. 1997, *The Development of the NASA GSFC and NIMA Joint Geopotential Model* Springer-Verlag.

Lichten, S. M. & Border, J. S. 1987, "Strategies for High Precision Global Positioning System Orbit Determination", *Journal of Geophysical Research*, vol. 92, no. B12, pp. 12751-12762.

Liu, M., Yang, Y., Stein, S., Zhu, Y., & Engeln, J. 2000, "Crustal Shortening in the Andes: Why do GPS Rates Differ from Geological Rates?", *Geophysical Research Letters*, vol. 27, no. 18, pp. 3005-3008.

Marquis, W. & Krier, C. 2000, "Examination of the GPS Block IIR Solar Pressure Model", *ION GPS 2000*, vol. 19-22, pp. 407-415.

Martin, C. F. & Rubincam, D. P. "Earth albedo affects on Lageos I satellite based on Earth Radiation Budget (ERBE) satellite measurements,", EOS, paper G32A-3, presented at the Spring Meeting of the AGU, Baltimore, MD, 1993

McCarthy, D. D. 1996, *IERS Conventions Technical Note 21* Observatoire de Paris.

Milani, A., Nobili, A. M., & Farinella, P. 1987, *Non-graviational Perturbations and Satellite Geodesy* Adam Hilger.

Misra, P. & Enge, P. 2001, *Global Positioing System Signals, Measurements, and Performance* Ganga-Jamuna Press.

Montenbruck, O. & Gill, E. 2000, *Satellite Orbits Models Methods Applications* Springer-Verlag.

Mozo-Garcia, A., Herraiz-Monseco, E., Martin-Piero, A. B., & Romay-Merino, M. 2001, "Galilieo Constellation Design", *GPS Solutions*, vol. 4, no. 4, pp. 9-15.

Neta, B. & Vallado, D. 1994, "On Satellie Umbra/Penumbra Entry and Exit Positions", *AAS97-155* pp. 715-724.

Otsubo, T., Appleby, G., & Gibbs, E. 2001, "GLONASS Laser Ranging Accuracy With Satellite Signature Effect", *Surveys in Geophysics*, vol. 22, no. 6, pp. 507-514.

Press, W. H., Teukolsky, S. A., Vetterling, W. T., & Flannery, B. P. 2002, *Numerical Recipes in C++*, Second edn, Cambrige University Press.

Price, B. A. & Smith, T. F. 1994, "Thermal Response of Composite Building Envelopes Accounting for Thermal Radiation", *Energy Conservation Management*, vol. 36, no. 1, pp. 23-33.

Reigber, C., Gendt, G., Dick, G., & Tomassini, M. 2002, "Water Vapor Monitoring for Weather Forecasts", *GPS World* pp. 18-27.

Rubincam, D. P. 1987, "LAGEOS Orbit Decay Due to Infrared Radiation from Earth", *Journal of Geophysical Research*, vol. 92, pp. 1287-1294.

Scharroo, R. 2002, *A Decade of ERS Satellite Orbits and Altimetry* Delft University Press.

Schwintzer, P., Reigber, C., Massmann, F., Bode, A., Meixner, H., Raimondo, J., Zhu, S., Biancale, R., Balmino, G., Lemoine, F., Marty, J., Moynot, B., Barlier, F., Boudon, Y., Exertier, P., Laurain, O., & Gruber, T. 1999, "Status of the GRIM-5 Gravitational Model Development", *Eos Transactions, AGU*, vol. 80, no. 17.

Seeber, G. 2003, *Satellite Geodesy* Walter de Gruyter.

Seidelmann, P. K. 1992, *Explanatory Supplement to the Astronomical Almanac* University Science books.

Slabinski, V. J. 1988, "LAGEOS Acceleration Due to Intermittent Solar Heating During Eclipse Periods", *American Astronomical Society Preprint.*

Springer, T. A., Beutler, G., & Rothacher, M. 1999, "A New Solar Radiation Pressure Model For GPS", *Adv.Space Res.*, vol. 29, no. No. 4, pp. 673-676.

Standish, E. M. JPL Planetary and Lunar Ephemerides: Export Information, 2004. http://ssd.jpl.nasa.gov/iau-comm4/README,
Ref Type: Electronic Citation

Svehla, D. & Rothacher, M. 2003, "Kinematic and Reduced-Dynamic Precise Orbit Determination of Low Earth Orbiters", *Advances in Geosciences* no. 1, pp. 47-56.

Tapley, B. D. 1994, "Precision Orbit Determination for TOPEX/POSEIDON", *Journal of Geophysical Research TOPEX/POSEIDON Special Issue*, vol. 99, no. 24, pp. 383-404.

Tapley, B. D., Watkins, M., Ries, J., Davis, G., Eanes, R., Poole, R., Rim, H., Schutz, B., Shum, C., Nerem, S., Lerch, F., Marshall, J., Klosko, S., Pavlis, N., & Williamson, R. 1996, "The Joint Gravity Model 3", *Journal of Geophysical Research*, vol. 101, no. B12, pp. 28029-28049.

Tapley, B. D., Schutz, B. E., & Born, G. 2004, *Statistical Orbit Determination* Elseiver Academic Press.

Tikhonravov, M. K. 1994, "The Creation of the First Artificial Earth Satellite: Some Historical Details", *Journal of the British Interplanetary Society*, vol. 47, no. 5, pp. 191-194.

Tsai, J. 2004, "Overview of Satellite Thermal Analytical Model", *Journal of Spacecraft and Rockets*, vol. 41, no. 1, pp. 120-125.

Vallado, D. 1997, *Fundamentals of Astrodynamics and Applications* McGraw-Hill.

Vigue, Y., Schutz, B. E., & Abusali, P. A. M. 1994a, "Thermal Force Modelling for Global Positioning System Satellites Using the Finite Element Method", *Journal of Spacecraft and Rockets*, vol. 31, no. 5, pp. 855-859.

Vigue, Y. S., Lichten, M., Muellerschoen, R., G.Blewitt , & M.B.Heflin 1994b, "Improved GPS Solar Radiation Pressure Modelling for Precise Orbit Determination", *Journal of Spacecraft and Rockets*, vol. 31, no. 5, pp. 830-833.

Vokrouhlicky, D., Farinella, P., & Mignard, F. 1994, "Solar Radiation Pressure Perturbations for Earth Satellites: III. Global Atmospheric and the Albedo Effect", *Astronomy and Astrophysics* no. 290, pp. 324-334.

Vokrouhlicky, D., Farinella, P., & Mignard, F. 1996, "Solar Radiation Pressure Perturbations for Earth Satellites: IV. Effects of the Earth's Polar Flattening on the

Shadow Structure of the Penumbra Transitions", *Astronomy and Astrophysics* no. 307, pp. 635-644.

Weinberg, S. 1972, *Gravitation and Cosmology* Wiley.

Wielicki, B. A., Barkstrom, B. R., Harrison, E. F., Lee, R. B., Smith, G. L., & Cooper, J. E. 1996, "Clouds and the Earth's Radiant Energy System (CERES): An Earth Observing System Experiment", *Bulletin of the American Meteorological Society* no. 77, pp. 853-868.

Woodburn, J. 2000, "Effects of Eclipse Boundary Crossings on the Numerical Integration of Orbit Trajectories", *American Institute of Aeronautics*, AIAA-2000-4027.

Ziebart, M. & Dare, P. 2001, "Analytical Solar Radiation Pressure Modelling for GLONASS Using a Pixel Array", *Journal of Geodesy*, vol. 75, pp. 587-599.

Ziebart, M., Adhya, S., Sibthorpe, A., & Cross, P. 2003a, "Residual Systematic Biases in Spacecraft Orbits", *Proceedings of Workshop on the State of GPS Vertical Positioning Precision Separation of Earth Processes by Space Geodesy.*

Ziebart, M., Adhya, S., Sibthorpe, A., & Cross, P. 2003b, "GPS Block IIR Non-Conservative Force Modelling: Computation and Implications", *Proceedings of ION GNSS 16th International Technical Meeting of the Satellite Division, 9-12 Sept.2003, Portland, Oregon.*

Ziebart, M., Adhya, S., Sibthorpe, A., & Cross, P. 2003c, "Taking the Long View: The Impact of Spacecraft Structural Design and High Precision Force Modelling on Long Term Orbit Evolution", *Proceedings of the Technical Meeting of the Satellite Division of The Institute of Navigation.*

Ziebart, M. 2004a, "Generalized Analytical Solar Radiation Pressure Modeling Algorithm for Spacecraft of Complex Shape", *Journal of Spacecraft and Rockets*, vol. 41, no. 5, pp. 840-848.

Ziebart, M., Edwards, S., Adhya, S., Sibthorpe, A., & Cross, P. 2004b, "High Precision GPS IIR Orbit Prediction Using Analytical Non-conservative Force Models", *Proceedings of ION GNSS 17th International Technical Meeting of the Satellite Division, 21-24 Sept.2004, Long Beach, CA.*